LANCASTER UNIVERSITY

Remote Sensing of Jupiter's Magnetospheric Dynamics

by

Rebecca Louise Gray

This thesis is submitted in partial fulfilment of the requirements
for the degree of Doctor of Philosophy

in the
Faculty of Science and Technology
Department of Physics

May 2018

Declaration of Authorship

I, Rebecca Louise Gray, declare that this thesis titled, 'Remote Sensing of Jupiter's Magnetospheric Dynamics' and the work presented in it are my own. I confirm that:

- This work was done wholly while in candidature for a research degree at this University.
- Where any part of this thesis has previously been submitted for a degree or any other qualification at this University or any other institution, this has been clearly stated. Two papers have been published in peer reviewed journals as a result of this thesis. These can be found in chapters 4 and 5 respectively:

  Gray, R. L., S. V. Badman, B. Bonfond, T. Kimura, H. Misawa, J. D. Nichols, M. F. Vogt, and L. C. Ray (2016), Auroral evidence of radial transport at Jupiter during January 2014, J. Geophys. Res. Space Physics, 121, 99729984, doi: 10.1002/2016JA023007.

  Gray, R. L., S. V. Badman, E. E. Woodfield, and C. Tao (2017), Characterization of Jupiter's secondary auroral oval and its response to hot plasma injections, J. Geophys. Res. Space Physics, 122, 64156429, doi: 10.1002/2017JA024214.
- Where I have consulted the published work of others, this is always clearly attributed. I have also acknowledged all main sources of help.
- Where I have quoted from the work of others, the source is always given. With the exception of such quotations, this thesis is entirely my own work.
- Where the thesis is based on work done by myself jointly with others, I have made clear exactly what was done by others and what I have contributed myself.

Signed: ____________________

Date: ____________________

'Nope, still one of your five-a-day...'

Abigail Kimberley

LANCASTER UNIVERSITY

Abstract

Faculty of Science and Technology
Department of Physics

Doctor of Philosophy

by Rebecca Louise Gray

This thesis presents and examines evidence of Jupiter's magnetospheric dynamics, primarily using Hubble Space Telescope images of the planet's ultraviolet aurora. The first two studies discuss the radial transport of hot plasma injections from reconnection return flow. The auroral evidence for a global magnetospheric disturbance is examined and it is found that the aurora showed a significantly super-rotating polar spot poleward of the main emission on the dawnside. The spot transitioned from the polar to main emission region in the presence of a locally broad, bright dawnside main emission feature and two large equatorward emission features. This is taken to be evidence of a prolonged period of reconnection and plasma injection, taking place over several hours. The second chapter examines the effect of hot plasma injection in the middle to inner magnetosphere. The location of the second oval feature lies between the Ganymede and Europa moon footprint contours between 150 and 240° system III longitude, corresponding to a source in the inner magnetosphere between 9 and 13 R_J. The feature is enhanced in both brightness and longitudinal spread 1-3 days after large hot plasma injections. It was suggested that wave-particle interactions are responsible for the scattering of electrons in this region. A third study investigated the auroral response to co-rotating interaction regions and solar wind compression. It was shown that in there are both high latitude and mid latitude features that arise - large scale flashes appear at high latitudes, sometimes along side significant branching of the main emission region. It is suggested that the arcs in the main emission are a result of strong compression either due to enhanced flow structures at the dusk side or a stepwise co-rotation breakdown in response to increase of azimuthal plasma velocity.

Acknowledgements

For God, the creator, sustainer and renewer of the universe (who also made Jupiter dead complicated).
For God, who redeemed us to be His people through His death.
'And we know that God causes all things to work together for good to those who love God, to those who are called according to His purpose.' - Romans 8:28, NASB.

Thanks must go primarily to my supervisor, Sarah, who has shown incredible kind patience to me. Thanks also to my colleague and friend Joe whose encouragement both verbally and practically has kept me going.

Thanks to my family, who have loved and supported me throughout. Thanks to Daniel and Maria, who have taught me how to relax. Thanks to Emma, who has been faithful in prayer, encouragement and modelling the good life.

Thanks to Sam who in terms of sheer effort has half earned this PhD herself, to Ace and Daisy who have been my very good friends, and to Ollie who has kept me grounded with a shared sense of dark humour.

I also acknowledge the teams who have worked on the Hubble Space Telescope, Hisaki, Wind/WAVES and mSWiM datasets, my co-authors and my fellow ISSI teammates - without the work of these scientists, this work would not be possible. I also acknowledge the funding I received in my studentship from STFC. HST and WAVES data can be found on the STScI and CDAWeb websites respectively.

Contents

Declaration of Authorship **i**

Abstract **iii**

Acknowledgements **iv**

List of Figures **viii**

List of Tables **xv**

Abbreviations **xvi**

1 Introduction **1**
- 1.1 The Sun and Solar Wind . . . 1
- 1.2 Frozen-in-Flow and Magnetic Reconnection . . . 3
- 1.3 Planetary Magnetospheres . . . 6

2 Jupiter **10**
- 2.1 Jupiter's Magnetospheric Structure . . . 10
  - 2.1.1 Inner, Middle and Outer Magnetospheric Structure . . . 10
  - 2.1.2 Magnetic Field Configuration . . . 17
- 2.2 Interchange and Injections . . . 18
- 2.3 Auroral Physics . . . 22
  - 2.3.1 Precipitation Processes . . . 22
    - 2.3.1.1 Scattering . . . 23
    - 2.3.1.2 Field-Aligned Currents . . . 24
    - 2.3.1.3 Stochastic Acceleration . . . 26
- 2.4 Auroral Signatures . . . 28
  - 2.4.1 Ultraviolet Signatures . . . 28
    - 2.4.1.1 Outer Emission . . . 29
    - 2.4.1.2 Main Emission . . . 30
    - 2.4.1.3 Polar Emission . . . 32

2.4.1.4 Moon Footprints 32
2.4.2 Radio Emission 33

3 Instrumentation and Data Reduction 35
3.1 Hubble Space Telescope Instrumentation 35
3.1.1 Spectral Imaging 37
3.1.2 Waves on WIND 37
3.2 Data Reduction 38
3.2.1 Image Processing Pipeline 38
3.2.2 Deriving Data Products From Images 39
3.2.2.1 Colour Ratio 39
3.2.2.2 Electron Flux, Brightness and Power 40

4 Auroral Evidence of Radial Plasma Transport 42
4.1 Introduction 42
4.2 Results 43
4.2.1 Auroral Features 43
4.2.2 Magnetospheric Source Regions 47
4.2.3 Emitted Auroral Power 49
4.3 Discussion: Interpretation of Auroral Signatures 50
4.4 Global Picture from Radio Observations 53
4.5 Conclusions and Summary 57

5 Response of Jupiter's Secondary Auroral Oval to Hot Plasma Injections 59
5.1 Introduction 59
5.2 Observation Overview 60
5.3 Feature Detection Algorithm 62
5.4 Results 65
5.4.1 Second Oval Location 65
5.4.2 Magnetic mapping of features to equatorial plane 70
5.4.3 Auroral brightness 71
5.4.4 Temporal Evolution 74
5.4.5 Spectral observations 75
5.5 Possible generation mechanism: Wave-Particle Interactions 76
5.6 Interpretation and Discussion 78
5.7 Summary 80

6 UV High Latitude Response to Solar Wind Compressions 81
6.1 Introduction 81
6.2 Theory 81
6.3 Auroral response to solar wind CIRs in February and March 2007 85
6.4 Analysis 91
6.4.1 High latitude response 91
6.4.2 Local time dependence of pulsating features 92

6.5 Discussion . . . 96
6.6 Conclusion . . . 101

7 Summary and Future Work 103
7.1 Summary . . . 103
7.2 Future Work . . . 106

Bibliography 109

List of Figures

1.1 An artist's impression of the Heliospheric Current Sheet configuration in interplanetary space. Courtesy NASA. 3

1.2 Schematic of a corotating interaction region in the solar equatorial plane. The solid black lines represent magnetic field lines and arrows show the outflow of the solar wind. After (*Gosling and Pizzo*, 1999) 4

2.1 Schematic in the merdional plane in the inner to middle magnetosphere of momentum supplied to sub-corotating plasma in the equatorial plane from the planet. The arrowed solid lines indicate magnetic field lines, curved outward the plane of the page by azimuthal currents in the middle magnetosphere current sheet. Iogenic plasma is shown by the dotted region. Three separate angular velocities associated with the system are that of the planet Ω_J, a particular shell of field lines ω, and of the neutral upper atmosphere in the Pedersen layer of the ionosphere, Ω_J^*. The opposite current represented by the dashed arrow. After (*Cowley and Bunce*, 2001, 2003). 12

2.2 Schematic of the reconnection in the meridonal plane. Panel a shows the stretched field after mass loading from Io has stretched the field lines the plasma is attached to in the radial direction (aside from the current sheet). Panel B shows the field reconnecting and consequent plasma flows radially away from the reconnection site. The field has dipolarised and the magnitude of B_θ has increased, positively planetward of the reconnection site and negatively tailward of it. After (*Vogt et al.*, 2010; *Vogt et al.*, 2014). 13

2.3 Schematic of the plasma flowlines (solid) in the equatorial plane. Dashed lines show the boundaries of flowlines that act in the co-rotation (inner) and convection driven (outer) regimes. The Dungey and Vasyliunas reconnection lines are marked with 'X's. 'O' marks the formation point of the plasmoid created by Vasyliunas reconnection and 'P' marks its outer bound, which asymptotes to the dusk tail magnetopause. After (*Cowley et al.*, 2003; *Badman and Cowley*, 2007). 14

2.4 (Top panel) The basic magnetospheric field configuration in the noon-midnight meridian and (bottom panel) the basic current flows in the equatorial plane. After *Khurana et al.* (2004). 16

2.5 Schematic showing the detection of the interchange process at the edge of the IPT. Flux in and flux out are descibed by the dashed and solid arrows respectively. After (*Kivelson et al.*, 1997; *Krupp et al.*, 2004). 19

2.6 Schematic of the plasma injection (red), which happens quickly. Dispersive drift due to rotation and magnetic field gradients cause energy dispersion over a longer period of time. After (*Mauk et al.*, 2002). 21

2.7 JEDI data taken during PJ4 of Juno's orbits. a) Downward intensity I versus electron energy E spectra for the times identified in panel c. b) Integrated downward electron energy flux. c) Intensity versus energy distributions for electrons within 20deg of the downward magnetic field direction. d) Pitch angle distributions of intensities averaged over electron energy (301,000 keV); the labels upward and downward indicate the portions of the plot (top and bottom) that represent electrons moving away from and towards Jupiter respectively. Mlat is the dipole magnetic latitude using the VIP4 field model dipole. R is the distance of Juno from the centre of Jupiter in R_J. Taken from *Mauk et al.* (2017a). 24

2.8 A plasma bubble in the magnetosphere I, the current integrated over the bubble, linked by the field aligned current $J_{||}$, dashed, into the ionosphere, where the Ionospheric current flows. The bubble itself flows planetward, as indicated by the grey arrow. The polar spot is formed on the 'up' FAC from the dawnside of the bubble. After *Radioti et al.* (2010) and *Nakamura et al.* (2001). 27

2.9 A schematic showing the most frequent UV auroral signatures as revealed by HST. The schematic is oriented with 180° system III longitude to the bottom. Taken from *Grodent* (2015). 28

2.10 A polar-projected HST image of Jupiter's northern FUV aurora taken at around 180° CML. The image is displayed with a log intensity scale saturated at 1000 kR. The grey lines indicate a 10° × 10° jovicentric latitude-system III longitude grid. The image is oriented such that 180° λ_{III} is directed toward the bottom and λ_{III} labels are displayed in grey. . 29

2.11 Example radio data from WIND waves in 2007 showing detection of Jovian radio decametric (DAM), hectometric (HOM) and solar bursts. The DAM emission is vertex late so corresponds to a dusk source. Taken from *Yoneda et al.* (2015). 34

3.1 A simplified schematic of the optics on the STIS after *Woodgate et al.* (1998) 36

4.1 Six panels showing polar-projected HST image of Jupiter's northern FUV aurora on 11 Jan 2014 at a) 00:41 UT, b) 01:06 UT, c) 01:08 UT, d) 01:10 UT, e) 01:11 UT and f) 19:39 UT. For each image the exposure time was 100 s. The Central Meridian Longitude (CML) is shown. The image is displayed with a log intensity scale saturated at 1000 kR. The dashed white line shows the edge of the field of view. The grey lines indicate a 10° × 10° jovicentric latitude-system III longitude grid. The image is oriented such that 180° λ_{III} is directed toward the bottom and λ_{III} labels are displayed in grey. On panels a-e, labels indicate the super-rotating polar spot (A), circled on panel b, a bright and expanded main emission region (B) and two equatorward emissions (C and D). The yellow lines on panel f, taken ∼18 h after the first visit, show the boundaries of the main emission region, derived from the average main emission position over the 2014 campaign. The poleward region of the main emission strip is the 'polar region' and the equatorward region up to 1.5 ° poleward of the Io footprint is the 'equatorward' region. Equatorward emissions circled in green on this image are possible remnants of the equatorward features C and D. 44

4.2 Polar-projected HST image of feature B taken at 00:41 UT, as in Fig. 1a, showing substructure. Longitude and latitude labels are displayed. 46

4.3 The location in the equatorial plane of the auroral features observed on 11 January 2014. The red stars show the equatorial mapping of the centre (specifically the brightest central point of the 200 kR contour) of the super rotating polar spot as it moves over the image sequence and the coloured boxes are the extrema of the auroral features. The poleward edges of the features were mapped using the flux equivalence method at 170° CML (*Vogt et al.*, 2011, 2015) with the GAM internal field model (*Grodent et al.*, 2008a). The VIPAL internal field model alone was used to map the equatorward edges of the main emission and equatorward emission features (*Hess et al.*, 2011). The Sun is to the right hand side. The blue box shows the expanded main emission (B), the green shows the left-hand equatorward feature (C) and the orange shows the right-hand equatorward feature (D). Solid black lines indicate the compressed and expanded magnetopause after *Joy et al.* (2002). 48

4.4 Power emitted from the different auroral regions over the 2014 HST campaign. The regions shown in colour from top to bottom are the main emission region (red), polar region (green) and the equatorward region (blue). The vertical grey shaded region indicates the HST visits of interest at 01:00 UT on day 011. The boundaries of these regions are indicated on Figure 4.1f. In each plot, the black points indicate the total power in order to indicate the contribution of each region to the total power. . . . 50

4.5 Averaged intensity at 3.5 MHz from WIND/Waves sorted by CML for the planetary rotation before (blue, 15:10-01:00 UT), during (green, 01:00-11:10 UT) and after (red, 11:10-21:10 UT) the auroral sequence in Fig 4.1b-e on day 11. The solid line shows campaign average intensity, in 10° bins. The coloured points plot the intensity averaged over 10° bins for successive rotations. 54

4.6 Radio spectra from Wind WAVES RAD1 (20-1040 kHz) and RAD2(1.075-13.82 MHz) detectors on day 011 (a) and day 014 (b). The flux density of both receivers is not cross-calibrated, producing the apparent discontinuity across the detector ranges. HOM emission is expected up to a few MHz. The HOM emission on day 011 is the between ∼00:30-02:30 UT and 150-220° CML, between 0.8-4 MHz. The HST image sequences are marked for indication: HST Sequence 1 (00:31-00:41 UT), HST Sequence 2 (01:01-01:11 UT) and the next sequence showing the relaxed main emission state, HST Sequence 3 (19:39-19:49 UT). A clearer HOM signal for comparison on day 014 is between ∼19:30-21:00 UT and 205-265° CML, between 0.7-6 MHz. The non-Io DAM signature on day 011 is at ∼04:00 UT and ∼270° CML. A typical solar burst showing decreasing frequency with time is highlighted. The colour scale is saturated at 1.5 dB to show Type III solar bursts. 56

5.1 Six polar projected images taken with the HST, with log intensity scale saturated at 400 kR. For each image the exposure time was 100 s. The grey lines indicate a 10° × 10° jovicentric latitude-system III longitude grid. The image is oriented such that 180° system III longitude is directed toward the bottom and labels are displayed in grey. Top row, left to right, a) Injection event, day 4 01:10 UT, average main emission position for campaign in gold, b) day 6 02:35 UT, c) day 7 07:16 UT. Bottom row, left to right, d) Injection event, day 11 00:31 UT, e) day 13 22:39 UT, f) After HOM emission on day 14, day 16 00:03 UT. 61

5.2 Polar projected HST UV 2014 campaign average image with inner and outer boundaries of intensity slices (red diamonds) used for second peak detection. Inner boundary is an example adjusted main emission; outer emission is the footpoint of the field line that crosses the equatorial plane at 7 R_J mapped with the VIPAL model. For peak detections, slices are taken between pairs of points. Average main emission also shown (black crosses). An example slice is shown around 160° longitude in red. 63

5.3 Two example intensity profiles from day 16 showing the second oval point selected (green). (Top) 148° longitude, clear main and second oval peaks; Gaussian profile (blue) subtracted from intensities (black) to give residual emission (red). (Bottom) 160° longitude, clear second but dim main emission; highest peak selected. 64

5.4 Two HST images from (a) day 6, and (b) day 16 with overplotted selected second oval points. (c) Second oval points from both day 6 (green) and day 16 (red), with the campaign average main emission to guide the eye. Moon footprint positions are also overplotted. 66

5.5 (a) Average campaign emission image with overplotted moon footprint contours (Europa in red, Ganymede in orange) and second oval points (black) with errors (yellow) of ±1 standard deviation either side. (b) Average campaign image with average main emission (blue), second oval position (black) with error bars (yellow), the Ganymede footprint contour (orange) and previous second oval points from (*Tomás et al.*, 2004b) (green). (c) The location in the equatorial plane of the auroral second oval (black) detected between 150-240° (in the ionosphere), and injections signatures (shaded blue) observed on 11 January 2014 (their position is consistent with e.g. (*Louarn et al.*, 2014)). The red circle shows the 15 R_J line, which is the approximate orbital path of Ganymede. The VIPAL internal field model was used to map the features (*Hess et al.*, 2011) with a CAN current sheet (*Connerney et al.*, 1981). The positive x-axis points to the Sun and the mapping is performed for 180° CML. 68

5.6 Histogram of brightness of second oval points for periods 3 days after an injection (red solid) and other days (blue outline). 71

5.7 (a) Timeseries of the number of second oval points found in each observation normalised to the number of points that fit the detection critera. The coloured bars represent large injection events on day 4 (red), 11 (green), 14 (blue). (b) The brightness of second oval points detected after injection observations. The mean brightness and standard deviation are overplotted for each observation. 72

5.8 Top panel: HST unprojected images of (a) day 11, injection signatures, and (b) day 16, second oval, showing slit intersection (white) over the images taken before spectral observation; the red line indicates the low latitude region of interest. The low latitude region on day 11 is interpreted as a large injection signature. On day 16, the low latitude region contains the main emission and second oval feature - the lowest latitude portion could be the second oval. Bottom panel: Electron energy and energy flux for (c) day 11 and (d) day 16 for the low latitude points only. The expected relation between the mean energy and energy flux according to the Knight relation is shown for different source populations, $N_0 = 0.0026$/cc (solid), $N_0 = 0.001$/cc (dashed), $N_0 = 0.01$/cc (dot dashed). The main emission is expected to obey the relation described by these lines (*Gustin et al.*, 2016) 75

6.1 Solar wind velocity(top), IMF strength (middle) and solar wind density (bottom) over the period of interest in 2007 measured using a propagated mSWiM model to match New Horizons data. These are found by shifting a solar wind propagation model (mSWiM) by 2.1 days to match New Horizons data after *Nichols et al.* (2009a); *Clarke et al.* (2009). Labels in blue show the times of the HST observations in Feburary and March, with uncertainty window of ± 40 h. 86

6.2 Twelve panels showing polar-projected HST image of Jupiter's northern FUV aurora over the CIR impact during February (panels A-F) and March (panels G-L). For each image the exposure time was between 30 and 100 s. The Central Meridian Longitude (CML) is shown. The image is displayed with a log intensity scale saturated at 1000 kR. The grey lines indicate a 10° 10°jovicentric latitude-system III longitude grid. The image is oriented such that 180° λ_{III} is directed toward the bottom and $lambda_{III}$ labels are displayed in white. 87

6.3 Six polar projected images taken with the HST, with log intensity scale saturated at 1000 kR. The gray lines indicate a 10° 10° jovicentric latitude system III longitude grid. The image is oriented such that 180° system III longitude is directed toward the bottom and labels are displayed in gray. (Top panel) Day 55 images (A) before and (B) during enhancement and (C) showing the difference between the files (pink) superimposed on the enhanced image (Bottom panel) Day 64 images (D) before and (E) during enhancement and (F) showing the difference between the files (pink) superimposed on the enhanced image. 92

6.4 Three polar projected images taken with the HST on day 63 showing the pulsating spot, with log intensity scale saturated at 1000 kR. The gray lines indicate a 10° 10° jovicentric latitude system III longitude grid. The image is oriented such that 180° system III longitude is directed toward the bottom and labels are displayed in gray. The spot is in (a) enhanced (10:26 UT) at around 172° longitude and 64° latitude, (b) faded (10:31 UT) and (c elongated polewards (10:33 UT) 93

6.5 A timeseries of auroral brightness (kR) estimated from the projected image from day 63 of the pulsating spot (red) and day 64 of the large flashing region (black). Local peaks (red) and troughs (blue) have been highlighted. There is a 2-3 minute periodicity. 94

6.6 Polar projection of DOY 7 (07:26 UT) from the 2014 HST campaign. The image is in grey, with the 'halo' region in blue, the 'core' region in orange. 95

6.7 The number of points above a 350 kR threshold v CML of images in the 2014 campaign. The red points show large flare activity. The dashed line is scaled against the y axis and shows the fraction of the total region of interest on view at each CML; after about 125° the whole of the region of interest (in this case, the high latitude region) can be seen. 96

6.8 The number of points above a 350 kR threshold v CML of images from days showing large scale flare activity (days 7 and 10). The left panel shows the number of points from the halo region and the right panel shows the core region. 97

6.9 Equatorial mapping of points in the X-Y plane of points over the campaign on closed field lines from the high latitude region. The mapping used the VIPAL internal field model and the flux-equivalence mapping method of *Vogt et al.* (2011, 2015). The magnetopause is the *Joy et al.* (2002) compressed and expanded magnetopauses. There is a clear duskward preference for the mapping. 98

7.1 Six polar projected images taken with the HST, with log intensity scale saturated at 400 kR. For each image the exposure time was 100 s. The grey lines indicate a 10° × 10° jovicentric latitude-system III longitude grid. The image is oriented such that 180° system III longitude is directed toward the bottom and labels are displayed in grey. Top row, left to right, a) Injection event, day 4 01:10 UT, average main emission position for campaign in gold, b) day 6 02:35 UT, c) day 7 07:16 UT. Bottom row, left to right, d) Injection event, day 11 00:31 UT, e) day 13 22:39 UT, f) After HOM emission, indicator of in injection event, on day 14, day 16 00:03 UT. 105

7.2 Six panels showing polar-projected HST image of Jupiter's northern FUV aurora over the CIR impact during February. For each image the exposure time was between 30 and 100 s. The Central Meridian Longitude (CML) is shown. The image is displayed with a log intensity scale saturated at 1000 kR. The grey lines indicate a 10° 10°jovicentric latitude-system III longitude grid. The image is oriented such that 180° $_{III}$ is directed toward the bottom and $_{III}$ labels are displayed in white. 106

List of Tables

5.1 System III Longitude and Latitude of Mean Second Emission 69

6.1 A table summary of the Mid-Low latitude and high latitude of the Jovian UV aurora to a CIR event, with indicated time markers for Onset, Magnetospheric Expansion and Solar Wind Rarefaction. Many of these responses have been noted previously by (*Clarke et al.*, 2009; *Nichols et al.*, 2007, 2009a; *Nichols et al.*, 2017a). There is some overlap so some panels are referenced twice. 90

Abbreviations

CML	**C**entral **M**eridian **L**ongitude
IPT	**I**o **P**lasma **T**orus
CIR	**C**orotating **I**nteraction **R**egion
UV	**U**ltraviolet
LT	**L**ocal **T**ime
HST	**H**ubble **S**pace **T**elescope
KH	**K**elvin **H**elmholtz
ME	**M**ain **E**mission
FAC	**F**ield **A**ligned **C**urrent

‘Ok, let’s just go through that one more time...’

- Sarah Victoria Badman

Chapter 1

Introduction

Jupiter is a rapidly rotating gas giant whose aurorae are powerful enough to be detected and studied from Earth. Its magnetic field is the strongest planetary field in the solar system, giving rise to its vast magnetosphere. The magnetosphere is populated with internally produced plasma from its volcanic moon, Io. The plasma can be accelerated along the magnetic field lines to cause precipitation of energetic particles into the atmosphere; it is these charge neutral collisions that produces the aurora observed. This thesis contributes to the understanding of Jupiter's plasma transport dynamics and focuses predominately on the middle to inner magnetosphere. However, like all planets in the solar system, Jupiter is immersed in the dynamic flow of solar wind. The solar wind can act as an external plasma source and transport driver. It is therefore important to briefly consider the interaction of the solar magnetic field and the magnetic field of a planet. This is outlined below, together with an introduction to terms such as 'plasma' and 'magnetosphere' in their wider context.

1.1 The Sun and Solar Wind

The Sun is our solar system's predominate source of energy. The release of energy by nuclear fusion occurs in the Sun's core, where there are sufficient temperatures and pressures. At these temperatures the predominately Hydrogen and Helium gases, which comprise the Sun, are ionised to form a state of matter called plasma. The magnetic field, generated by the solar dynamo, is known to flip every 11 years and varies with the solar activity (e.g. *Kivelson and Russell* (1995); *Cole* (2002)). The Sun can be understood as a rotating magnetised plasma body, whose outer atmosphere has a temperature of $\sim 10^6$ K still high enough to ionise and cause a charge neutral plasma.

The solar wind is a low density plasma that fills the solar system; assuming the Sun is in hydrostatic equilibrium and then applying force balances, we find that at large radius, the gas pressure of the solar wind is around $\sim 2\times10^{-5}$ Nm^{-2}. This is high compared to the region of space around it (the local interstellar medium). The difference in pressure causes the solar material to continuously flow into the interplanetary medium - this flow is known as the solar wind. The solar wind is composed primarily of protons and electrons with trace helium and heavier ions. The solar wind dynamic pressure P_{SW} can be estimated by $P_{SW} = \rho \mathbf{v}^2$ (where ρ is the density and $\mathbf{v}$ is the solar wind speed) and the density falls as r^{-2}, where r is distance from the Sun. Using a solar wind speed of 450 km/s, Jupiter's distance from the Sun of 5.2 AU and the solar wind proton density at Earth of 6.6 cm^{-3} (*Hundhausen*, 1995) gives an approximate dynamic pressure of 0.08 nPa at Jupiter.

The solar magnetic field is carried out by the solar wind plasma giving rise to the interplanetary magnetic field (IMF). Since the Sun rotates, the IMF is wound into a spiral (*Parker*, 1958) with a periodicity of around 27 days. Fluctuations in the solar wind will therefore also rotate in the IMF, so similar structured solar wind will pass over obstacles to the solar wind, i.e. planetary magnetospheres, with the same periodicity.

The Sun's magnetic field is approximately dipolar during solar minimum but during solar maximum it is more disordered. This means that the radial component of the magnetic field is (presently) directed away from the Sun in the northern hemisphere but towards it in the southern hemisphere. This gives rise to a thin current sheet at the magnetic equator called the 'Heliospheric Current Sheet'. The sheet is also wound on the Parker Spiral and undulates above and below the equatorial plane of the solar system due to the tilting of the magnetic field of the Sun. The tilt maximises with solar cycle. In addition, as the solar cycle maximises and more frequent events such as flares and coronal mass ejections occur, the sheet and the spiral both become disordered resulting in structured outflows. The Parker Spiral is illustrated artistically in Fig 1.1.

Co-rotating Interaction Regions (CIRs) are one such outflow structure. The flow from the Sun tends to occurs in a fast ($>$ 650 km/s) and slow ($<$ 400 km/s) regimes. During solar minimum, fast flow occurs close to the poles and slow flow closer to the equator, but around solar maximum this can change. Any one longitude and latitude point on the solar surface will experience outflow of both regimes because of the solar rotation.

Figure 1.1: An artist's impression of the Heliospheric Current Sheet configuration in interplanetary space. Courtesy NASA.

As a result, in the solar wind structured slow then fast or fast then slow solar wind speed regimes exist. When a fast stream catches a slow stream, a compression region is formed and when slow wind follows fast wind a rarefaction region is formed. Further from the Sun, these cause density perturbations and 'shocks' in the solar wind. In the solar wind frame, a reverse shock forms as the depleted region propagates sunward and a forward shock when the denser region propagates anti-sunward. These regions also show variations in their magnetic field strength. The whole structure rotates with the Sun, and some, if stable, will survive multiple rotations. The structures are therefore called Co-rotating Interaction Regions. These are demonstrated in Fig 1.2.

1.2 Frozen-in-Flow and Magnetic Reconnection

It is equally correct to think of a plasma carrying a magnetic field or the field carrying the plasma - if the plasma energy dominates the field energy (i.e. $\frac{1}{2}\rho\mathbf{v}^2 > \frac{\mathbf{B}^2}{2\mu_0}$), the plasma is described as carrying the field. Otherwise, the field is said to carry the plasma. The 'Frozen-in-Flow' approximation allows a description of the forces on the charged particles and thereby their motion. Their motion along one field line is described by $\mathbf{F} = q\mathbf{v} \times \mathbf{B}$, where q is the particle charge, $\mathbf{v}$ is the velocity vector, $\mathbf{B}$ is the magnetic field vector and

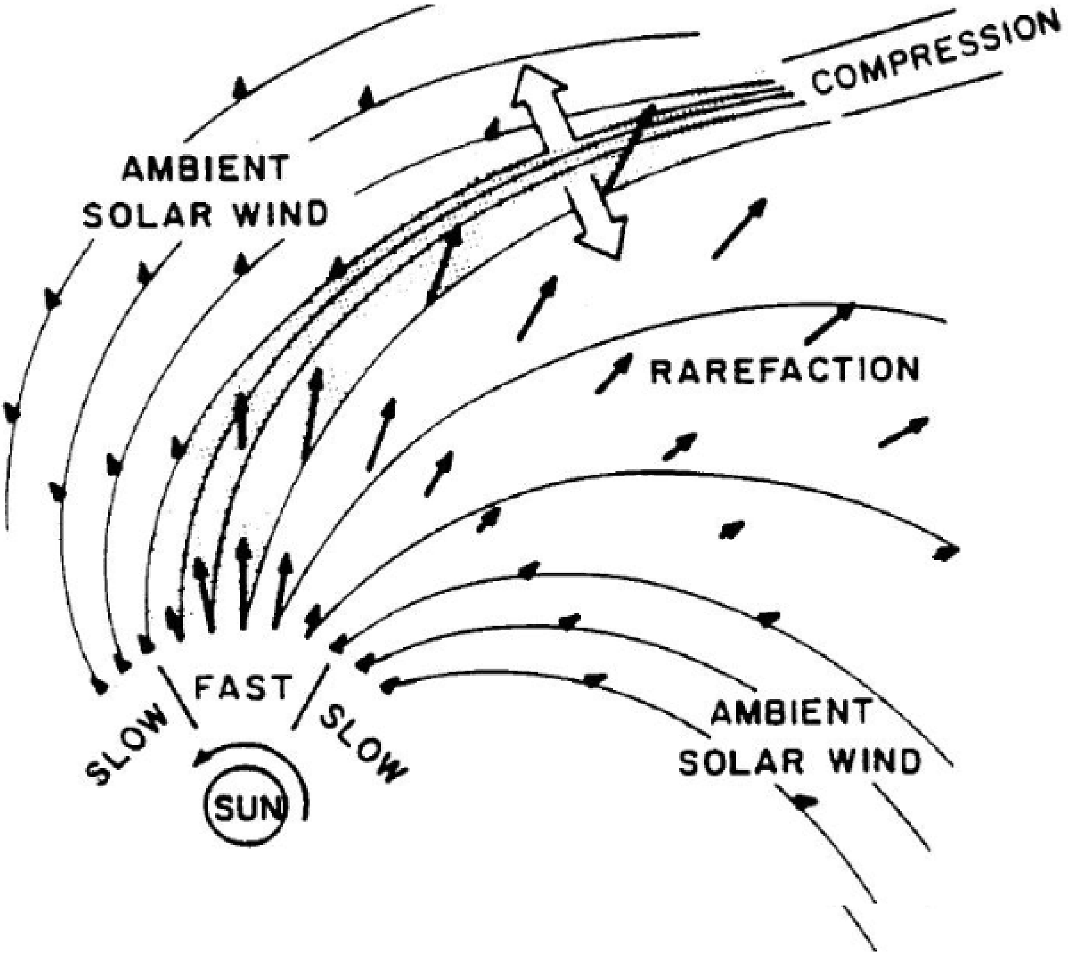

FIGURE 1.2: Schematic of a corotating interaction region in the solar equatorial plane. The solid black lines represent magnetic field lines and arrows show the outflow of the solar wind. After (*Gosling and Pizzo*, 1999).

F is the force vector. The particles thus have a helical motion up and down the field, since by taking the cross product of the velocity and magnetic field, motion is always perpendicular to both. So long as the particle doesn't fall into the 'loss cone', it will remain in the field line. When considering additionally an electric field perpendicular to the magnetic field, the particles will have the drift velocity perpendicular to both fields in accordance with $\mathbf{v_{drift}} = \frac{\mathbf{E}\times\mathbf{B}}{B^2}$. Under these three motions, Frozen-in-Flow is obeyed and the particle's gyrocentre (the centre point around which is gyrates) will remain on the same field line. When the magnetic field itself changes, forces other than these come into play. A change in the field strength perpendicular to the field direction comparable to the particle's radius of gyration (its gyroradius) will cause the particle to drift in the direction of higher field as it gyrates (experiencing a stronger field one side of its orbit than the other). Its velocity due to the gradient in the magnetic field, $\mathbf{V}_{\nabla B}$, is:

$$\mathbf{V}_{\nabla B} = \frac{mv_{\perp}^2}{qB^2}\frac{\mathbf{B} \times \nabla B}{B} \tag{1.1}$$

where $v_{\perp}$ is the velocity perpendicular to the field line.

Alternately a curvature of the magnetic field induces an centrifugal acceleration of the particle, giving the drift:

$$\mathbf{V}_{curv} = \frac{mv_{\parallel}^2}{qB^2}\frac{\mathbf{R_C} \times \mathbf{B}}{R_C^2} \tag{1.2}$$

where $v_{\parallel}$ is the velocity parallel to the field line and $\mathbf{R_C}$ is the field curvature radius.

Gradient and curvature drift both act proportionally to a particle's energy and in opposite directions depending on the particle's positive or negative charge. When they act, the Frozen-in-Flow approximation fails and the particles can move off their field lines (*Kivelson and Russell*, 1995; *Baumjohann and Treumann*, 2012).

As two plasmas or field regions encounter each other, due to the Frozen-in-Flow theorem (that plasmas must remain on their field line and vice-versa), a boundary between the two regimes forms. Over this boundary, there is a change in the magnetic field strength and direction, so by Ampère's law, a current flow forms, known as the current sheet. The equation describing the motion of the magnetic field can be derived.

Starting with Ohm's law for plasma with conductivity σ and $\mathbf{j}$ is current density:

$$\mathbf{E} + \mathbf{v} \times \mathbf{B} = \frac{\mathbf{j}}{\sigma} \tag{1.3}$$

we then rearrange and substitute Faraday's Law (curl$\mathbf{E} = -\frac{\partial \mathbf{B}}{\partial t}$) to come to:

$$\frac{\partial \mathbf{B}}{\partial t} = \nabla \times (\mathbf{v} \times \mathbf{B} - \frac{\mathbf{j}}{\sigma}) \tag{1.4}$$

Substituting for $\mathbf{j}$ using Ampère's Law (curl$\mathbf{B} = \mu_0 \mathbf{j}$) for the non-relativistic case (therefore neglecting displacement current) gives:

$$\frac{\partial \mathbf{B}}{\partial t} = \nabla \times (\mathbf{v} \times \mathbf{B}) - \frac{\nabla \times (\nabla \times \mathbf{B})}{\mu_0 \sigma} \tag{1.5}$$

Using the vector identity, $\nabla^2 \mathbf{A} = \nabla(\nabla \cdot \mathbf{A}) - \nabla \times (\nabla \times \mathbf{A})$, we find:

$$\frac{\partial \mathbf{B}}{\partial t} = \nabla \times (\mathbf{v} \times \mathbf{B}) + \frac{\nabla^2 \mathbf{B}}{\mu_0 \sigma} - \frac{\nabla(\nabla \cdot \mathbf{B})}{\mu_0 \sigma} \tag{1.6}$$

Finally, since there are no magnetic monopoles ($\nabla \cdot \mathbf{B} = 0$), we find the motion of magnetic field can be described by the so-called induction equation:

$$\frac{\partial \mathbf{B}}{\partial t} = \nabla \times (\mathbf{v} \times \mathbf{B}) + \frac{\nabla^2 \mathbf{B}}{\mu_0 \sigma} \tag{1.7}$$

The first term after the equality describes the convective transport, representing how the field moves under the $\mathbf{E} \times \mathbf{B}$ drift. The second term is the diffusion term. Since this form can be bulky to handle, it is often written in a dimensional form:

$$\frac{B}{\tau} = \frac{vB}{L} + \frac{B}{L^2 \mu_0 \sigma} \tag{1.8}$$

where B is the average magnetic field strength, τ is the characteristic time scale for magnetic field variations, v is the average plasma velocity and L is the characteristic length scale for magnetic field variations. The ratio of the convective and diffusion terms (first and second terms respectively) is known as the Reynolds number ($R_m = \mu_0 \sigma v L$). For the case where the Reynolds number is much less than one, the diffusion term dominates and the Frozen-in-Flow approximation breaks down. When this happens, magnetic fields are allowed to diffuse across the thin current sheet. The field lines become distorted/twisted and so may ‘break’ and ‘reconnect’ in a process known as magnetic reconnection. The newly reconnected field lines will straighten according to the magnetic tension forces acting and will be accelerated away from the reconnection site.

1.3 Planetary Magnetospheres

Some planets, such as Earth and Jupiter, have an intrinsic magnetic field. When the solar wind encounters this sort of obstacle, the planetary magnetic field forms a cavity in the solar wind. This cavity is thus shaped by the solar wind and is called the magnetosphere (*Gold*, 1959); the ‘dayside’ (facing the Sun) has a closed shape but the ‘nightside’ has a long extended tail. This can be imagined as the long wake around a rock as an obstacle in a stream. The supersonic flow of the solar wind over the dayside boundary of the magnetosphere causes the bow shock to form. The magnetopause is formed at the point of magnetic and dynamic pressure balance between the solar wind and the magnetosphere; the magnetopause will move closer to and further from the planetary body as the solar wind pressure increases and decreases. These two regions are marked on Fig 2.4.

The magnetopause standoff distance (the point of magnetic and dynamic pressure balance) can be found by equating the solar wind ram pressure (the particle pressure dominates the thermal or magnetic pressure) ($P_{sw} = 2\rho v^2$) and the magnetic pressure of the planet ($P_{mp} = \frac{B_{mp}^2}{2\mu_0}$ and B_{mp} is twice the dipole field $B_{dipole} = 2B_{eq}(\frac{r}{R_p})^3$). At $r = R_{mp}$:

$$\frac{B_{mp}^2}{2\mu_0} = \frac{2B_{eq}^2}{\mu_0}(\frac{R_{mp}}{R_p})^6 \tag{1.9}$$

So therefore:

$$\frac{R_{mp}}{R_p} = (\frac{B_{eq}^2}{\mu_0 \rho v^2})^{\frac{1}{6}} \tag{1.10}$$

Using $B_{eq} = 500{,}000$ nT, proton density $\rho = 0.2$ cm^{-3} and velocity of 400 km/s the magnetopause standoff distance at Jupiter is $\sim 40\ R_J$. For comparison, at Earth, for $B_{eq} = 31{,}000$ nT, proton density $\rho = 5$ cm^{-3} and a velocity of 400 km/s, the magnetopause is at $\sim 10R_E$. Statistical models based on observations place the magnetopause between 63 and 92 R_J (*Joy et al.*, 2002), highlighting the downfall of this approximation which neglects the thermal and magnetic pressures of Jupiter's magnetosphere.

Reconnection between solar wind field lines and planetary field lines can happen at the dayside magnetopause. This has the effect of injecting solar wind plasma onto planetary field lines, thereby adding solar plasma to the system. In a convection driven system (such as the Earth but unlike Jupiter, see below), the field lines will convect over the polar cap of the planet and then may also reconnect in the magnetotail (on the nightside), injecting plasma planetward. The field lines will then convect around to the dayside either side of the planet, completing a twin-cell motion in the polar cap. This transport cycle is known as the 'Dungey' system after Jim Dungey, who first proposed it (*Dungey*, 1961, 1963). The Dungey cycle dominates at Earth, but in rapidly rotating magnetospheres or magnetospheres where there are internal plasma sources exerting pressure, such as that of Jupiter or Saturn, these processes can dominate the magnetospheric dynamics.

The details of the internally driven magnetospherics at Jupiter are discussed in chapter 2, particularly with respect to the dynamics of an internal plasma source outflow. Here, we derive an expression to compare the co-rotation and the convection effects. Considering first the convection system, we can set up the following co-ordinate system: X points towards the sun from the tail, Y points from dawn to dusk and Z points (at Earth) up out the equatorial plane aligned with the magnetic field axis. **B** the magnetic field points along the Z direction and therefore the associated electric field **E** points in the Y direction. We can therefore describe the convective electric field as $\mathbf{E_{conv}} = E_0\hat{\mathbf{y}}$ and the magnetic field can be written as $\mathbf{B} = B_{eq}(\frac{R_p}{r})^3\hat{\mathbf{z}}$, where B_{eq} is the equatorial magnetic field strength at distance r and R_p is the planetary radius. Finding, then, the velocity using $\mathbf{v} = \frac{\mathbf{E}\times\mathbf{B}}{B^2}$ at the equator:

$$\mathbf{v_{conv}} = \frac{\mathbf{E_{conv}} \times \mathbf{B}}{B^2} = \frac{E_0}{B_{eq}}(\frac{r}{R_p})^3\hat{\mathbf{y}} \times \hat{\mathbf{z}} = \frac{E_0}{B_{eq}}(\frac{r}{R_p})^3\hat{\mathbf{x}} \tag{1.11}$$

The corotation flow of the plasma and field moving with the planet can be described by:

$$\mathbf{v_{corot}} = r\omega_p\hat{\phi} \tag{1.12}$$

where ω_p is the angular velocity of the planet and $\hat{\phi}$ is the azimuthal unit vector in the direction of rotation. On the dusk side where the velocities both have the opposite direction, there will be a stagnation point R_{sp}. To find whether convection or corotation dominates the system, we should determine whether the stagnation point lies within the magnetosphere (so for some r, $r < R_{sp}$, convection will dominate for some regime inside the magnetosphere) or whether the stagnation points lies outside the magnetosphere (for all r, $r > R_{sp}$, where corotation will dominate). Equating the two expressions for velocity for $r = R_{sp}$ at the stagnation point:

$$\frac{E_0}{B_{eq}}(\frac{R_{sp}}{R_p})^3\hat{\mathbf{x}} = R_{sp}\omega_p \tag{1.13}$$

And by rearrangement:

$$\frac{R_{sp}}{R_p} = (\frac{\omega_p B_{eq} R_p}{E_0})^{\frac{1}{2}} \tag{1.14}$$

The stagnation point should then be compared to the magnetopause, R_{mp}. For the case of Earth, $\omega_p = 7 \times 10^{-5}$ rads^{-1}, B_{eq} = 31,000 nT, R_p =6400 km and E_0 =2×10^{-4} Vm^{-1} (estimated using $\mathbf{E} = -\mathbf{v} \times \mathbf{B}$), so the stagnation point lies at ∼8.5 R_E compared to the magnetopause at $\sim$10 R_E so the planet is convection dominated. For the Jovian case, $\omega_p = 1.7 \times 10^{-4}$ rads^{-1}, B_{eq} = 500,000 nT, R_p =71,400 km. The convective electric field can be estimated by taking the Dungey-cycle potential (0.4 MV) over the cross tail length (15 R_J) (*Acuña et al.*, 1983; *Badman and Cowley*, 2007) to give $E_0 = 4\times10^{-5}$ Vm^{-1}, so the stagnation point lies at $\sim$390 R_J compared to the magnetopause of $\sim$40 R_J (even the *Joy et al.* (2002) statistical models place the magnetopause between 63 and 92 R_J) so the planet is corotation dominated.

This introductory chapter has looked from the large scale IMF generated by the Sun and briefly assessed some of the differences of the interaction of the IMF with Earth and Jupiter. Some of the basic plasma physics has also been introduced in these assessments.

Chapter 2

Jupiter

This chapter outlines the current understanding of the Jovian system, considering the magnetospheric structure and dynamics, the magnetic field configuration, what is known about ultraviolet (UV) auroral signatures in the Outer Emission, Main Emission and Polar Emission regions and the Radio emissions.

2.1 Jupiter's Magnetospheric Structure

This section gives an overview of the relevant magnetospheric physical structures, starting in the inner magnetosphere closest to the planet, working down the nightside magnetotail, and then to the dayside magnetopause. It also gives an overview of Jupiter's magnetic field configuration, including various field modelling attempts made by the community.

2.1.1 Inner, Middle and Outer Magnetospheric Structure

Much of Jupiter's magnetospherics are determined by its internal plasma source: the volcanic moon Io (orbiting at 5.9 R_J) has surface lava lakes, volcanic pits and volcanoes, each with various energy release rate, temperature and lava type etc. (*Davies*, 2007). The volcanic output populates the atmosphere of Io where the particles are sputtered and picked up (e.g. *Johnson and Leblanc* (2001)). The rates at which these processes occur are a current research topic (*Yoneda et al.*, 2009, 2010). The plasma populates the Io Plasma Torus (IPT), which is a dense cold plasma region from 5 - $8R_J$. For the purpose of this thesis, we consider the population of the IPT to be steadily maintained, unless perturbed due to interchange processes (see below), and to comprise of heavy ions and electrons.

The plasma torus itself can be well described using radial and longitudinal profiles of electron density, temperature and relative ion abundances (*Tsuchiya et al.*, 2015; *Yoshioka et al.*, 2017). These parameters have been shown to change with solar wind variations; it is thought that the outer regions of the magnetosphere and these inner regions are linked by an electric field (*Murakami et al.*, 2016). It is common to estimate the plasma outflow rate as $\sim$ 1000 kg/s (with half the contributions from neutrals and half from ions), though this figure is under constant revision as more observations are made - see appropriate chapters in, for example, *Bagenal et al.* (2007). It has recently been shown with the Hisaki satellite that the inflow and outflow rates through the outer torus differ and may vary with volcanic activity (*Yoshioka et al.*, 2017). Hot plasma inflows from the magnetosphere have been shown to impact the IPT, so act as another plasma source and perturbation (*Yoshikawa et al.*, 2016). Interchange, a process where hot sparse plasma and cold dense plasma transfer position in order to conserve magnetic flux, occurs at the edge of the IPT. Hot plasma injections are also detected in this region. These two processes are discussed in section 2.2.

Whistler mode waves are pervasive in the inner magnetosphere (*Menietti et al.*, 2016). Wave-particle interactions in the region 10-17 R_J are thought to scatter electrons into a field-aligned distribution, leading to a transition region at these distances where the electron pitch-angle distribution (PAD) changes (*Tomás et al.*, 2004a). The PAD boundary is thought to be a part of the Nishida recirculation process whereby energetic particles radially diffuse inwards in the equatorial plane, pitch angle scatter in the inner magnetosphere, latitudinally diffuse at low altitudes to larger L-shells and are so recirculated to radially distant regions (*Nishida*, 1976; *Fujimoto and Nishida*, 1990).

In the middle magnetosphere (15-40 R_J), Iogenic plasma continues to flow outwards as it is driven centrifugally outward and interchange process take place. As the distance from the planet increases, the angular speed of the plasma falls behind corotation. A field-aligned current system that closes through radial currents in the equator is required to transfer angular momentum (through the $\mathbf{j} \times \mathbf{B}$ force) in order to maintain partial corotation. This system is shown in Fig. 2.1.

It is thought that the angular speed of plasma outflow from the IPT drops as it moves

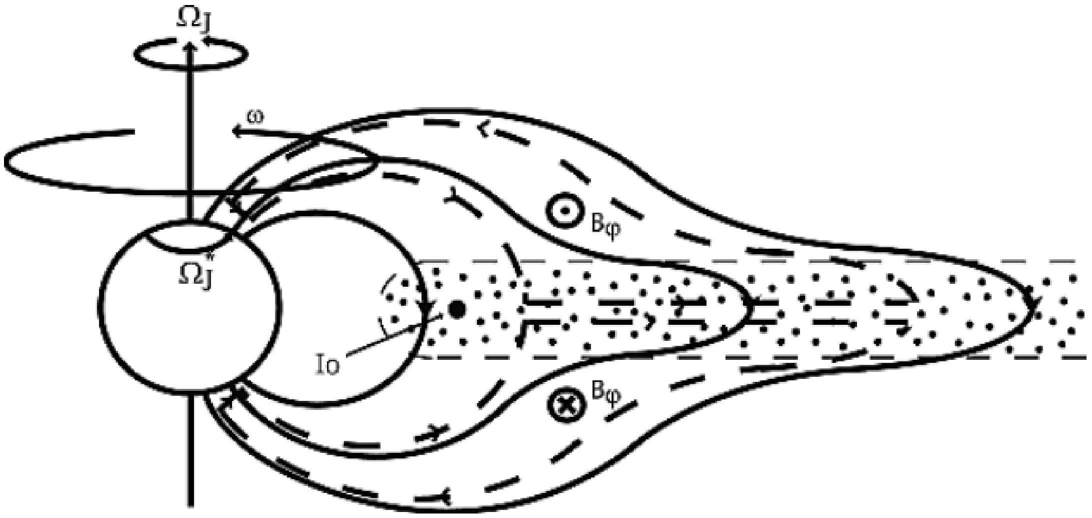

Figure 2.1: Schematic in the merdional plane in the inner to middle magnetosphere of momentum supplied to sub-corotating plasma in the equatorial plane from the planet. The arrowed solid lines indicate magnetic field lines, curved outward the plane of the page by azimuthal currents in the middle magnetosphere current sheet. Iogenic plasma is shown by the dotted region. Three separate angular velocities associated with the system are that of the planet Ω_J, a particular shell of field lines ω, and of the neutral upper atmosphere in the Pedersen layer of the ionosphere, Ω_J^*. The opposite current represented by the dashed arrow. After (*Cowley and Bunce*, 2001, 2003).

radially away due to conservation of momentum. The plasma remains bound to the magnetic field as it moves (obeying Frozen-in-flow conditions, here the field is frozen into the plasma), leading to the stretched and bent-back field configuration. The azimuthal component of the magnetic field B_ϕ, accounting for the bend-back, is directed opposite to the direction of planetary rotation in the northern magnetic hemisphere and in the direction of planetary rotation in the southern hemisphere, reversing in the magnetic equatorial plane. Due to Ampère's law, a radial current threads this loop. An upward FAC is thought to connect the radial current in the IPT to the ionosphere, where Pedersen currents flow and complete the circuit with the return FAC. Pedersen currents flow perpendicular to the magnetic field but parallel to the electric field. The resulting **j** x **B** forces from the currents (which communicate the momentum transfer) in the equatorial plane and ionosphere act to spin up and de spin the plasma in the equatorial plane and ionosphere respectively. This transfers momentum to the plasma in the magnetosphere from the planetary atmosphere. The upward current produces Jupiter's auroral main emission (*Hill*, 2001; *Cowley and Bunce*, 2001). Its primary variability corresponds to changes in mass loading and mass outflow rate in the middle magnetospheric 'corotation breakdown region' (*Nichols*, 2011; *Ray et al.*, 2012), but also depends on the ionospheric conductivity (*Nichols and Cowley*, 2003, 2004).

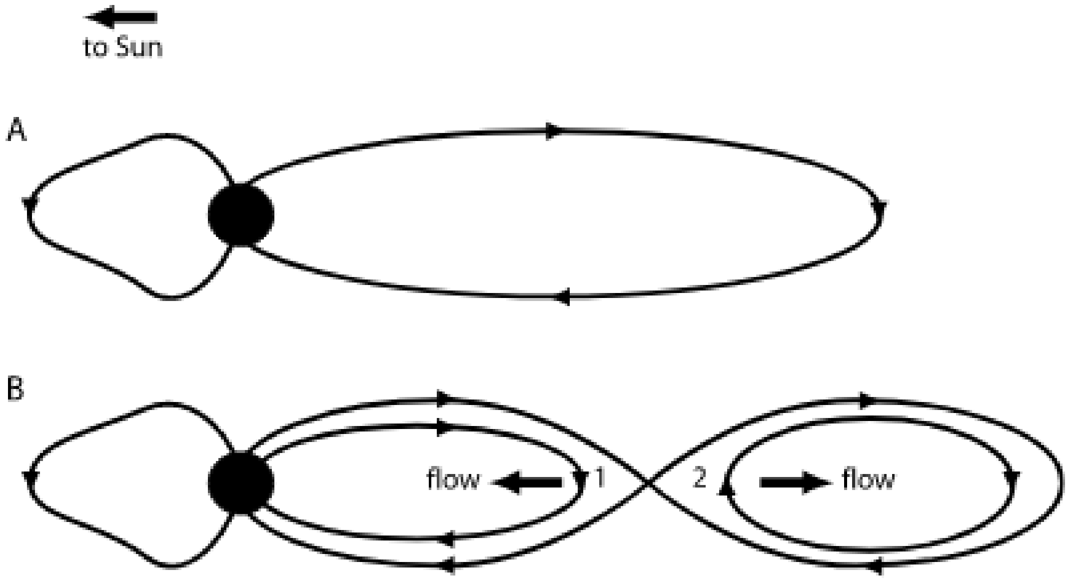

Figure 2.2: Schematic of the reconnection in the meridonal plane. Panel a shows the stretched field after mass loading from Io has stretched the field lines the plasma is attached to in the radial direction (aside from the current sheet). Panel B shows the field reconnecting and consequent plasma flows radially away from the reconnection site. The field has dipolarised and the magnitude of B_θ has increased, positively planetward of the reconnection site and negatively tailward of it. After (*Vogt et al.*, 2010; *Vogt et al.*, 2014).

In the outer magnetosphere (>40 R_J), the magnetic field is stretched by the plasma trapped with it as the plasma is driven centrifugally from the planet. This eventually leads to field collapse and reconnection (*Vasyliunas*, 1983). Reconnection results in planetward flows of very hot, tenuous plasma and tailward flows, known as 'plasmoids' (e.g. *Jackman et al.* (2011)), as Iogenic plasma is ejected from the system (*Kronberg et al.*, 2005; *Vogt et al.*, 2010). Fig. 2.2 shows the field stretching, collapse and plasmoid release. The statistical survey of *Vogt et al.* (2010) showed that the reconnection location in the tail is placed at a radial distance of around 90 R_J. Small auroral spots, known as polar spots, are associated with the planetward flow of dipolarised magnetic field lines following reconnection in the magnetotail (*Grodent et al.*, 2004; *Radioti et al.*, 2008a, 2010, 2011; *Ge et al.*, 2010). The return flow plasma is energised by an electric field generated by the reconfiguration of the field (*Mitchell et al.*, 2009). The process of plasma loading from Io, field collapse and reconnection, plasma loss downtail and hot return flow as described in the preceeding paragraphs is known as the 'Vasyliunas cycle' or the internally driven cycle of mass transport (*Vasyliunas*, 1983). The associated flowlines are shown in Fig 2.3.

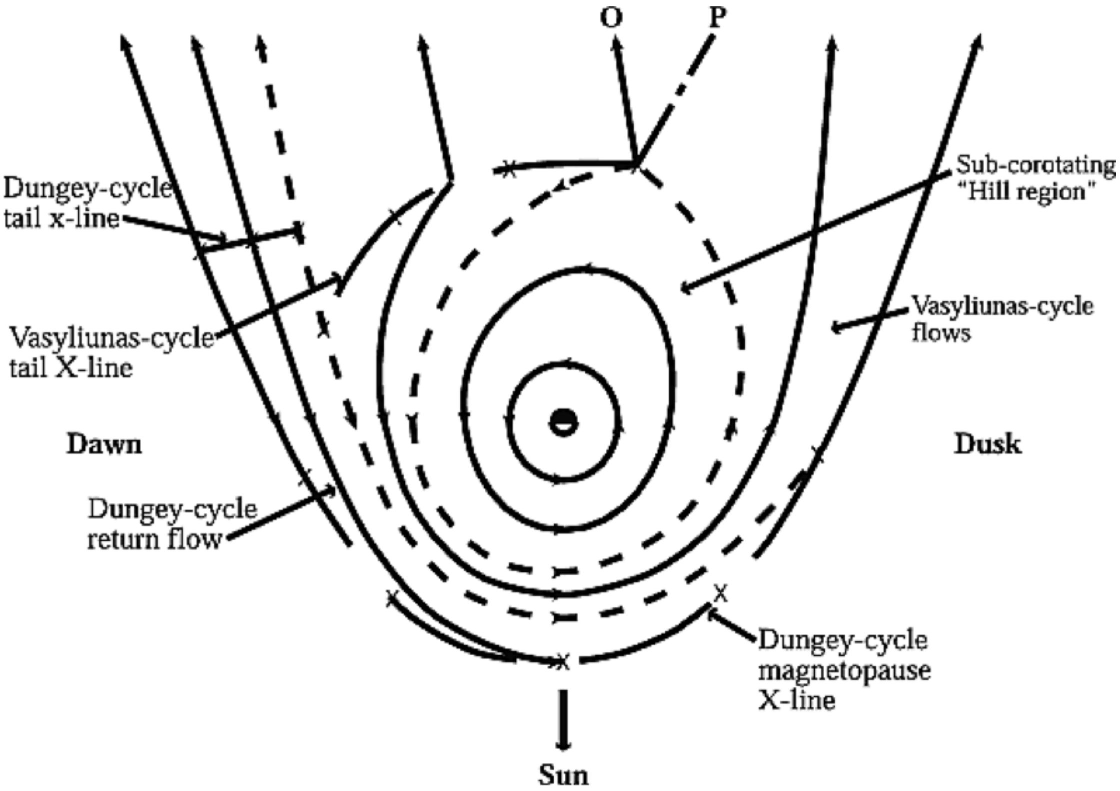

FIGURE 2.3: Schematic of the plasma flowlines (solid) in the equatorial plane. Dashed lines show the boundaries of flowlines that act in the co-rotation (inner) and convection driven (outer) regimes. The Dungey and Vasyliunas reconnection lines are marked with 'X's. 'O' marks the formation point of the plasmoid created by Vasyliunas reconnection and 'P' marks its outer bound, which asymptotes to the dusk tail magnetopause. After (*Cowley et al.*, 2003; *Badman and Cowley*, 2007).

Recent work by *Bonfond et al.* (2017a) examining Juno UVS data taken over ~ 4 hours has shown that auroral injection signatures can develop in the aurora from night to around dawn local times. Towards the end of the imaging sequence a protrusion into the polar cap appears, which the authors associate with tail reconnection. The authors postulated that the plasma moves to the outer magnetosphere, causes current sheet stretching and therefore triggers tail reconnection. Their work helps constrain the timescale over which the Vasyliunas cycle may act. This describes an inner to outer transport process, as opposed to the hypothesis undertaken in chapter 4, which suggests that the reconnection inflows may also enhance injections. The work of *Mitchell et al.* (2009, 2015) suggests that these two processes are intrinsically linked.

Reconnection signatures in the tail can be clustered (*Vogt et al.*, 2014) implying reconnection events can happen in succession across field lines. As well as this, once the closed field lines closest to the equatorial current sheet have closed, reconnection may proceed onto the open field lines. *Kasahara et al.* (2011) studied the effect of reconnection on the jovian plasma sheet and found that during an extended interval of tail reconnection (up to 18 h) involving both closed and open field lines, a jet of electrons at the dipolarisation front (where the theta component of the magnetic field switches) was detected travelling planetward at 7500-17000 km/s. How much reconnection occurs on open field lines is a topic of open research. Similarly, the amount of flux closure in the nightside tail as part of any 'Dungey-cycle' (the Earth-like, solar wind 'externally' driven, plasma circulation system where flux opened on the dayside is closed in the tail (*Dungey*, 1961, 1963)) is not well restrained, but is thought to be of significance (*Badman and Cowley*, 2007). The tail reconnection processes are far from fully understood, yet must play a major role in mass balance - over a sufficiently long timescale, mass must be lost at least at the rate it is being produced internally.

The solar wind interaction at Jupiter's dayside is also not well understood. Processes like magnetic reconnection and flow-shear driven instabilities are a fundamental source of energy on the dayside of the planet. These processes are expected to map to the polar region, the interaction happening on the outermost planetary field lines. Figure 2.4 shows the basic magnetospheric field and current configurations. On the dayside: the bowshock forms the shock with the oncoming solar wind; the magnetopause is where the dynamic pressure of the solar wind balances the dynamic pressure of the magnetopause; the 'cushion region' shows the region where the magnetodisk and thus 10 hour periodicity associated with planetary rotation are absent (*Khurana et al.*, 2004). The magnetopause is considered to be very compressible, with a magnetopause standoff distance somewhere between 45 and 100 R_J (*Joy et al.*, 2002).

The nature of flux opening and closure is also not understood. There are currently three main theories: first, that Dungey-cycle reconnection opens magnetic flux at the dayside magnetopause and closes it in magnetotail reconnection (*Cowley et al.*, 2003); second, magnetic flux opened on the dayside is closed down the outer magnetospheric flanks in reconnection (*McComas and Bagenal*, 2007); thirdly, KH waves generated along the magnetopause triggers reconnection along the flanks.

The prevalence of, and ideal conditions for, reconnection at Jupiter's dayside are topics of debate and active research (*Delamere et al.*, 2015). Spacecraft measurements have shown that reconnection does occur, particularly in the case of 'flux-transfer events', (e.g. *Walker and Russell* (1985); *Huddleston et al.* (1997)). It is thought that increased plasma beta parameter (that is, the ratio of plasma pressure to the magnetic pressure) has the effect of suppressing reconnection onset due to particle drifts in the current sheet away

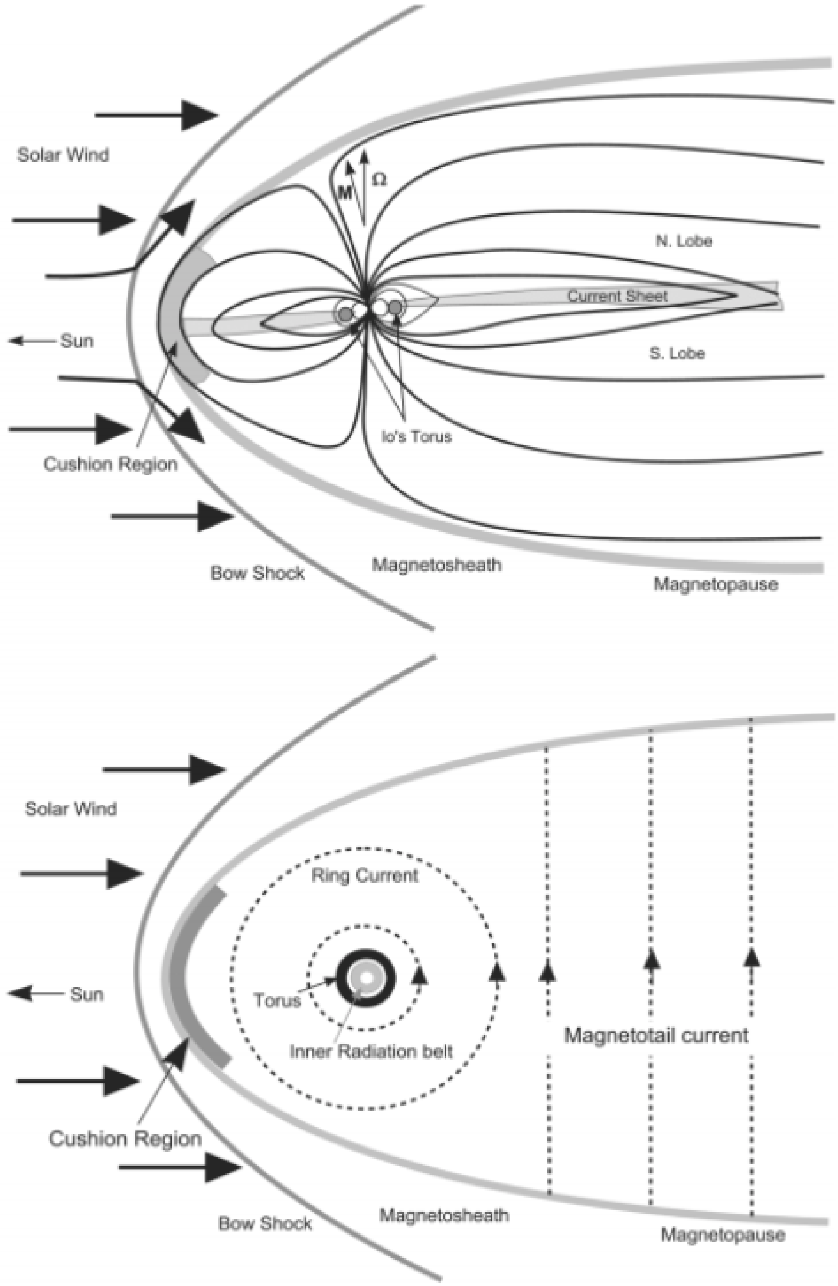

FIGURE 2.4: (Top panel) The basic magnetospheric field configuration in the noon-midnight meridian and (bottom panel) the basic current flows in the equatorial plane. After *Khurana et al.* (2004).

from the reconnection site - this is known as diamagnetic suppression (*Swisdak et al.*, 2003; *Phan et al.*, 2010, 2013). *Desroche et al.* (2012) modelled idealised magnetopause conditions and investigated their effect on reconnection. They found that, indeed, reconnection could be suppressed due to diamagnetic suppression but also that on the dawn side, reconnection was likely suppressed due to flow shears across the dawn flank, known as flow shear suppression. Pulsed dayside reconnection, possibly at the cusp (*Bunce et al.*, 2004), is thought to also occur and produce auroral signatures discussed in (*Bonfond et al.*, 2011) and in the final data chapter of this thesis.

Instablilites that develop across the magnetopause boundary due to flow shears may also play a role in transferring energy to the system (*Delamere et al.*, 2015). In this thesis the Kelvin-Helmholtz (KH) instability, which acts at the interface of two flows akin to blowing across the surface of a cup of liquid to cause waves and vortices, is the most relevant. This is because it is thought to form very good conditions for reconnection (*Delamere and Bagenal*, 2010). For example, at Earth KH vortices on the magnetopause flanks induce significant reconnection to allow flux transfer (e.g. *Hasegawa et al.* (2004); *Nakamura et al.* (2006); *Hasegawa et al.* (2009)). KH waves have been seen at Jupiter (*Huddleston et al.*, 1997) and the modelling efforts by *Desroche et al.* (2012) discussed above also suggested significant KH instability generation is possible, particularly along the dawn flank.

2.1.2 Magnetic Field Configuration

Jupiter's magnetic field rotates with the planetary body with a period of 9.925 hours as defined from the radio emissions (*Dessler*, 1983; *Russell et al.*, 2001). Its magnetic field is offset from its spin axis by about 10° (*Russell and Dougherty*, 2010).

Jupiter's magentodisk is formed by the stretching of dipolar field lines due to centrifugal forces (owing to the planet's rotation) causing radial transport of internally produced plasma. The magnetodisk prevails from around 15-20 R_J (*Krupp et al.*, 2004). As plasma generated from Io in the inner magnetosphere is driven centrifugally from the planet, its speed drops as momentum is conserved. This requires the field lines that the plasma is trapped on to also slow, and causes a deflection in the B_ϕ azimuthal component of the magnetic field producing a 'swept-back' configuration on the dawnside and 'swept-forward' on the duskside, particularly towards the outer magnetosphere. This configuration resembles a cross between the 'Parker Spiral' of the solar wind and a solar wind driven swept field configuration (like at Earth). The resulting flowline shape can be seen in Fig 2.3.

Spherical harmonic models of Jupiter's magnetic field can be used to perform 'magnetic mapping' (the tracing of a field line from the equatorial plane to the ionosphere) in order to relate auroral phenomena to equatorial sources. In this thesis, two internal field models are used for mapping close to the planet (<15 R_J) and a 'flux equivalent' mapping model is used for field lines that cross the equator further than this, since at these distances the currents can cause field stretching (see below).

An anomaly exists where the surface magnetic field is weaker with higher dipole tilt from the spin axis around the longitudes 80 °-150 ° (*Grodent et al.*, 2008a). The VIPAL internal field model (*Hess et al.*, 2011) is an update to the VIP4 internal magnetic field model (*Connerney et al.*, 1998) and is based on Voyager and Pioneer magnetic field measurements, modeling the lowest orders of the magnetic anomaly and correcting for the longitudinal position of the magnetic field lines mapping to Io's orbit. The Grodent Anomaly Model (GAM) uses the footprints of all three moons (not just Io, as in VIP4) to constrain the magnetic anomaly in the northern hemisphere. At around 15 R_J the magnetic field begins transitioning from a dipolar to a stretched configuration due to plasma sheet stretching (*Khurana et al.*, 2004). Therefore, at these distances the CAN current sheet model can be used in the mapping (*Connerney et al.*, 1981).

When choosing an internal field model, the model which provides the best match for the moon footprint of Ganymede at the feature longitude should be used (as the furthest moon footprint field line from the planet, it maps closest to the features discussed in this thesis). The same field model should be used for all features for consistency.

Vogt's 'flux equivalent' model is used to map to the outer magnetosphere (beyond 30 R_J) (*Vogt et al.*, 2011). The model traces contours of constant radial distance from the equatorial plane and finds the flux equivalent region in the ionosphere (as opposed to tracing a field line from the equatorial plane to the ionosphere). The model requires an internal field model; *Vogt et al.* (2015) recommends an internal model is chosen based on which longitude sector the feature is in. The model has been used to find the boundary between open and closed field lines in the ionosphere (by finding the lines that map to equatorial distances of greater than 150 R_J).

2.2 Interchange and Injections

A large part of this thesis is dedicated to considering how the outer and inner magnetospheric processes are linked. In the outer magnetosphere, the predominant flow is tailward as mass is lost from the system, but substantial hot inflow from reconnection has been observed (e.g. *Kronberg et al.* (2005)). Similarly, in the inner magnetosphere, flow is predominately radially outward as Iogenic plasma is driven centrifugally from the planet, but hot injections have been observed (e.g. *Mauk et al.* (2002)). The large-scale

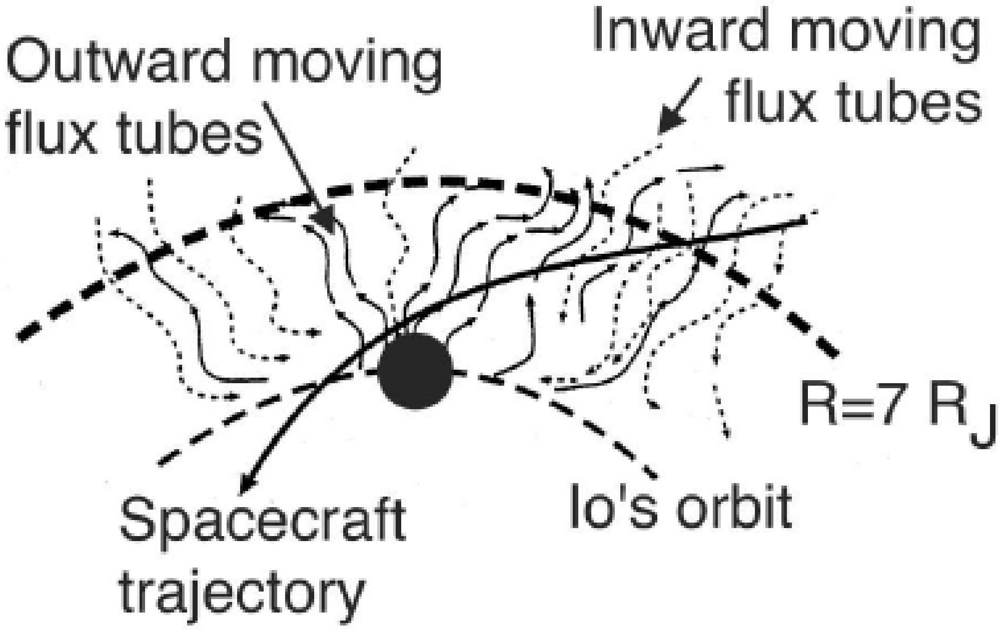

Figure 2.5: Schematic showing the detection of the interchange process at the edge of the IPT. Flux in and flux out are descibed by the dashed and solid arrows respectively. After (*Kivelson et al.*, 1997; *Krupp et al.*, 2004).

result of interaction between hot plasma inflows and the close dense plasma outflows in the middle magnetosphere is the focus of the first two data chapters of this thesis.

As the plasma in the IPT rotates around the planet, it is driven centrifugally from the planet. In the inner magnetosphere (<15 R_J), the process of interchange occurs when regions of hot, tenuous plasma are encountered by outflowing cold, dense Iogenic plasma. The tenuous and dense plasma populations interchange position in order to conserve magnetic flux. Narrow interchange fingers have been detected in the vicinity of Io (*Kivelson et al.*, 1997; *Thorne et al.*, 1997). Figure 2.5 shows the narrow threads of flux in and flux out of the IPT in the process of interchange.

The interchange instability is analogous to the 'Rayleigh-Taylor' instability, an illustrative example of which is the characteristic droplets of oil (less dense) that form when it is dropped into water (more dense). In the case of interchange as discussed here, the driving force is centrifugal, not gravitational. It involves the changing of location of hot sparse flux tubes with cold dense ones to conserve magnetic flux at their boundary, where the triggering pressure gradient exists. The hot plasma is heated adiabatically as it moves inwards (not by the electric field generated as the plasma moves radially inwards but as the magnetic field is compressed, i.e. reversibly). Interchange allows plasma to move without significantly altering the magnetic field configuration and so is the main driver of transport in the inner dipolar region of Jupiter's magnetosphere. Interchange has been observed on the IPT edges (around $\sim 7R_J$) on 'small-scales' where the dense plasma is Iogenic outflow. The observations are of, for example, changes in magnetic field measurement, wave emissions and associated phase space densities due to two different plasma populations on the torus edge *Kivelson et al.* (1997); *Thorne et al.* (1997).

Interchange has also been inferred to act on larger scales in the middle magnetosphere - in this case, the sparse plasma is the injections of hot plasma (*Mauk et al.*, 1999, 2002). These are referred to as large-scale because the auroral evidence of injection signatures appear to be associated with a large regions in the equatorial plane - it may be the case that the 'large-scale' interchange events are a series of 'small-scale' interchange events close together and that we currently lack spatial resolution to detect this using auroral images. Substructure has been found in Galileo Energetic Particles Detector (EPD) measurements (*Mauk et al.*, 1997). *Radioti et al.* (2013) showed simultaneous Energetic Neutral Atom (ENA) and auroral observations at Saturn of injection signatures evolving into several small signatures.

Large injections of hot plasma have been detected at 9-27 R_J radial distance, extending up to ~ 1 R_J in azimuth (*Mauk et al.*, 1999, 2002). Figure 2.6 is a schematic of a hot plasma injection moving planetward.

Injected electrons are expected to drift opposite to the co-rotation direction as a result of the gradient and curvature of the magnetic field. Dispersion is also expected according to the energies of the electrons (*Mauk et al.*, 2002). The auroral signatures of hot plasma injections have also been detected as diffuse patches of aurora at the corresponding latitudes equatorward of the main auroral oval (*Mauk et al.*, 2002; *Dumont et al.*, 2014); more is said about these in the introductory section describing Jupiter's auroral signatures. These injections play a role in conserving magnetic flux; *Dumont et al.* (2014) estimated that they can account for at least 18% of the inward flux required to balance the Iogenic outflow.

There are probably two plasma sources of these injection signatures; interchange driven from both the cold IPT outflow and also by hot plasma inflows from reconnection.

Studies of Saturn's magnetospheric dynamics have revealed the presence of a plasmapause at the boundary of the nightside internally driven reconnection inflow and the dense inner magnetospheric plasma (*Thomsen et al.*, 2015). Evidence of interchange

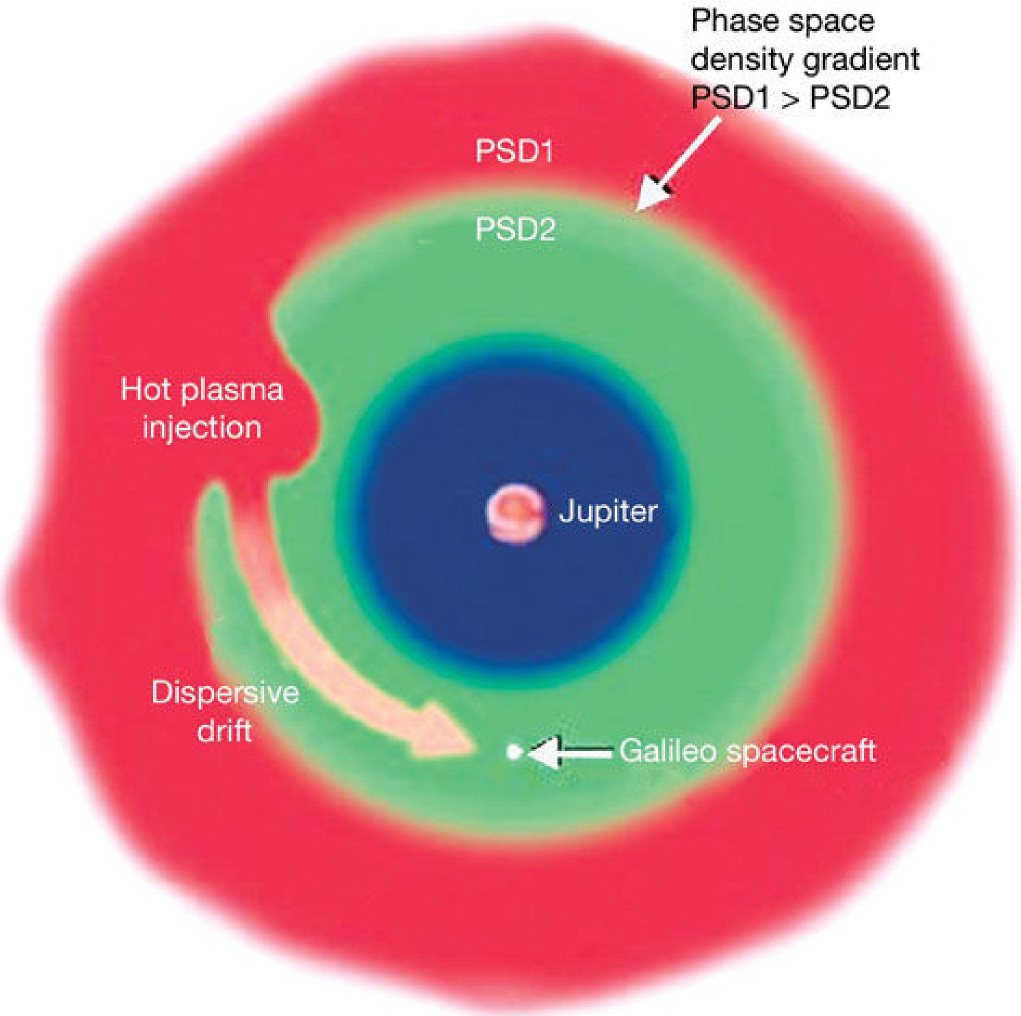

FIGURE 2.6: Schematic of the plasma injection (red), which happens quickly. Dispersive drift due to rotation and magnetic field gradients cause energy dispersion over a longer period of time. After (*Mauk et al.*, 2002).

across the sharp boundary was detected in both hot, planetward plasma and cool, tailward plasma. *Mitchell et al.* (2015) have also suggested that inward flows from reconnection could trigger interchange processes in the inner magnetosphere.

A similar boundary could be present in Jupiter's magnetosphere at the outer edge of the dense, cold plasma torus. The process of outward to inward radial plasma transport could be analagous large scale plasma injections at Saturn, which is evidenced by SKR and auroral UV enhancements (e.g. *Mitchell et al.* (2009); *Lamy et al.* (2013)). However, whilst reconnection (and therefore its inflows in the outer magnetosphere) are expected to occur preferentially on the dawnside (*Vogt et al.*, 2010; *Vogt et al.*, 2014), statistical studies of the inner magnetospheric injections and their auroral signatures show no local time preference (*Mauk et al.*, 1999; *Dumont et al.*, 2014).

Dumont et al. (2015) have shown in simulations that small injections of plasma in the inner magnetosphere are sub-corotating. The localised injection signatures may be generated by electron scattering due to pitch angle diffusion and whistler-mode waves. This corresponds to a sub-corotating source for the second oval feature, so sub-corotation of the feature may be expected.

2.3 Auroral Physics

Processes in the magnetosphere, for example, the generation and transport of hot plasma injections discussed above, can lead to precipitation of plasma along the magnetic field lines on which they are trapped into the ionosphere. This section outlines precipitation processes into the ionosphere and the consequential collisional processes.

2.3.1 Precipitation Processes

There are, broadly speaking, three ways for electrons and ions to precipitate into the ionosphere from the magnetosphere: particles may be scattered into the 'loss cone'; particles may be accelerated along Field-Aligned Currents (FACs); and particles may be accelerated by waves in 'stochastic' acceleration along field lines. These will each be discussed in turn, with the most attention paid to scattering and FACs given the topics of this work. Recent observations from the Juno spacecraft suggest that FACs are less prevalent through the system and that so-called stochastic acceleration processes are more important than previously thought (*Mauk et al.*, 2017b,a; *Allegrini et al.*, 2017).

There are three ways for energy to transfer from the magnetosphere to the planetary atmosphere once electrons impact the ionosphere: excitation, ionisation and dissociation of the neutrals. This results in changes in the ionospheric density and conductance. Jupiter's UV aurora are thus a result of emission from molecular and atomic hydrogen as they relax from excitement by incoming electrons. Hydrocarbons, which absorb parts of the UV emission, are found deep in atmosphere (*Yung et al.*, 1982); their density profile is determined by precipitation variations, upwelling processes that change the number density of hydrocarbons and heating processes (e.g. *Grodent et al.* (2001); *Gustin et al.*

(2004)). In chapter 3 derivations of parameters such as brightness and colour ratio are discussed.

2.3.1.1 Scattering

As discussed in chapter 1 electrically charged particles are fixed onto the magnetic field lines around which they gyrate up and down. A particle will gyrate along a field line until the field strength becomes higher as it reaches a point at high latitude, at which point it is 'magnetically mirrored' back along the field line. The pitch angle of an electron is defined by the angle between its velocity and the direction of the magnetic field line it is on. When the pitch angle becomes too small and falls into the 'loss cone', the electron will be scattered (by collisions) into the ionosphere because its mirror point is too deep. Processes that act to alter the pitch angle of an electron such that it is lost are said to cause 'pitch angle scattering' or 'pitch angle diffusion' (*Roederer*, 2012). Acceleration processes (such as parallel electric fields) also act to 'boost' the loss cone to higher field aligned energies and lower pitch angle.

JADE (Jovian Auroral Distribution Experiment) results from Juno show that at low latitudes (66° to 69°, corresponding to field lines threading the inner plasma sheet) there exist upward loss cones to generate the diffuse aurora (*Allegrini et al.*, 2017). The work of *Li et al.* (2017) have also shown by comparing Juno UVS (Ultraviolet Spectrograph) to JADE and JEDI (Jovian Energetic Particle Detector Instrument) in situ measurements that scattered electrons are largely responsible for the diffuse aurora. Figure 2.7 shows JEDI data of 2.7a intensity versus energy for marked times in 2.7c; 2.7b the energy flux; 2.7c energy distribution and intensity and 2.7d pitch angle. These are shown against time, magnetic latitude and distance from planet. Fig 2.7c marked point (4) corresponds to some broadband scattering causing aurora.

Of particular interest to this thesis, wave-particle interactions in the region 10-17 R_J are thought to scatter electrons into a field-aligned distribution, leading to a transition region at these distances where the electron pitch-angle distribution (PAD) changes, and to a secondary auroral oval sometimes visible at lower latitudes than the main oval (*Grodent et al.*, 2003; *Tomás et al.*, 2004a,b; *Radioti et al.*, 2009). Further study of the second oval, including how hot plasma injections may influence the oval can be found in chapter 4.

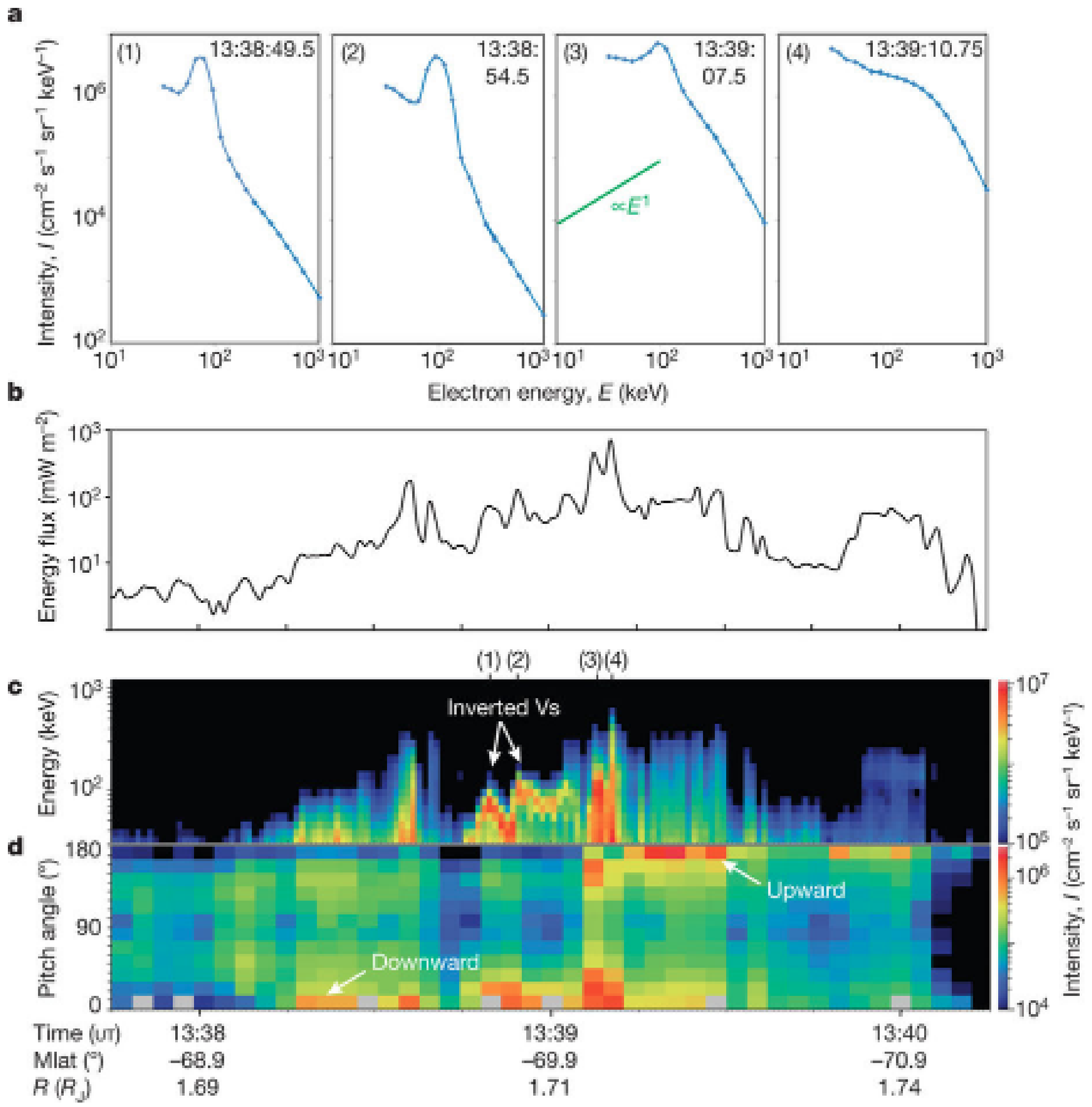

Figure 2.7: JEDI data taken during PJ4 of Juno's orbits. a) Downward intensity I versus electron energy E spectra for the times identified in panel c. b) Integrated downward electron energy flux. c) Intensity versus energy distributions for electrons within 20deg of the downward magnetic field direction. d) Pitch angle distributions of intensities averaged over electron energy (301,000 keV); the labels upward and downward indicate the portions of the plot (top and bottom) that represent electrons moving away from and towards Jupiter respectively. Mlat is the dipole magnetic latitude using the VIP4 field model dipole. R is the distance of Juno from the centre of Jupiter in R_J. Taken from *Mauk et al.* (2017a).

2.3.1.2 Field-Aligned Currents

Field aligned currents (FACs) are the flow of electrically charged energetic particles (either electrons or ions) between the magnetosphere to the ionosphere. The maximum current that can flow from the equatorial plane to the ionosphere is based on the number density and thermal energy of the particles. Without any additional acceleration, current would not impact the ionosphere with enough energy to produce aurora - the particles would experience a resistance to motion as they are magnetically mirrored. The energy flux of the auroral structures seen by HST would be unexplained. However, when a field aligned acceleration is also considered, higher energy fluxes impact the ionosphere. These are described by *Knight* (1973) and are being updated by, for example, *Ray et al.* (2010). Most FACs are thus thought to be accelerated.

The maximal current $j_{\|0}$ that can be carried without acceleration by plasma with number density N and thermal energy W_{th} assuming a full downwards loss cone and an empty upgoing one is:

$$j_{\|0} = eN(\frac{W_{th}}{2\pi m_e})^{\frac{1}{2}} \tag{2.1}$$

The associated field aligned energy flux (the electron energy multiplied by the electron number flux) E_{f0} is:

$$E_{f0} = 2NW_{th}(\frac{W_{th}}{2\pi m_e})^{\frac{1}{2}} \tag{2.2}$$

To produce the larger current $j_{\|i}$ required at the ionosphere, a potential drop with voltage $\Phi_{\|}$ is required:

$$e\Phi_{\|} = W_{th}((\frac{j_{\|i}}{j_{\|i0}}) - 1) \tag{2.3}$$

This results in the field aligned energy flux E_{fi}:

$$E_{fi} = \frac{E_{fi0}}{2}((\frac{j_{\|i}}{j_{\|i0}})^2 + 1) \tag{2.4}$$

The average energy of the electrons can then be expressed as the electron energy flux divided by the number flux and assuming the accelerated energy flux is much greater than that without acceleration:

$$< W > \approx \sqrt{2}W_{th}(\frac{E_f}{E_{f0}})^{\frac{1}{2}} \propto \frac{W_{th}^{\frac{1}{4}}}{N^{\frac{1}{2}}}E_f^{\frac{1}{2}} \tag{2.5}$$

This allows the effect variation of the plasma parameters W_{th} and N to be seen on the mean energy. Colour ratio studies (which describe the mean energy using spectral observation of aurora) can be used to estimate the mean energy (by assuming an atmospheric model). This technique has been used by, for example *Badman et al.* (2016), to try to constrain from auroral images the state of magnetospheric parameters such as mass loading rate or magnetopause distance.

Some in-situ evidence of acceleration along field aligned currents (though much less than required to produce the intense auroras observed by the HST alone) has been reported from recent Juno measurements - 'inverted V' signatures (an electron beam peaked in energy due to acceleration, greater than 50keV) have been detected by JEDI amongst other structures (*Mauk et al.*, 2017a). The 'inverted V' can be seen at marked points (1) and (2) in 2.7c and it is clear that these do not provide the predominant energy flux in Fig 2.7b (compare, e.g. to (3) an angled beam discussed below). Given the suggested relative importance of FACs to other electron flows by Juno, it seems the simple flywheel model of *Cowley and Bunce* (2001) may need developing with regard to current generation; the expectations from Juno in the framework of the model may be tested (*Cowley et al.*, 2017).

Other examples of FACs are found in the magnetotail, connecting plasma 'bubbles' from the magnetosphere to the ionosphere. FACs connect small plasma bubble structures (the inflowing, mass-depleted flux tubes) created during magnetic reconnection to the ionosphere (see Fig. 2.8); the upward FAC gives rise to the 'polar spot' auroral signature (*Radioti et al.*, 2008a). The inflowing plasma carrying the field creates a deflection in B_ϕ such that by Ampère's Law (curl$\mathbf{B} = \mu_0\mathbf{j}$) a current flows into the ionosphere. The deflection in the magnetic field has been observed by Galileo (*Radioti et al.*, 2011).

2.3.1.3 Stochastic Acceleration

This broad category accounts for any other acceleration of energetic particles, for example, by Alfvén waves and broadband acceleration. Juno JEDI results have shown that monotonic energy beams can provide the majority of the current required to produce the auroral intensity observed (*Mauk et al.*, 2017b,a). For example, in 2.7c, the marked point (3) shows an angled beam where there is a clear upward going electron beam that is peaked in energy (2.7a,b). *Allegrini et al.* (2017) have shown using the JADE that

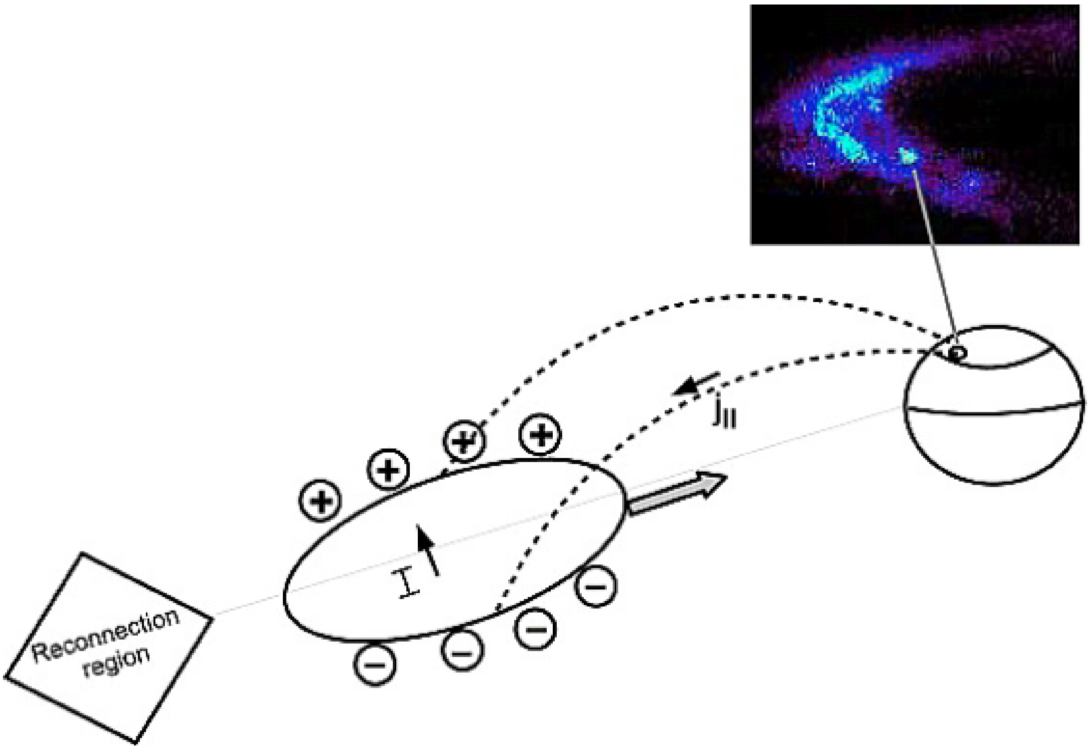

FIGURE 2.8: A plasma bubble in the magnetosphere I, the current integrated over the bubble, linked by the field aligned current $J_{\|}$, dashed, into the ionosphere, where the Ionospheric current flows. The bubble itself flows planetward, as indicated by the grey arrow. The polar spot is formed on the 'up' FAC from the dawnside of the bubble. After *Radioti et al.* (2010) and *Nakamura et al.* (2001).

there are mostly up and but some downwards electron beams. Alfvénic acceleration, acceleration of particles by Alfvén waves, is thought to generate the moon footprint auroral signatures (see review by *Bonfond* (2012) and references therein).

The Alfvén speed, the fastest wave propagation along a magnetic field line, is defined as:

$$V_A = \frac{B}{\sqrt{2}\sqrt{\mu_0 n_i m_i}} \tag{2.6}$$

where B is the magnetic field strength, μ_0 is the magnetic constant, n_i is the ion number density and m_i is the ion mass. This provides a theoretical 'limit' on speed of information propagation along the field lines; comparison between the Alfvén speed and observation can therefore help rule out whether single field lines are responsible for a phenomenon.

Sketch of the typical FUV auroral components of the northern hemisphere of Jupiter. Planetocentric parallels and System III meridians are drawn every 10°: 1. Main emission (oval); 2. Kink region; 3. Discontinuity; 4. Secondary emission; 5. Signatures of injections; 6. Io footprint (multiple) and tail; 7. Europa footprint and tail; 8. Ganymede footprint (multiple); 9. Polar active region; 10. Polar dark region; 11. Polar swirl region; 12. Polar auroral filament (PAF); 13. Dawn spots and arcs; 14. Midnight spot. The *upper gray shaded region* is not accessible to Earth orbit instruments

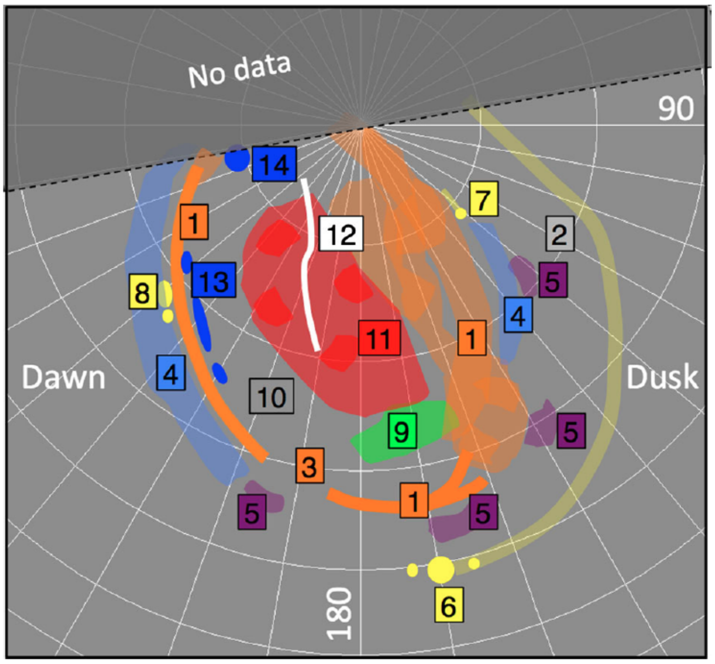

FIGURE 2.9: A schematic showing the most frequent UV auroral signatures as revealed by HST. The schematic is oriented with 180° system III longitude to the bottom. Taken from *Grodent* (2015).

2.4 Auroral Signatures

Precipitation along the magnetic field lines from the magnetosphere into the ionosphere, where collisional processes that generate the aurora, as described above. The auroral morphologies and intensities therefore provide a way of measuring magnetospheric processes. In this section, the ultraviolet (UV) and radio emissions are both discussed.

2.4.1 Ultraviolet Signatures

UV observations taken with the HST have provided a wealth of information about the aurora. *Grodent* (2015) reviews the UV aurora as revealed by HST and schematically shows, as in Fig. 2.9, the common auroral features, some of which are more thoroughly introduced below and further investigated in this thesis. Typically, the aurora have been split into three groups based on their latitudes; the high latitude ‘polar emission’, the mid-latitude band of ‘main emission’ and the lower latitude ‘outer emission’. This section examines the most prominent auroral signatures and relates them to their magnetospheric drivers, working from the outer emissions at lower latitude to the high latitude aurora.

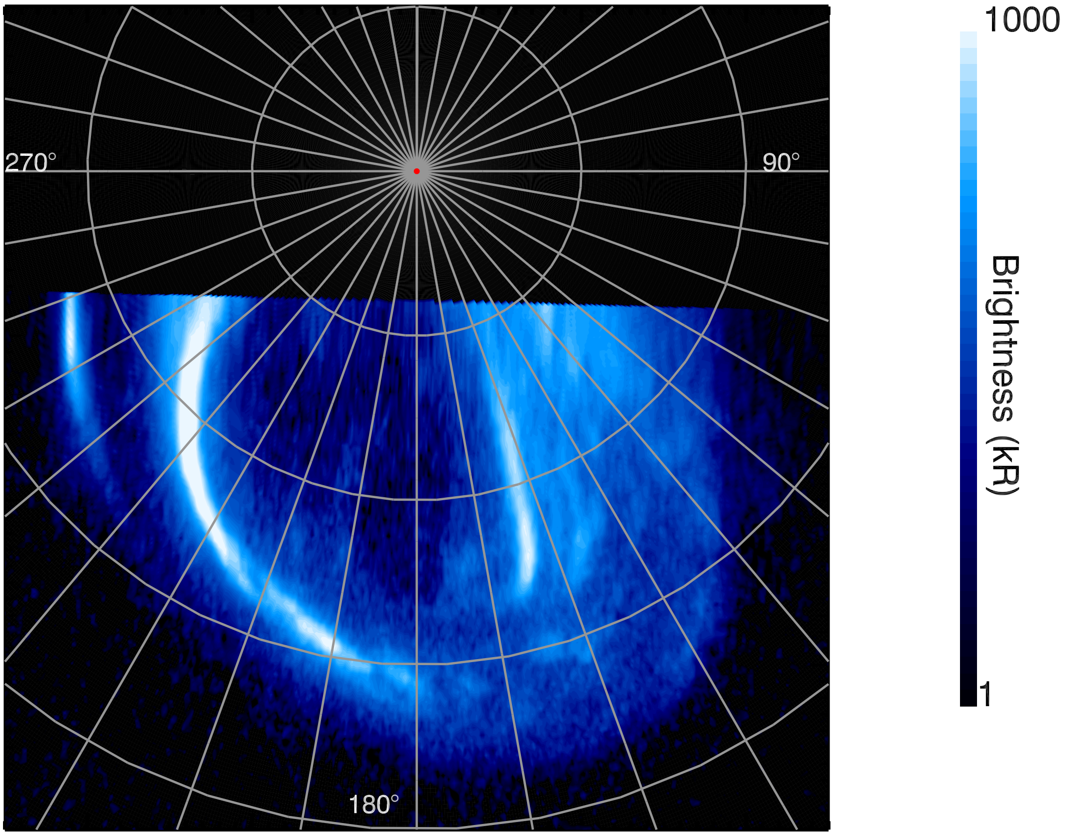

Figure 2.10: A polar-projected HST image of Jupiter's northern FUV aurora taken at around 180° CML. The image is displayed with a log intensity scale saturated at 1000 kR. The grey lines indicate a 10° × 10° jovicentric latitude-system III longitude grid. The image is oriented such that 180° λ_{III} is directed toward the bottom and λ_{III} labels are displayed in grey.

Figure 2.10 shows an auroral image from the 2007 HST campaign. Images are projected on a 10° × 10° jovicentric latitude-system III (rotating with the planet's auroral region at a period of around 10 hours) longitude grid. This image has a nearly empty high latitude region, well defined main emission (aside from where the main emission is discontinuous) and very little low-latitude activity. The main emission in this image is slightly contracted compared to the campaign average.

2.4.1.1 Outer Emission

Injection signatures (see 5 on Fig. 2.9) can be the largest and brightest component of the outer emission. Their size can vary from a few degree size blobs to large more diffuse emissions. The injection features can be driven either by scattering of electrons into the loss cone or field-aligned currents associated with pressure gradients within, and at the boundaries of, the hot plasma. They have been related to hot plasma injections in the inner magnetosphere (*Mauk et al.*, 2002; *Bonfond et al.*, 2012; *Dumont et al.*, 2014). *Kimura et al.* (2015) has related injection signatures to radial transport motions as a result of interchange as hot plasma moves radially toward the planet from reconnection.

Injection features were identified in observations from 2007 during an interval of high volcanism on Io (*Nichols et al.*, 2009a; *Bonfond et al.*, 2012). These injections were attributed to increased Iogenic outflow during a volcanically active time, driving interchange and therefore hot plasma injections. In particular, *Bonfond et al.* (2012) showed an increase in the occurrence rate of high power equatorward emission following increased Io activity compared to a prior period. Before the volcanically active period only 1 in 41 days showed high power emission, whereas after the activity the rate was 8 in 32 days. This shows injections can also be used as an indicator of increased mass outflow from Io - this has been further demonstrated in the 'Juno era' observations of *Nichols et al.* (2017a).

At longitudes less than 150°, the Equatorward Diffuse Emission (EDE) region reported in *Radioti et al.* (2009) is prominent. The EDE region appears broad in latitude and has a low brightness. The second oval feature (see 4 on Fig. 2.9) lies outside of the main emission and tends to be less bright than the injection signatures, appearing in sections of discrete arcs of varying length (*Tomás et al.*, 2004a,b; *Grodent et al.*, 2003). These features both magnetically map to the PAD region and are thought to be the results of scattered electrons excited by whistler mode waves (*Woodfield et al.*, 2013; *Katoh et al.*, 2011), which exist in this magntospheric region (*Menietti et al.*, 2016). Chapter 4 investigates whether the second oval feature can be re-energised by precipitation due to hot plasma injections in the inner magnetosphere region.

2.4.1.2 Main Emission

The main emission (see 1 on Fig. 2.9) at Jupiter has been traditionally viewed as the most stable component of the aurora, e.g. *Clarke et al.* (2004); *Grodent et al.* (2003) and references therein. The current understanding of how the main emission is generated can be found in the 'field-aligned currents' section of chapter 1; its brightness, typically ∼400 kR (*Radioti et al.*, 2008b), will vary mostly with mass outflow rate, ionospheric conductivity and electron temperature. Increases in electron precipitation can increase the ionospheric conductivity (*Nichols and Cowley*, 2004). Models have shown this can increase the coupling currents, generating bright and broadened aurora (*Nichols and Cowley*, 2003). *Badman et al.* (2016) reported the main emission expanded 1° and dimmed by 70% of its power - this is thought to be in response to changes in cold plasma transport rate or expansion of the magnetosphere. The main emission shape is often referred to as a 'kidney bean' due to the 'kink sector' at longitudes 80°-150° (see 2 on Fig. 2.9) (*Grodent et al.*, 2003, 2008a). There are temporal variations within the main emission observable using the ∼45 minute cadence of HST images - these shall be discussed in turn.

Given the main emission is related to the magnetosphere-ionosphere coupling it may be expected that there are variations in the emission with magnetic local time. *Radioti et al.* (2008b) reported the discontinuity region in the main emission around local noon with varying extent. They suggested solar wind driven compresion of plasma means a reduction or a reversal in the FACs required to transfer momentum from the planet to enforce co-rotation, so the main emission mapping to this magnetic local time sector would be dimmer. In addition, *Palmaerts et al.* (2014) suggested that a small transient spot, also fixed in magnetic local time at around 1400 LT, was generated by flow shear induced by intermittent inward plasma flow near noon in the equatorial plane. Periodic emission has also been seen in the main emission. *Nichols et al.* (2017b) showed that a feature in this region could be periodically pulsing with a period of 10 minutes as a result of ULF wave generation at a low density region outside the plasma sheet. The authors suggest this could be related to the processes described by *Palmaerts et al.* (2014).

The dawn sector of the main emission can display incredibly bright and varied morphology. 'Multiple Dawn Arcs' - parallel arcs poleward of main emission - have been reported (*Grodent et al.*, 2003). They have been linked to outer magnetospheric processes (i.e. reconnection). 'Dawn storm' events, described by *Gustin et al.* (2006) and *Nichols et al.* (2009a), are a morphology in which the entire dawn length of the main emission is brightened and broadened. The brightness of the 'dawn storm' morphologies has been reported to peak at 1.8 MR (*Gustin et al.*, 2006), in this thesis we report >6.8 MR, and in recent observations from *Nichols et al.* (2017a), the power has been seen to peak at 5.5 TW from this feature. The precise origin of the dawn storm feature is still unclear but based on magnetospheric mapping it is probably related to transport through the middle magnetosphere (*Kimura et al.*, 2015). The reader is directed to chapter 3 for further discussion. In the most recent and brightest case, the feature is attributed to transport of both hot plasma inflows from the tail and increased Iogenic outflow (*Nichols et al.*, 2017a).

2.4.1.3 Polar Emission

The polar emission is the most varied of all the auroral emissions. The features have been related to nightside processes such as magnetospheric reconnection, specifically the aforementioned polar spots. These tend to be around 1° of latitude poleward of the main emission (see 13 and 14 on Fig. 2.9) (*Grodent et al.*, 2004; *Radioti et al.*, 2008a, 2010). Another feature are quasi-periodic flashes in the dusk/night sector (*Nichols et al.*, 2017a). The cap also shows dayside processes such as emission driven at the open-closed field line boundary (*Bonfond et al.*, 2017a; *Vogt et al.*, 2011) and specifically bursts, from the dayside cusp (*Waite et al.*, 2001; *Pallier and Prangé*, 2001, 2004; *Bunce et al.*, 2004; *Bonfond et al.*, 2011).The bursts are can be periodic, showing periodicities most notably of 40-45 and 2-3 minutes. These periodicites have been linked to travel times along field lines (*Bunce et al.*, 2004), radio bursts (*Kimura et al.*, 2011) measurements and Ulysses measurements (*McKibben et al.*, 1993).

Given the dependence on many magnetospheric phenomena, the polar aurora exhibit many different regions of morphologies and are often split up on this basis. Traditionally, the aptly named ‘swirl region’, ‘active region’ and ‘dark region’ have all been considered (*Grodent et al.*, 2008b) (see 11, 9, 10 respectively on Fig. 2.9). Other subsections (such as a 'Noon Auroral Region') have also been considered, e.g.*Nichols et al.* (2009a); *Nichols et al.* (2017a).

2.4.1.4 Moon Footprints

The most equatorward auroral features tend to be the moon footprints; Io, Europa and Ganymede have moon footprint ‘tails’ (see 6, 7 and 8 on Fig.2.9) (*Bonfond*, 2012; *Bonfond et al.*, 2017b). Io and Ganymede are known to have multiple spots in the tail structure (*Bonfond et al.*, 2008, 2009; *Bonfond*, 2010; *Bonfond et al.*, 2013). Because of their known radial position in the magnetosphere, the footprints are used to validate mapping along magnetic field lines between magnetospheric source regions and the ionospheric auroral signatures. The auroral signatures are driven by plasma waves such as Alfvén waves (e.g. *Bonfond et al.* (2012) and references therein). The moons are an obstacle to the plasma flow in the magnetosphere, which flows faster than the orbital speed of the moon. This launches Alfvén waves along the magnetic field line which accelerates electrons and causes auroral precipitation. The spots often appears downstream of the moon such that there is a ‘lead angle’ between the main moon auroral spot footprint and the moon itself, due to the delay as the complex interaction takes place. For example, for

Io, interactions of the waves through the IPT causes multiple auroral spots to appear. Analysis of the footprint properties therefore allows investigation of the properties of the plasma environment of the moon footprint field lines.

2.4.2 Radio Emission

The Radio emissions are a lower frequency band emission than the UV. The process that drives the UV emission can also drive Radio emissions (*Zarka*, 1998) and recent results from Juno show radio emission at Jupiter is driven by the Cyclotron Maser Instability (*Louarn et al.*, 2017; *Kurth et al.*, 2017). The emissions of particular relevance to this thesis are the narrowband kilometric (n-KOM), decametric (DAM) and hectometric (HOM) emissions. The HOM (0.5 - few MHz) and DAM (MHz) emissions have been correlated with the solar wind activity (*Galopeau and Boudjada*, 2005; *Hess et al.*, 2012, 2014). The HOM emissions are analogous to the terrestrial Auroral Kilometric Radiation (AKR) and Saturn Kilometric Radiation (SKR). DAM emissions have also been related to Io, so fall into two categories - Io and non-Io DAM. The non-Io DAM emissions are a higher frequency extension of the HOM emission (*Zarka*, 1998).

n-KOM (40-150 kHz) emissions have been related to internally driven magnetospheric dynamics (*Louarn et al.*, 2000, 2001; *Louarn et al.*, 2016). *Louarn et al.* (2014) showed that inflows from tail reconnection were correlated (within one planetary rotation, ∼10 h) with intensifications of the HOM and the subsequent appearance of new n-KOM radiation sources in the outer Io plasma torus, so are possibly related interchange motions (*Louarn et al.*, 2016).

Intensifications of non-Io DAM have been correlated with the arrival of solar wind shocks in some cases, although the physical process leading to the intensification has not been described (*Hess et al.*, 2014). There are also 'internally triggered' non-Io DAM emission (*Hess et al.*, 2012, 2014). It is possible to identify whether DAM emissions have a dawn or dusk source from their frequency spectra; vertex-early (late) correspond to dawn (dusk) sources. Increases in HOM emission has also been related to high solar wind dynamic pressure (*Gurnett et al.*, 2002). Solar type III emissions tend to have a distinctive increasing frequency in time pattern; this make it possible to pick them out and isolate HOM emissions using satellited in interplanetary space. Figure 2.11 shows an example of radio data detected with the WIND Waves instrument (*Yoneda et al.*, 2013) and identifies the emissions. More detail on radio emissions and their detection can be found in chapter 3.

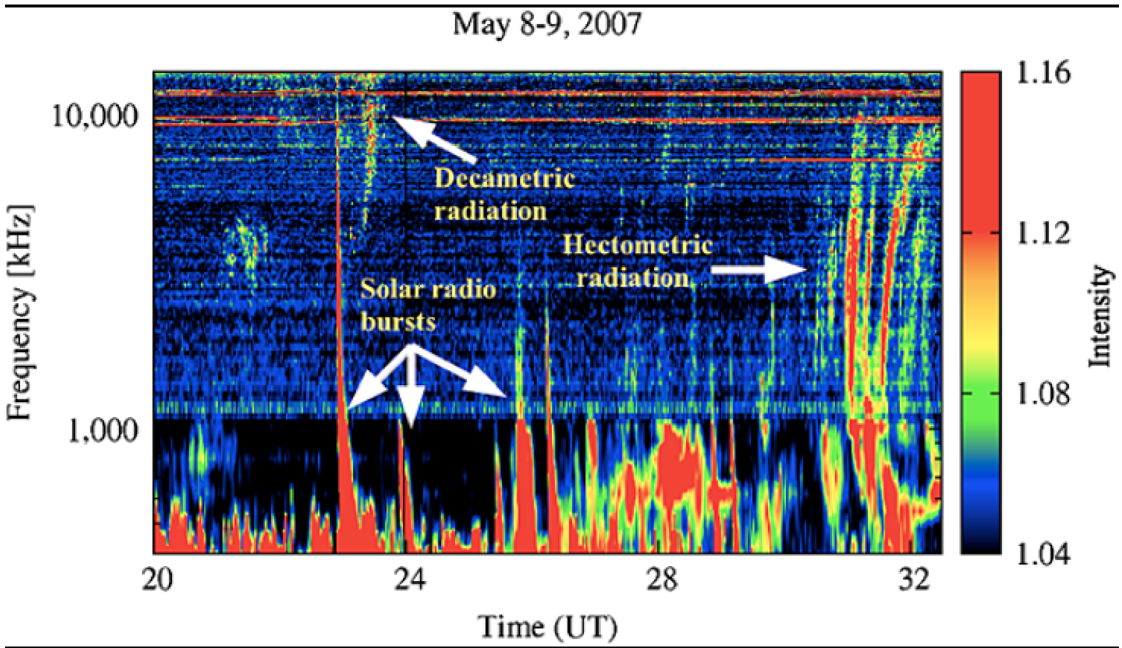

FIGURE 2.11: Example radio data from WIND waves in 2007 showing detection of Jovian radio decametric (DAM), hectometric (HOM) and solar bursts. The DAM emission is vertex late so corresponds to a dusk source. Taken from *Yoneda et al.* (2015).

This chapter has introduced the structures in Jupiter's magnetosphere, its field configuration, some of the processes (injections and interchange) that are of importance, auroral process physics, some of the typical UV auroral features and radio emissions. Many of these areas are particular to, or particularly prominent in, Jupiter's magnetosphere. Whilst comparing magnetospheric processes between planets is often insightful, for the areas described above due care must be taken to understand the physics in Jupiter's context.

Chapter 3

Instrumentation and Data Reduction

This chapter outlines the relevant instrumentation of the Hubble Space Telescope's Space Telescope Imaging Spectrograph (STIS) camera. It also outlines the use of the Waves instrument on the WIND satellite for Jovian radio wave detection. It then goes on to discuss the data reduction processes to produce the polar-projected images used for analysis. The derivation of the data products brightness, power and colour ratio are also presented.

3.1 Hubble Space Telescope Instrumentation

The Hubble Space Telescope has made many contributions to science. It orbits Earth at around 600 km. The 2.4 meter telescope therefore avoids distortion from atmospheric effects resulting in higher resolution images than ground based telescopes.

The majority of data used in this thesis are taken using the Hubble Space Telescope's Space Telescope Imaging Spectrograph (STIS) instrument; its specification and a detailed discussion of its optics can be found in *Woodgate et al.* (1998). Figure 3.1 shows a simplified schematic of the optics of STIS.

The light enters the camera, hits the primary mirror, is corrected for the primary mirror abberation by two correction mirrors and then passes through a slit appropriate for the field of view. The beam is then collimated before hitting the mode select mechanism.

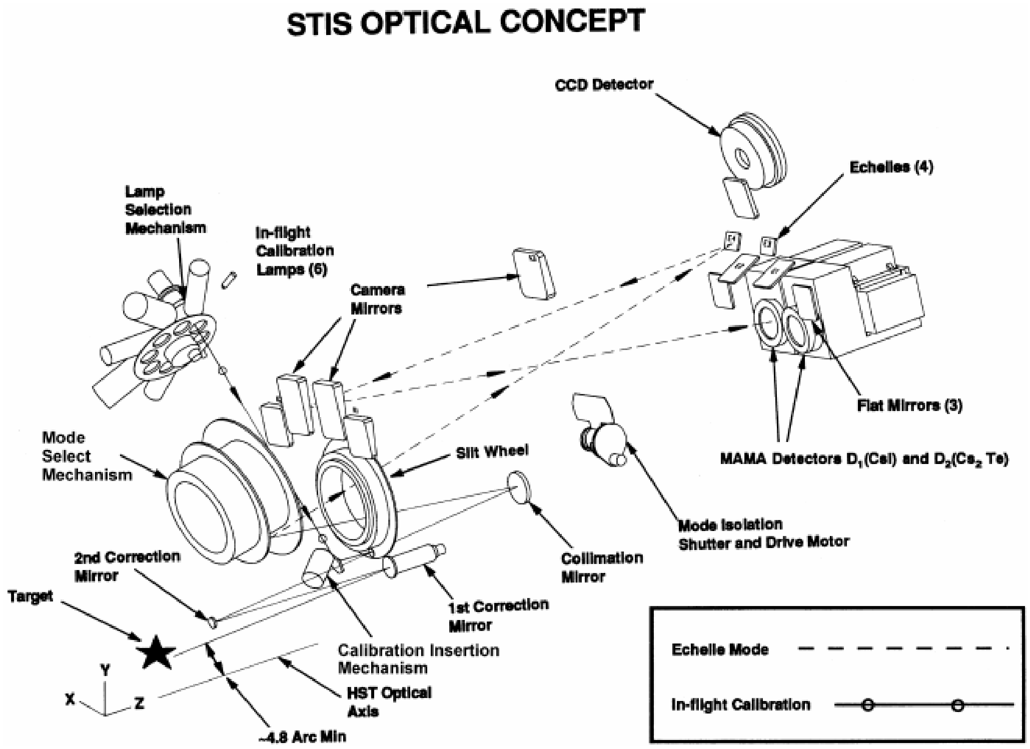

FIGURE 3.1: A simplified schematic of the optics on the STIS after *Woodgate et al.* (1998)

Here, in the spectral mode, the gratings are selected before the beam is directed to the Multianode Microchannel Array (MAMA) detectors, or in imaging mode sent to the appropriate Charge Couples Device (CCD). The MAMA detector has an array size of 1024 by 1024 pixels; each pixel is 0.0243" (where 1" is 1 arcsecond, corresponding to 1/3600°). The point spread function (the spread due to diffraction) is 0.08" full width at half maximum. The detector photoamplifies the signal and is able to either integrate an image across the array over time or record the time and position of each signal in its 'time-tag' mode (*Woodgate et al.*, 1998).

The MAMA camera is solar blind and can sense the far ultraviolet emission from Jupiter. A SrF_2 filter is used to block out some emission lines. The UV emission mainly consist of H Lyman alpha and H_2 Lyman and Werner bands. The bandpass of the SrF_2 filter is 1250 - 1900 Å, i.e. it rejects light at shorter wavelengths including the H Lyman alpha line at 1215 Å(which can be excited by solar rays both at Jupiter and Earth). Each $\sim$45-minute long visit consists of two sequences of 700 s time tag imaging sequences interrupted by a 200 s spectral observation.

HST is an Earth-orbiting telescope, so its view of Jupiter is constrained to a specific geometry. The Central Meridian Longitude (CML) is the longitude subtended by the Earth observer to the planet measured in planetary rotation frame (System III longitude). The Sub-Solar Longitude (SSL). Earth is close to the Sun relative to Jupiter, so CML and SSL will always be very similar. If a feature is fixed in longitude then it rotates with the planet. If the feature is fixed in local time it won't rotate with the planet.

3.1.1 Spectral Imaging

In this thesis, spatially resolved spectral observations used were taken consecutively with the HST images, in the wavelength range 1100-1700 Å. The colour ratio is the ratio of H_2 emission intensity at 1550-1620 Å, which is unabsorbed by methane (the major hydrocarbon component), compared to 1230-1300 Å, absorbed by methane. The slit position was verified against intensity profile along the slit from the spatially resolved images taken before and after and also against the limb position. The full wavelength range was integrated over (to account for the limited throughput of the spectral filter) to compare to the intensity profiles of the images.

3.1.2 Waves on WIND

Boudjada et al. (2001) have shown it is possible detect Jovian hectometric emission (HOM) using the Radio and Plasma Waves (WAVES) experiment on the Wind spacecraft. Wind/WAVES data are available through CDAWeb. The spacecraft is located at the L1 Lagrange point in orbit around Earth and detects from around 1-14000 kHz over its two receivers RAD 1 (4-1040 KHz) and RAD 2 (1075 to 13825 kHz) (*Bougeret et al.*, 1995), which are co-incident with HOM emission frequencies (500 - few 1000 kHz). The data can be used when HOM bursts can detected above solar contamination (see below) and when there is appropriate alignment; when Jupiter can be seen by the spacecraft (i.e. both the planet and the spacecraft are the same side of the Sun). WAVES can also pick up DAM emission (few thousand kHz), which generally appears up to higher frequencies than the solar contamination, so is slightly easier to pick out, especially when considering the DAM emission spectra characteristic forms.

Examination of typical WAVES data at solar minimum and maximum shows that intense solar Type III radio bursts (considered contamination when detecting HOM) occur more during solar maximum. These bursts extend over the full frequency range and have a characteristic shape in frequency-time space, wherein the frequency decreases with time. This is different to the HOM and DAM emission characteristics (e.g. intensity and arc shape, see chapter 1).

Studies taken during solar maximum will use data that are heavily contaminated by solar bursts, but it is possible to pick out other radio emission structures using both the spectra and analysis of the intensity as a function of Jupiter CML, [e.g., *Yoneda et al.* (2013)]. The occurrence probability of HOM is known to peak at CML around 30°, 120° and 270° (*Galopeau and Boudjada*, 2005); it is therefore possible to see whether any significant HOM can be statistically picked out over noise and use WAVES data during times of contamination.

3.2 Data Reduction

This section discusses how images taken by the cameras on HST are processed into the polar-projected views used for analysis. It also discusses how the brightness, power and colour ratio parameters are derived.

3.2.1 Image Processing Pipeline

The images were processed through the Boston University pipeline (*Nichols et al.*, 2009a; *Clarke et al.*, 2009), correcting for dark current, flat field, and geometric distortion. The images were projected onto a planetocentric longitude-latitude grid assuming a peak auroral emission height of 240 km above the 1 bar pressure level of an oblate spheroid (*Vasavada et al.*, 1999). The resolution of the projected image is 0.25 °× 0.25 °. The images are clipped at ∼2° below the planetary limb to avoid analysis where there are significant inaccuracies due to the oblique viewpoint (*Grodent et al.*, 2003). Further details about data reduction and projection accuracy can be found in *Nichols et al.* (2009a) and *Grodent et al.* (2003) respectively.

Auroral features are measured in system III (λ_{III}), a jovicentric longitude-latitude grid which corotates with the planet with a period of 9.925 hours, as defined in *Dessler* (1983). In this way, features that move to higher longitudes (clockwise) are sub-corotating, and features that move to lower longitudes (anti-clockwise) are super-rotating.

3.2.2 Deriving Data Products From Images

The 'data products' brightness, power and colour ratio have been shown to vary for different features of the aurora (e.g. *Nichols et al.* (2009a); *Gérard et al.* (2014)). By comparing these, the energies and fluxes of precipitating electrons can be estimated and compared to plasma theory (such as the Knight relation (*Knight*, 1973)), which will reveal more about the magnetospheric source of the plasma e.g. the plasma temperature and thermal energy, electron density etc., as described in chapter 2.

3.2.2.1 Colour Ratio

Jupiter's UV aurora are a result of emission from molecular and atomic hydrogen as they relax from excitement by incoming electrons. Hydrocarbons, which absorb parts of the UV emission, are found deep in atmosphere (*Yung et al.*, 1982); their density profile is determined by precipitation variations, upwelling processes that change the number density of hydrocarbons and heating processes (e.g. *Grodent et al.* (2001); *Gustin et al.* (2004)). By taking the ratio of the emission intensity of the bands absorbed and unabsorbed by hydrocarbons, a measure of the effective hydrocarbon column density is found. This is known as the colour ratio (*Tao et al.*, 2016a). Electrons that penetrate the atmosphere will be stopped by the collisional process that lead to auroral emission. Electrons that have a higher energy may be expected to penetrate deeper; therefore the colour ratio can be used to estimate the electron energy, among other parameters, when an atmospheric model is applied. These atmospheric models clearly have an effect on the derived parameters (*Gérard et al.*, 2014). The colour ratio is 1.1 if there is no absorption by hydrocarbons; as more emission is absorbed (i.e. deeper penetrating and higher energy electrons) the colour ratio rises. The colour ratio therefore provides a measure of the precipitating electron energy. The colour ratio has been shown to vary between different auroral features *Gustin et al.* (2004); *Gérard et al.* (2014) and between different longitudes of the same feature (*Gustin et al.*, 2006), and so can act as another diagnostic tool for investigating the precipitating electron characteristics and therefore the magnetospheric driver of precipitation. Recent application of the technique to JUNO era images has shown that the colour ratio peak and peak brightness are often not co-located. This has been shown for the case of auroral injection signatures, demonstrating a differential drift in energy and that the signature is formed by hot plasma injections as thought (*Bonfond et al.*, 2017a). It has also been shown that in the swirl region of the polar cap a higher colour ratio is seen compared to the brightness, which has implication for the outer field lines and the magnetopause processes associated to this region (*Gustin et al.*, 2004; *Bonfond et al.*, 2017a).

3.2.2.2 Electron Flux, Brightness and Power

Comparison of the power emitted by different regions of the aurora over time can be used to indicate how energy is moved through the magnetosphere. The power emitted can be extracted from the images in the following procedure, which is detailed more thoroughly in *Gustin et al.* (2012): counts per second are converted to kiloRayleighs (kR) emitted from H_2 over the full wavelength range 700-1800 Å, assuming a colour ratio of 2.5 (*Gustin et al.*, 2012). The emission falling on the SrF_2 filter corresponding to 1kR is 4523 counts per second. (1 Rayleigh corresponds to 10^6 photons crossing an area of 1 cm^2 in every direction each second.)

Electron flux is determined from the auroral brightness using the approximation that 10 kR$\sim$1 mWm^{-2} of input electron flux. For full details, see *Tao et al.* (2016a) and *Gustin et al.* (2004).

The brightness (in kR) observed by one pixel of the detector is multiplied by 1 x 10^9 to recompute the number of incident photons in counts per second. To then find the energy flux, this is multiplied by the mean energy of an auroral photon in 700-1800 Å(the full UV spectrum). The absorption by the atmosphere is known from a model of the atmosphere (indicated by the colour ratio) and the camera filter rejects certain wavelengths. These two factors are encapsulated in a 'conversion factor'. For STIS, this results in a conversion factor of 1.02 x 10^{-9} for a colour ratio of 2.5 (*Gustin et al.*, 2012). This is then multiplied by the Jupiter-HST distance squared. Alternate conversion factors for the counts per second to brightness and brightness to power for the Advanced Camera for Surveys (ACS) can be found in *Gustin et al.* (2012). The power is calculated from the brightness on the unprojected image, since as part of the projection process, brightness is conserved, but area is not.

The observed auroral power is dependent on the CML. For some viewing geometries, a significant fraction of the auroral emission is located behind the planetary limb because of the magnetic dipole tilt of 10°. Following the procedure outlined in *Clarke et al.* (1980) and more recently *Nichols et al.* (2009a) and *Bonfond et al.* (2012), the corrected UV power in each area of interest of the aurora was extracted from the HST images in the following way: Different views of the Jovian northern hemisphere from Earth were simulated and the fraction of area of interest visible from Earth at each CML compared the to the total region visible was found. This produces a curve of CML versus fraction of area of interest visible. This curve was fitted using an RMS minimization technique to the raw power values for each visit; the peak of the curve is the ‘auroral index’. This is a measure of the activity separate from the viewing effects; it is what the power would be if the points were viewed at the optimal viewing angle. The deviation (positive or negative) of the raw power values from the curve was added to the ‘auroral index’ to give the corrected power, hence taking into account their viewing geometry and auroral activity respectively. This method assumes that there is no significant variation of powers in a single visit and is therefore not appropriate for analysis of power variation within one visit.

Chapter 4

Auroral Evidence of Radial Plasma Transport

4.1 Introduction

As chapter 1 outlines, as part of the Vasiiliunas cycle, Iogenic plasma generated in the inner magnetosphere is transported radially outward through a quasi-steady state process to the outer magnetosphere where it is lost down the magnetotail. In this chapter, evidence of plasma transport from outer to inner magnetosphere is presented.

The HST images of Jupiter's FUV northern aurora are taken between days of year 001 to 016 of 2014 (ID: GO13035, available through the Space Telescope Science Institute (STScI) website). The 2014 Hubble Space Telescope (HST) campaign has been studied previously. We take into account the relevant work in our study. *Kimura et al.* (2015) have suggested that transient brightening events during the observational interval are driven by internal processes, not externally by the solar wind. *Yoneda et al.* (2015) have shown that there was no increase in sodium nebula brightness, indicating that Io was not significantly volcanically active in the weeks before the campaign. S and O emissions in the inner Io torus are observed to be steady over the observation interval (*Tsuchiya et al.*, 2015). It is therefore unlikely that the transient brightening is due to increased Iogenic outflow. This study further investigates the brightening event on day 011.

There is on average one HST 'visit' per day, with exceptions of day 011 and day 013 having two and three visits respectively. Each ∼45-minute long visit consists of two sequences of 700 s time tag imaging sequences interrupted by a 200 s spectral observation.

The imaging observations are split into seven images with 100 s exposures. The images have been processed and projected as described in chapter 2.

In this chapter, we present auroral observations of a super-rotating polar spot transition from the polar to main emission region in the presence of a broad, bright main emission feature and two large equatorward emission features. The magnetospheric processes that cause these aurora occur at different radial distances. We therefore investigate the signatures as part of a sequence of inward radial transport processes.

4.2 Results

4.2.1 Auroral Features

Figure 4.1 shows six 100 s exposure images taken on 11 Jan 2014. The field of view is bounded by the dashed white line. In this work, the main emission boundary (shown in panel f) is defined as a strip that is 1° poleward and 2° equatorward of the average peak in the main emission for the 2014 HST campaign. Given the variable main emission morphology through the campaign, the strip sometimes cuts off the extreme edges of the emission. The polar region is defined as poleward of the main emission and the equatorward region is equatorward of the main emission, up to ∼1.5° poleward of the Io Footprint (*Hess et al.*, 2011).

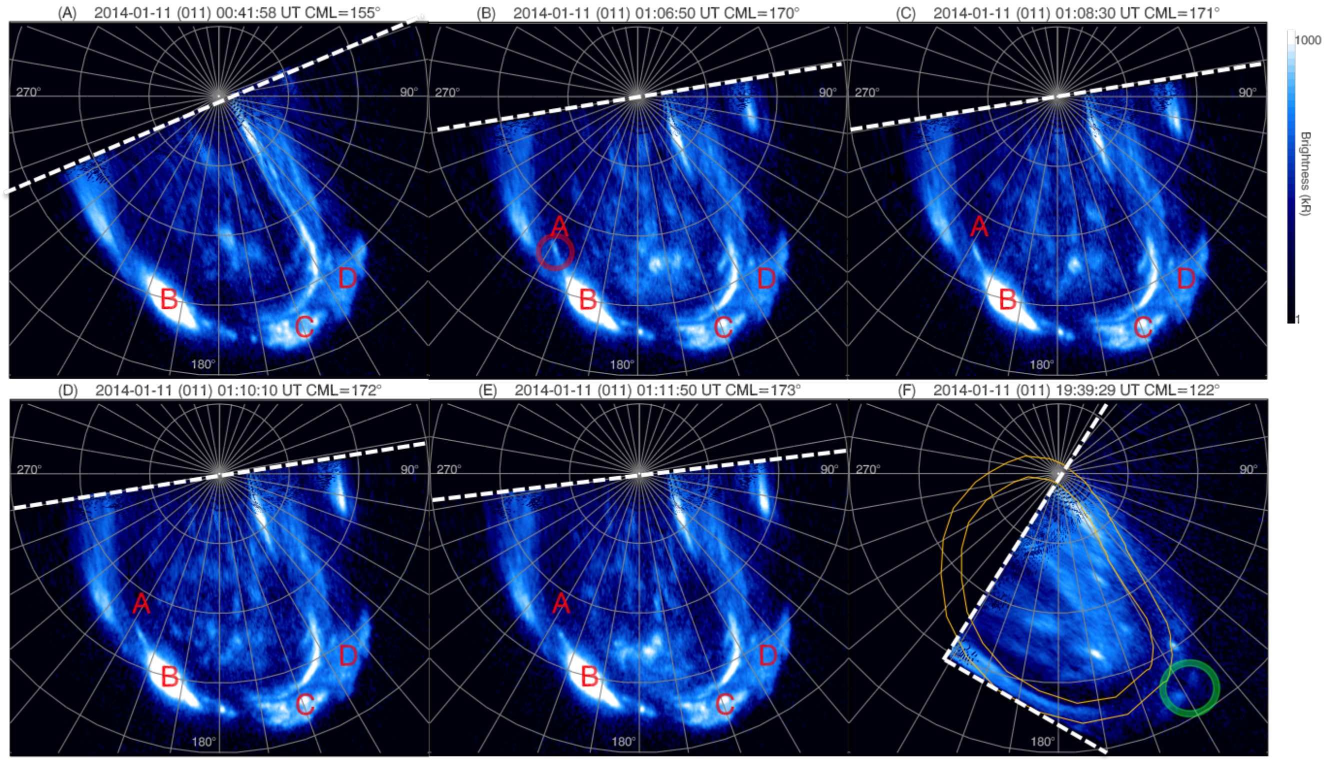

FIGURE 4.1: Six panels showing polar-projected HST image of Jupiter's northern FUV aurora on 11 Jan 2014 at a) 00:41 UT, b) 01:06 UT, c) 01:08 UT, d) 01:10 UT, e) 01:11 UT and f) 19:39 UT. For each image the exposure time was 100 s. The Central Meridian Longitude (CML) is shown. The image is displayed with a log intensity scale saturated at 1000 kR. The dashed white line shows the edge of the field of view. The grey lines indicate a 10° × 10° jovicentric latitude-system III longitude grid. The image is oriented such that 180° λ_{III} is directed toward the bottom and λ_{III} labels are displayed in grey. On panels a-e, labels indicate the super-rotating polar spot (A), circled on panel b, a bright and expanded main emission region (B) and two equatorward emissions (C and D). The yellow lines on panel f, taken ~18 h after the first visit, show the boundaries of the main emission region, derived from the average main emission position over the 2014 campaign. The poleward region of the main emission strip is the 'polar region' and the equatorward region up to 1.5 ° poleward of the Io footprint is the 'equatorward' region. Equatorward emissions circled in green on this image are possible remnants of the equatorward features C and D.

In the first sequence of the first visit (00:31 - 00:41 UT, Fig 4.1a), three features are highlighted; feature B is a section of the main emission and C and D are both large equatorward emission features. In the second sequence of the first visit (01:01-01:11 UT, Fig 4.1b-e), feature A is a polar spot. This is circled in panel 4.1b. The images, which are shown fixed in SIII longitude with λ_{III}=180 ° at the bottom, indicate that the polar spot is super-rotating, i.e. moving faster than the features that are fixed in λ_{III}.

The spot centre (the brightest central point of the 200 kR contour) moves ~8° (~8000 km) in the ionosphere over the 10 minute sequence, corresponding to ~270% corotation speed (including both azimuthal and radial motion, where 100% corresponds to corotation). The spot is up to 4° wide in longitude and 1° in latitude and brightens to an average of ~300 kR. It is separated from the campaign average main emission position initially by 3.8° and moves equatorward to a separation of 2° latitude over the 10 minute sequence. The spot is an extended feature and extends between 200°-211° longitude over all images. The spot appears on the dawn flank, similar to those reported in (*Radioti et al.*, 2008a, 2010), which were interpreted as a signature of reconnection in the magnetotail.

The main emission is usually broad at dusk and well defined/narrow at dawn (*Gustin et al.*, 2006). However, in this visit (00:33-01:11 UT), in the region λ_{III} ~185-200° the main emission appears notably expanded in latitude (up to ~2.5° latitude either side of the average campaign main emission position) compared to the rest of the campaign and previous observations. This unusual feature could be due to a structure superposed on the main emission, or an expansion of the emission itself. Figure 4.2 shows the substructure of feature B at 00:41 UT. The substructure consists of two extremely bright regions (up to >6.8 MR) which appear to subcorotate over the sequence. The broadness of the feature is obvious when compared to the main emission on the opposite side of the oval, between λ_{III} ~150-160°. The main emission region at B is also very bright; the power in the total main emission region in these images is consistently over 1000 GW, compared to typical power of ~500 GW over the rest of the 2014 campaign.

The observed morphology is reminiscent of but distinct from the ‘dawn storm’ events described in chapter 1. In feature B described here, the peak brightness of the main emission feature B is much higher than a typical dawn storm at >6.8 MR and the broadened region is well constrained, not covering the whole dawn flank of the main emission. Feature B is also distinct from the multiple dawn arcs reported by *Grodent et al.* (2003).

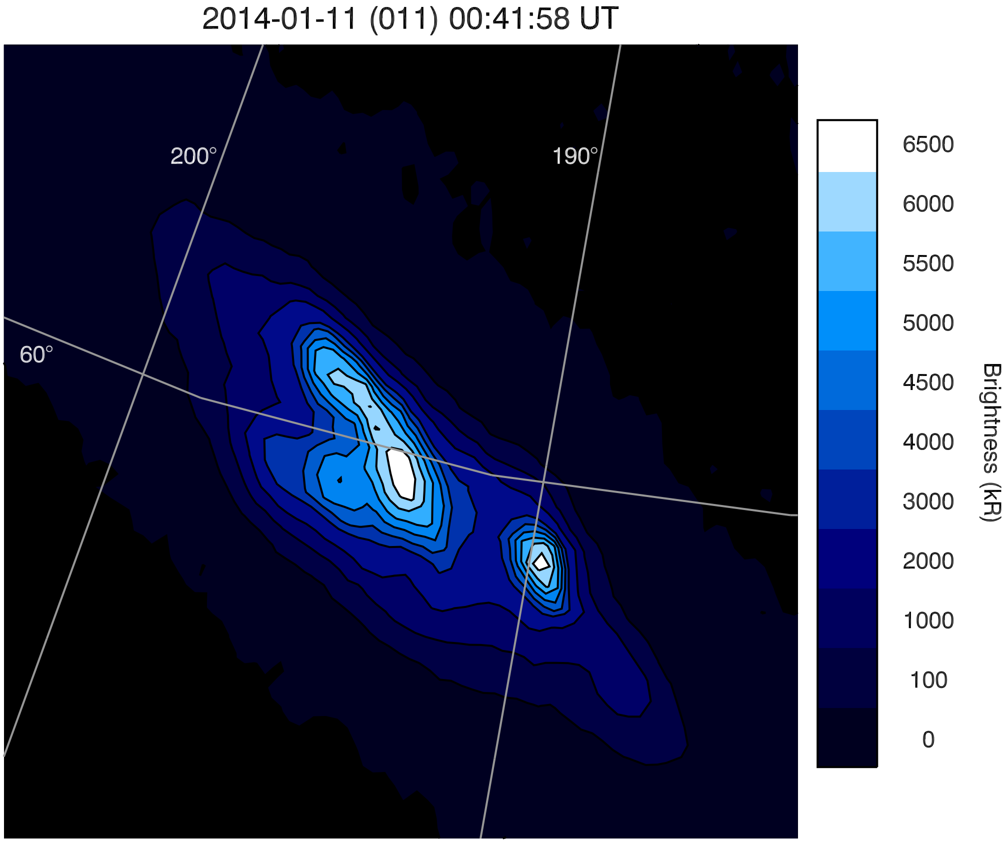

FIGURE 4.2: Polar-projected HST image of feature B taken at 00:41 UT, as in Fig. 1a, showing substructure. Longitude and latitude labels are displayed.

The last image of this sequence (shown in Fig 4.1e) shows the super-rotating spot entering the area of bright and expanded main emission ~200° λ_{III}. The spot's visible lifetime is therefore 20 minutes - but this is not a true 'lifetime', rather the time where it remains distinct from other features. The position implies that the field lines mapping to the spot are in the vicinity of the dawn sector corotation breakdown region (*Cowley and Bunce*, 2001; *Vogt et al.*, 2011, 2015). This is also the region responsible for the main emission. The breadth of the main emission has reduced to the steady state configuration (although dimmer, up to ~400 kR) by the next HST visit at 19:39 UT (shown in Fig 4.1f).

There are two large equatorward emissions at 154-169° (emission C) and 133-152° (emission D). Emission C has bright patches of up to 1600 kR and extends into the main emission oval. Emission D is more diffuse, reaching a peak brightness of only 600 kR and is centered at lower latitudes, extending to within 2° of the IFP contour. The average brightness in emission D is 270 kR. These emissions are present at the beginning of this HST sequence (00:31-00:41 UT, Fig 4.1a), so their generation must have occurred before the transit of the polar spot into the main emission region.

The longevity of the equatorward emissions is also comparable to that described by *Dumont et al.* (2014); the consecutive HST sequences starting at 00:31 UT and 01:01 UT both show the emissions. There are faint structures on images taken at 19:39 UT (second visit, Fig 4.1f, circled green) at the same longitudes as feature C in the previous visit. The faint structures could be a remnant of feature C, which would give a minimum lifetime for this equatorward emission of 18.5 hours.

4.2.2 Magnetospheric Source Regions

In order to investigate the potential magnetospheric source region of the auroral features, we map field lines from the northern hemisphere to the equatorial magnetosphere using the Grodent Anomaly Model (GAM) and the VIPAL models. Figure 4.3 shows the mapped location of the centre of the super-rotating spot (specifically the brightest central point within the 200 kR contour), in the equatorial plane of the magnetosphere alongside the mapped source regions of the extrema of the main emission and two equatorward emissions shown in Fig. 4.1. The red stars show the equatorial mapping of the centre of the super rotating polar spot and the boxes the extrema of the other auroral features. The magnetopause is indicated by the solid black lines and shows both the compressed and the expanded configurations after *Joy et al.* (2002).

The poleward edges of the features were mapped using the flux equivalence method at 170° CML (*Vogt et al.*, 2011, 2015). The spot and poleward edges of the main emission use the GAM internal field model because it provides the most accurate match to the Ganymede footprint at these longitudes (*Grodent et al.*, 2008a; *Vogt et al.*, 2015). Out of the internal field models available, GAM predicts the most tailward source for the spot and main emission, which is consistent with the initial notable high latitude of the spot and the interpretation of polar spots as a result of tail reconnection. For consistency, the GAM model of the internal field was used for the poleward edges of the equatorward emission (*Vogt et al.*, 2011, 2015). The VIPAL internal field model alone was used to map the equatorward edges of the main emission and equatorward emission features (*Hess et al.*, 2011) since they likely map to <15 R_J.

As the polar spot super-rotates around the planet, its mapped radial distance from the planetary centre decreases from 95 to ~70 R_J as it moves from 0400 to 0615 LT. These radial distances are consistent with the locations of reconnection events observed

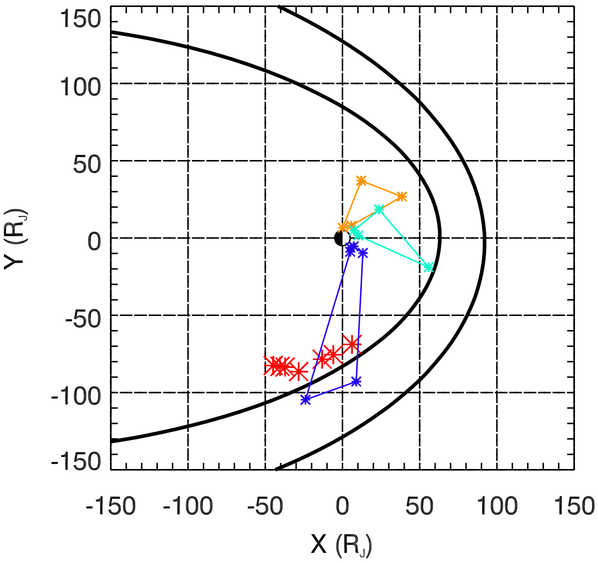

Figure 4.3: The location in the equatorial plane of the auroral features observed on 11 January 2014. The red stars show the equatorial mapping of the centre (specifically the brightest central point of the 200 kR contour) of the super rotating polar spot as it moves over the image sequence and the coloured boxes are the extrema of the auroral features. The poleward edges of the features were mapped using the flux equivalence method at 170° CML (*Vogt et al.*, 2011, 2015) with the GAM internal field model (*Grodent et al.*, 2008a). The VIPAL internal field model alone was used to map the equatorward edges of the main emission and equatorward emission features (*Hess et al.*, 2011). The Sun is to the right hand side. The blue box shows the expanded main emission (B), the green shows the left-hand equatorward feature (C) and the orange shows the right-hand equatorward feature (D). Solid black lines indicate the compressed and expanded magnetopause after *Joy et al.* (2002).

in situ with Galileo (*Kronberg et al.*, 2005) and the statistical x-line in this sector (*Vogt et al.*, 2010). Figures 4.1b-e show that the spot (A) moves closer to the enhanced main emission region (B). Correspondingly, the map in the equatorial plane (Fig. 4.3) shows that the final mapped source region of the spot and the main emission source region are co-located. The total distance between the first and last mapped location of the spot is ∼56 R_J. This corresponds to an average propagation speed of 6450 km/s in the magnetosphere over the 10 minute sequence.

The mapped main emission region (feature B, blue outline) extends from 8 R_J to as far as ∼110 R_J from the planet. The majority of points within this feature, however, map to within 15-45 R_J, which is consistent with the modelled corotation breakdown region of 15-30 R_J (*Vogt et al.*, 2015) in the dawn sector. The source region maps to between 0500-0915 LT.

The brighter equatorward emission source region (feature C, green outline) is farther from the planet than the second equatorward emission source region (feature D, orange outline). The source region of emission C extends over ~8-58 R_J and between 1100-1500 LT. The source region of emission D extends over ~6-45 R_J and between 1445-1730 LT.

4.2.3 Emitted Auroral Power

Figure 4.4 shows the time series of the power in each region of the aurora. The day 011 event dominates the time series. The total auroral power peaks at ~2200 GW. Comparison of the contributions of each auroral region and the morphologies themselves (see Fig. 4.1) show that main emission brightness region is the primary contributor to the power (~1100 GW) and that the breadth of feature B causes the power to 'leak' over the defined regional boundaries into the other regions. There is additionally a significant contribution from the large equatorward emissions (~540 GW). These are similar to the observed power of equatorward emissions observed by (*Bonfond et al.*, 2012). The contribution of the two large equatorward emissions C and D alone is ~390 GW. The super-rotating polar spot does not contribute notably to power in the polar region because of its small size.

The next HST image (19:39 UT, Fig 4.1f) was taken 18.5 hours after the image sequence showing the above features (01:01-01:11 UT, Fig 4.1b-e). The total auroral power decreased from ~2200 GW at 01:11 UT back to ~1300 GW at 19:39 UT on day 011. Using a simultaneous data set from the Hisaki satellite, which measures extreme ultraviolet (EUV) power emitted from the whole northern polar region quasi-continuously, the time interval during which the power was elevated above average values can be constrained to just 7 hours (*Kimura et al.*, 2015). The extremely bright main emission feature B and large equatorward emissions C and D are the primary contributors to the power. The long-term variations in power are discussed by *Badman et al.* (2016).

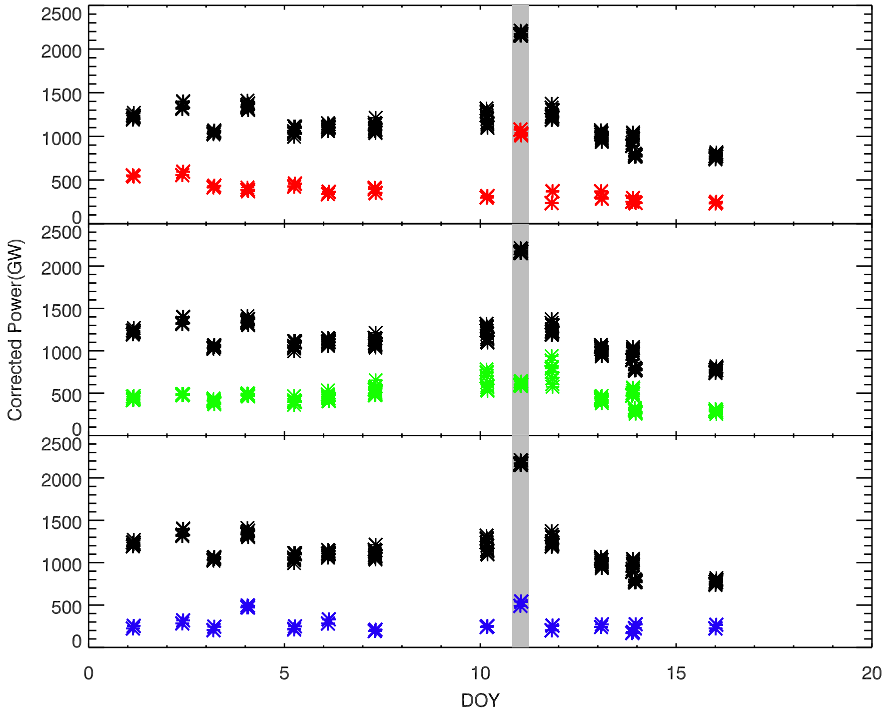

FIGURE 4.4: Power emitted from the different auroral regions over the 2014 HST campaign. The regions shown in colour from top to bottom are the main emission region (red), polar region (green) and the equatorward region (blue). The vertical grey shaded region indicates the HST visits of interest at 01:00 UT on day 011. The boundaries of these regions are indicated on Figure 4.1f. In each plot, the black points indicate the total power in order to indicate the contribution of each region to the total power.

4.3 Discussion: Interpretation of Auroral Signatures

Polar spots which are not super-rotating have been interpreted as auroral signatures of magnetic reconnection (*Grodent et al.*, 2004; *Radioti et al.*, 2008a, 2010). The super-rotating polar spot (A) is also interpreted as the auroral response of magnetic field reconnection in the magnetotail because of its similar size, direction of motion, and location. The super-rotating spot appears at higher latitude relative to the main emission compared to the other polar spots seen in this campaign, such as on day 004 (not shown here). The typical separation of these spots from the main emission is around 1° of latitude, consistent with observations of polar spots by *Radioti et al.* (2008a). However, on day 011, the spot is as far as 3.8° poleward of the campaign average main emission location. In general, more poleward emissions correspond to events farther from the planet, so this indicates that reconnection is occurring further from the planet (or at least farther from the corotation breakdown/main oval region) in the day 011 case than in other previously reported polar spot cases.

Two explanations of the unusual spot observations are presented. Firstly, following *Nichols et al.* (2014), the site of magnetic reconnection itself propagates rapidly as flux over a large spatial region reconnects. As the field dipolarises, Alfvén waves are launched from the reconnection site and generate an auroral signature. As the reconnection site moves, so does its ionospheric footprint. It is noted that the mapped location of the super-rotating spot in the magnetosphere follows the location of the statistical Vasyliunas cycle x-line in the magnetotail (*Vogt et al.*, 2010), i.e. moving closer to the planet with increasing LT. In this scenario, to match the observations the x-line would need to propagate at ∼6500 km/s.

Alternatively, hot tenuous plasma flowing very quickly planetward from a distant reconnection site can produce a signature at very high latitudes relative to the main emission and rotate around the planet at high azimuthal velocity. By analogy to auroral streamers at Earth, as the field line moves azimuthally and planetward around dawn, the footpoint in the ionosphere is also expected to move (*Henderson et al.*, 1998; *Nakamura et al.*, 2001; *Nishimura et al.*, 2011). The relatively fast contraction of the dipolarising field line in the magnetosphere past the surrounding field lines causes a gradient in B_z and therefore a field-aligned current system (e.g. *Kasahara et al.* (2011)). This has been observed at Earth by the THEMIS mission (*Keiling et al.*, 2009). *Cowley et al.* (2015) showed that for a simple 1D current sheet, a newly-reconnected field line (dipolarisation) will contract planetward with a speed equal to the difference between the Alfvén speed and the tailward flow of plasma on stretched nightside field lines. Taking the observed speed of the auroral spot, ∼6500 km/s, as the speed of planetward contraction and an estimate of the downtail plasma flow as 350 km/s (*Krupp et al.*, 2004; *Cowley et al.*, 2015), the Alfvén speed must be >6000 km/s. For a typical value of the field strength outside the current sheet of 7 nT (taken at 80 R_J) (*Kivelson and Khurana*, 2002), this requires a very low ion mass density (e.g. a proton density of 1×10^{-3} cc^{-1}), indicating that, in this scenario, reconnection occurred in a low density region such as the lobe.

On day 011 (00:31-01:11 UT), the main emission is locally broadened and bright at emission B. The mapping of the path of the super-rotating spot indicates reconnection inflows into this region. This implies that there are flows into the main emission region from reconnection events in the more distant magnetotail. Prior reconnection events may have caused similar flows. The resulting flow shears and dipolarised field lines generate field-aligned currents and enhanced auroral emission (*Kasahara et al.*, 2013; *Palmaerts* *et al.*, 2014), as indicated by the structure of feature B, shown in Fig 4.2. These effects could be compounded by an increase in ionospheric conductivity in the ionosphere locally to generate the bright signature observed. Increases in electron precipitation can increase the ionospheric conductivity and therefore increase the coupling currents, generating bright and broadened aurora (*Nichols and Cowley*, 2003, 2004).

The main emission in feature B has returned to a normal configuration by the second visit of day 11 (Fig 4.1f). Assuming that a significant proportion of the total EUV power measured by Hisaki was from the large and exceptionally bright feature B, the lifetime of feature B may be constrained to just ∼7 hours. Feature B is interpreted as the result of enhanced flow shears, so it is suggested that enhanced inflow from the tail could also have continued for ∼7 hours.

Emission regions C and D are unlike the injection morphologies described by *Dumont et al.* (2014), which are smaller and brighter. They are also larger than the emissions characterized by *Mauk et al.* (2002) as signatures of injections in the inner magnetosphere.

Similar features were identified in observations from 2007 with associated high powers in the equatorward region (*Nichols et al.*, 2009a; *Bonfond et al.*, 2012), which were related to increased volcanic activity. However, in the present case, observations of the Io sodium nebula brightness (*Yoneda et al.*, 2015) and EUV power of the inner torus (*Tsuchiya et al.*, 2015) show no indication that Io volcanic activity has increased in the weeks prior to or during this observational interval. Yet, a similar occurence rate of injection signatures as in 2007 are observed. It is therefore suggested that inflow from reconnection causes hot plasma injections to generate the large signatures observed (analogously to bursty bulk flows at Earth), without requiring increased Iogenic outflow as in the 2007 case.

Following the discussion above, features C and D could have formed following reconnection-driven inflows in the preceding hours. It is known that polar spots appear in groups and that reconnection events can be clustered (*Radioti et al.*, 2008a), occurring on successive fieldlines (*Vogt et al.*, 2014). During long (up to 18 h) periods of reconnection across open and closed field lines, electron jets at the dipolarisation front were detected travelling planetward at 7500-17000 km/s (*Kasahara et al.*, 2011). This is similar to the velocity of the super-rotating auroral spot inferred from the magnetic mapping (6450 km/s).

The equatorward emission D lies within the longitudinal range (150° $< \lambda_{III} <$210°) and expected brightness (270 kR) identified for the secondary oval associated with the PAD boundary (*Grodent et al.*, 2003; *Tomás et al.*, 2004b; *Radioti et al.*, 2009). Enhancement of this feature can also be attributed to hot plasma injections since the hot population would enhance the waves responsible for the electron scattering (*Tomás et al.*, 2004a; *Woodfield et al.*, 2013). This phenomena is discussed in chapter 5.

Previous observations show auroral signatures of injections can last over 34 hours (*Bonfond et al.*, 2012). Possible remnants of equatorward features C and D have been identified in HST observations made 18.5 h later (Fig. 4.1f). This implies that the effects of hot plasma injections (e.g. further planetward transport and wave-particle interactions) can continue for 18.5 hours.

In summary, the HST image auroral signatures have been interpreted as hot plasma inflows from tail reconnection (super-rotating polar spot), flow shears in the dawnside middle magnetosphere (locally bright and broad dawnside main emission) and evidence of hot plasma injections in the inner magnetosphere (equatorward emission). It is not suggested that the magnetospheric counterpart of the super-rotating spot causes the other features observed at the same time, but that the super-rotating polar spot signature is part of a prolonged reconnection interval.

Reconnection can proceed on open field lines if all the closed field lines have first been reconnected. The super-rotating spot is seen at particularly high latitudes compared to previously reported spots, which are thought to have formed as part of the Vasyliunas cycle. Open field lines will map to more poleward emissions than the closed field lines and Dungey cycle reconnection is expected to take place in the far tail (*Badman and Cowley*, 2007). It is suggested that the observed super-rotating spot signature appears near the end of a prolonged reconnection interval, involving (Vasyliunas-type) closed field line reconnection, possibly proceeding onto open field lines.

4.4 Global Picture from Radio Observations

We now examine Jupiter's radio emissions for additional evidence of magnetospheric dynamics. *Louarn et al.* (2014) linked tail reconnection inflows to intensifications of the HOM and new sources of nKOM in the outer Io plasma torus within 1 Jupiter rotation. Intensifications of non-Io DAM has been sometimes related to solar wind shocks, although the processes are not understood (*Hess et al.*, 2014). Increases in HOM have also been related to high solar wind dynamic pressure (*Gurnett et al.*, 2002).

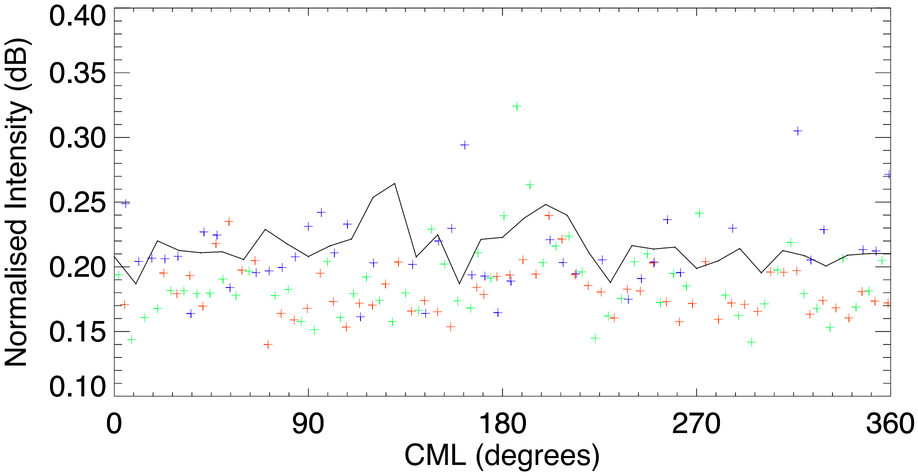

FIGURE 4.5: Averaged intensity at 3.5 MHz from WIND/Waves sorted by CML for the planetary rotation before (blue, 15:10-01:00 UT), during (green, 01:00-11:10 UT) and after (red, 11:10-21:10 UT) the auroral sequence in Fig 4.1b-e on day 11. The solid line shows campaign average intensity, in 10° bins. The coloured points plot the intensity averaged over 10° bins for successive rotations.

WIND Radio and Plasma Waves (WAVES) data (*Bougeret et al.*, 1995) were examined for this interval (data is available through CDAWeb). Figure 4.5 shows the average intensity from days 001-016 at one frequency band (3.5 MHz), where HOM is expected, as a function of CML (black line). The occurrence probability of HOM is known to peak at CML around 30°, 120° and 270° (*Galopeau and Boudjada*, 2005). The peak at 120° indicates the HOM was detected by WIND at this frequency during the interval despite the significant solar activity. This statistical peak will be ignored in the analysis of the HOM associated with this transient event.

The blue, green and red points on Fig 4.5 show the intensities at 3.5 MHz from the planetary rotations around the auroral image sequence shown in Fig 4.1b-e at 01:01-01:11 UT. We show the rotations before and after the image sequence in order to show that the HOM signature observed is non-periodic. The blue points show the planetary rotation before the auroral sequence, the green starts at the time of the auroral sequence and the red at the rotation after the sequence. The intensity of emission during the end of the first rotation (blue, 15:10-01:00 UT) and beginning of the middle rotation (green, 01:00-11:10 UT) around CML 150-220° exceeds the campaign average. The rotation after the image sequence (red, 11:10-21:10 UT) does not show significant intensity around the same CML, as expected for a signature that is non-periodic. The majority of the points are lower intensity compared to the campaign average because there is lower type III burst activity at this frequency around day 011 compared to the rest of the campaign. The blue point at 310° CML above the campaign average has been checked against the frequency-time spectrogram and is not associated with HOM, but is associated with a solar burst on day 010. The other HOM associated frequency bands were checked and CML 150°-220° consistently showed increased intensity. Other points above the campaign average show variation across other frequency bands, so these are not HOM.

The raised intensity at HOM frequencies around the time of the HST images is also evident in Fig 4.6a, the frequency-time spectrogram, at 00:30-02:30 UT between 0.7 - 4 MHz. The emission frequency increases with time, opposite to the solar type III bursts also occurring. This potential HOM burst is detected simultaneously with the intense UV emission observed by HST (Fig 4.1b-e). The specific UV auroral feature that the HOM corresponds to is unknown, although HOM is expected to be related to inner magnetospheric sources (L-shell < 30) (*Ladreiter et al.*, 1994; *Zarka et al.*, 2001; *Imai et al.*, 2015). Fig 4.3 shows part of the main emission and equatorward emissions relate to sources up to L $\sim$30.

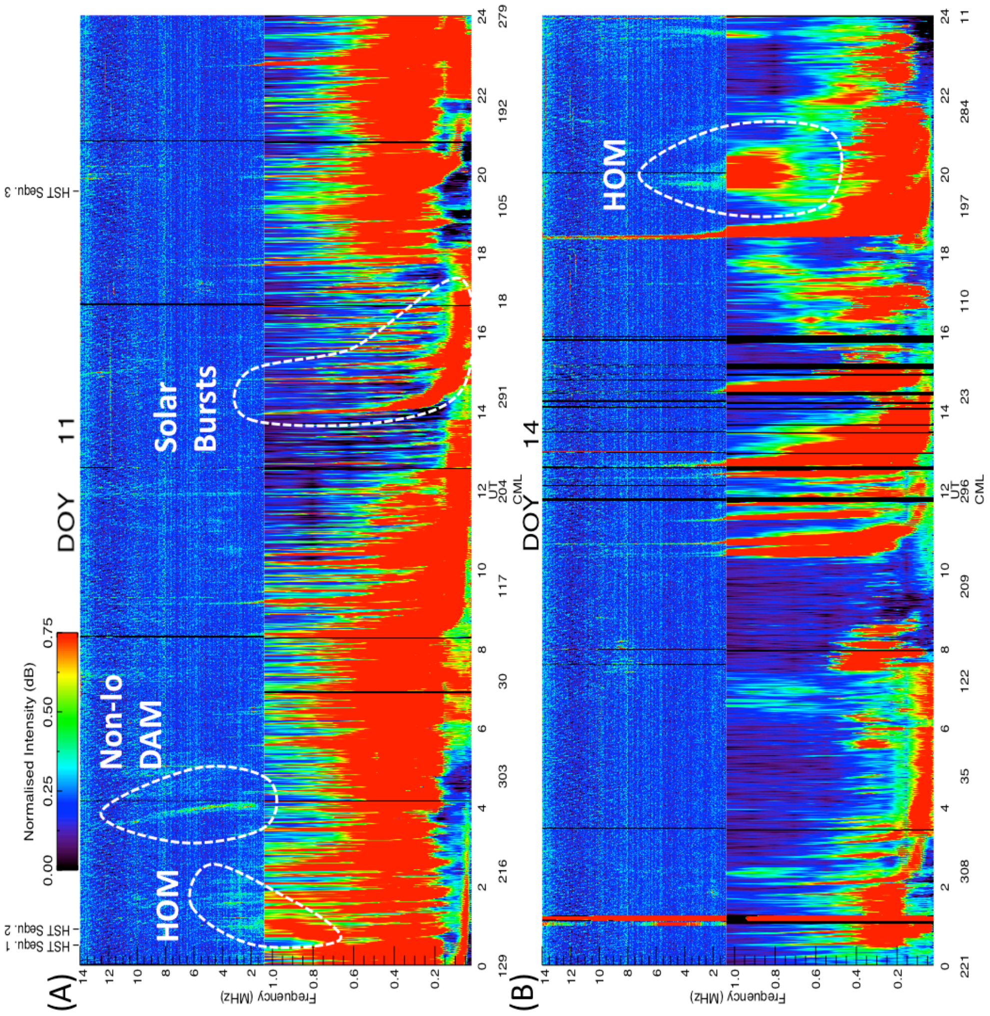

FIGURE 4.6: Radio spectra from Wind WAVES RAD1 (20-1040 kHz) and RAD2(1.075-13.82 MHz) detectors on day 011 (a) and day 014 (b). The flux density of both receivers is not cross-calibrated, producing the apparent discontinuity across the detector ranges. HOM emission is expected up to a few MHz. The HOM emission on day 011 is the between ~00:30-02:30 UT and 150-220° CML, between 0.8-4 MHz. The HST image sequences are marked for indication: HST Sequence 1 (00:31-00:41 UT), HST Sequence 2 (01:01-01:11 UT) and the next sequence showing the relaxed main emission state, HST Sequence 3 (19:39-19:49 UT). A clearer HOM signal for comparison on day 014 is between ~19:30-21:00 UT and 205-265° CML, between 0.7-6 MHz. The non-Io DAM signature on day 011 is at ~04:00 UT and ~270° CML. A typical solar burst showing decreasing frequency with time is highlighted. The colour scale is saturated at 1.5 dB to show Type III solar bursts.

For comparison, in Fig 4.6b we show another HOM burst from 19:30-21:00 UT between 205-265° CML on day 014, which was also correlated with intense UV emission (*Kimura et al.*, 2015). Because of its higher power this feature is easier to distinguish on the frequency-time spectrogram, but otherwise its characteristics are similar to those seen at 00:30-02:30 UT on day 011, supporting our interpretation of the day 011 feature as a HOM burst associated with enhanced UV emission.

Non-Io DAM emission was also observed at 04 UT, CML 275° at 1-10 MHz. The vertex-late shape corresponds to a dusk source (*Hess et al.*, 2014). At this time, ∼1/4 rotation after the images shown in Fig 4.1b-e, the bright main emission feature B and equatorward feature C would be in the dusk and post-dusk sectors, assuming corotation with the planet. *Hess et al.* (2014) suggest DAM sometimes exhibits a correlation with solar wind shocks, as has been detected in the UV (*Clarke et al.*, 2009; *Nichols et al.*, 2009a). However, within ∼1 day accuracy, there is no evidence in the propagated SW data of a SW shock arriving at Jupiter at this time (*Tao et al.*, 2016b). This could therefore be an internally triggered DAM emission, as identified by *Hess et al.* (2012, 2014).

The intensifications of the emissions identified as HOM and DAM support the interpretation that a global magnetospheric disturbance was occurring, involving tail reconnection and disturbance of the outer Io plasma torus (*Louarn et al.*, 2014). The large equatorward emissions are thought to be generated by inflows prior to the HOM detection and HST imaging sequence on day 011. This implies that there has been magnetotail reconnection prior to the time of the HST observations. This could be analagous to SKR and auroral UV enhancements and large scale plasma injections at Saturn (e.g. *Mitchell et al.* (2009); *Lamy et al.* (2013)).

4.5 Conclusions and Summary

HST observations from day 011 January 2014 (01:01-01:11 UT) show bright and unusual auroral forms, which are interpreted as part of an inward radial transport sequence. A super-rotating polar dawn spot (feature A) was observed and interpreted as the signature of tail reconnection. The spot could be either the signature of the propagation of the X-line in the tail, or the signature of dipolarised field travelling planetward. The spot was observed to move into a broad and bright patch along the dawnside main emission (B). The brightening in this region could be related to flow shears associated with earlier inflows. The presence of hot plasma originating from the tail could lead to the presence of bright equatorward emissions (C and D) as the signatures of earlier hot plasma injections [e.g., (*Thomsen et al.*, 2015)]. The images are thought to capture part of a prolonged period of reconnection.

Radio emissions measured by WIND suggest that HOM and non-Io DAM signatures are associated with the sequence of auroral signatures (01:01-01:11 UT). These are interpreted as inner magnetospheric and internally driven disturbances. *Louarn et al.* (2014) previously showed HOM should occur within 10 hours of tail inflows. The enhancement/detection of the HOM supports our interpretation of the UV auroral signatures as a sequence of radial transport.

The bright and broad dawnside main emission feature magnetically maps to the morphological boundary between the hot tail inflows and inner magnetosphere region. The Hisaki EUV power is only elevated for about 7 hours above the average power level, so assuming the main contributor to the EUV power is the main emission feature, the lifetime of feature B may be constrained to just ∼7 hours. If flow shears in the middle magnetosphere are the cause of the emission, then the flow shears and therefore the enhanced inflow may also be constrained to a duration of 7 hours. The equatorward images may show emission for at least 18.5 hours. This implies the interval of hot plasma injections and its consequences can be at least 18.5 hours duration. The next chapter further discuss the auroral injection signatures and the plasma that causes them.

Chapter 5

Response of Jupiter's Secondary Auroral Oval to Hot Plasma Injections

5.1 Introduction

In the previous chapter, hot plasma inflows triggered by reconnection were shown to in turn trigger hot plasma injections in the inner magnetosphere, as close as 8 R_J. This is likely due to a predominantly internally driven global transport process. This hypothesis has been further explored by *Louarn et al.* (2014) using HOM and n-KOM radio data. *Kimura et al.* (2015) have also explored this using the Hisaki spacecraft and they identified a transient brightening in the auroral power corresponding to a large injection event. From the signatures discussed in chapter 4, the auroral power increase presumably comes from the main emission region brightening and increased low latitude emission. This chapter addresses the consequences of injections of hot plasma in the inner magnetosphere, specifically in the region 10-17 R_J. In this region, sometimes known as the PAD transition region, wave-particle interactions are thought to scatter electrons into a field aligned distribution. The particles may then form a secondary auroral oval due to precipitation at lower latitudes than the main emission (*Bhattacharya et al.*, 2001; *Grodent et al.*, 2003; *Tomás et al.*, 2004a,b; *Radioti et al.*, 2009).

Hot plasma injections in the PAD transition region may be expected to act as a particle source and source of energy for wave growth for wave-particle interactions and therefore increase scattering into the ionosphere (*Xiao et al.*, 2003), causing the second oval to become more visible. Due to the confined local time nature of the hot plasma injection, it may be expected that the second oval forms in latitudinally constrained arcs. We also show that due to field gradient-curvature drifts, the signature may become longitudinally spread over time. This chapter quantifies the location and intensification of the second oval feature in response to the occurrence of hot plasma injections.

5.2 Observation Overview

The images are taken from the 2014 HST campaign between days 1-14, as in the previous chapter and processed as outlined in chapter 2, instrumentation. The spectral images are also processed in line with chapter 2, instrumentation.

Figure 5.1 gives examples of the relevant morphologies observed. There is an injection signature on day 4, appearing outside the main oval (top left). On days 5 (not pictured), 6 (Fig. 5.1b) and 7 (Fig. 5.1c), the second oval appears in bright arcs with diffuse emission between sections. After another injection event on day 11 (Fig. 5.1d), a fuller second oval is seen on day 13 (Fig. 5.1e). A further injection event on day 14 is indicated by a Hectometric (HOM) radio emission at 20:00 UT, which has previously been linked to large reconfiguration events and injection events (*Louarn et al.*, 2014) and chapter 3, Radial Plasma Transport. On day 16 (Fig. 5.1f), the fullest second oval is observed.

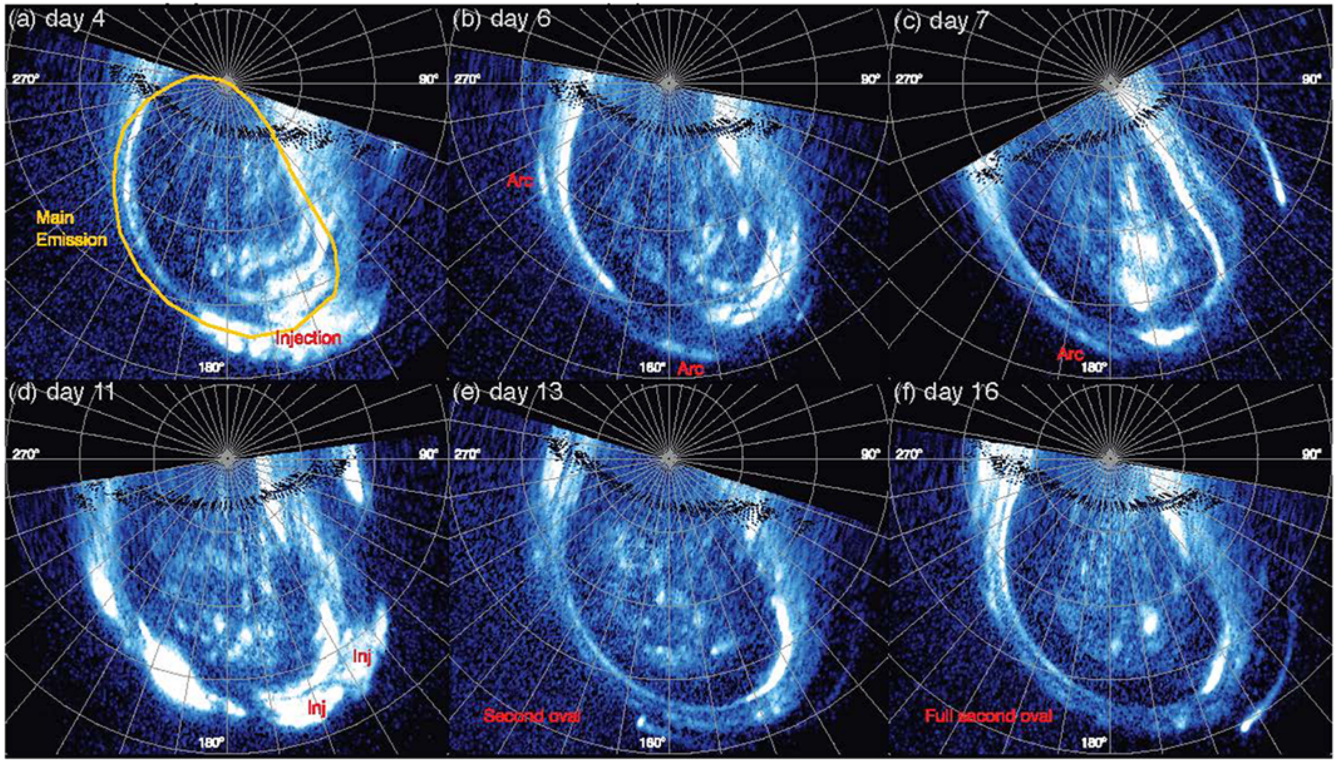

Figure 5.1: Six polar projected images taken with the HST, with log intensity scale saturated at 400 kR. For each image the exposure time was 100 s. The grey lines indicate a 10° × 10° jovicentric latitude-system III longitude grid. The image is oriented such that 180° system III longitude is directed toward the bottom and labels are displayed in grey. Top row, left to right, a) Injection event, day 4 01:10 UT, average main emission position for campaign in gold, b) day 6 02:35 UT, c) day 7 07:16 UT. Bottom row, left to right, d) Injection event, day 11 00:31 UT, e) day 13 22:39 UT, f) After HOM emission on day 14, day 16 00:03 UT.

Three large injection events are detected through the 2014 HST campaign on days 4, 11 and 14 using the Hisaki instrument. In all three cases, Hisaki measurements show sudden transient increase in auroral power, indicating a reconfiguration and injection events (*Kimura et al.*, 2015). On days 4 and 11, HST images show large auroral injection signatures (see Fig. 5.1a and d). On day 14, a large HOM emission is observed.To analyse the response of the second oval feature to the injections, the campaign was split into two groups: observations which were within three days after an injection event (days 5, 6, 7, 11, 13 and 16) and the other observations (days 1, 2, 3, 4 and 10).

5.3 Feature Detection Algorithm

An automated detection algorithm was used to select the second oval points. The average position of the main emission over the campaign was found as follows: the average campaign image was binned into 1° system III longitude bins. The maximal brightness was found in each bin with the caveat that the latitude of maximal brightness was not to change more than 2° between adjacent longitude bins. This confines the brightness of the main emission to a strip a few degrees in latitude. The average main emission position for the campaign is shown in black crosses on Fig 5.2. For each visit, slices perpendicular to the main emission were taken at ∼0.25° intervals along the oval. Firstly, the main emission position along the slice was found. The outer bound of the slice is set as the footpoint of the field line that crosses the equatorial plane at 9 R_J (mapped with the VIPAL model (*Hess et al.*, 2011)); the inner bound is 0.5° poleward of the average main emission position. A Gaussian distribution is fit along the intensity profile of the slice (on the assumption that the main emission is bright and confined). The peak position of the Gaussian is taken as the main emission peak position for that slice if it is above 200 kR (to avoid selecting bright second oval peaks). The position of the main emission for the visit was found by averaging the points' positions in 20° spatial bins in longitude around the central point at 175° longitude, 66° latitude (which was empirically determined).

The second peaks were then found as follows: an average main emission position is found for each visit by incrementally expanding the average main emission shape from 0.25° of its original shape till it best fits the main emission points found for that visit. This maintains the expected shape of the main emission for regions where the emission is dim on that visit. To define the latitudinal 'slice' at each location, the inner bound of the intensity profile along the slice is 0.5° equatorward of the adjusted average main emission position and the outer bound was the footprint of the field line that crosses the

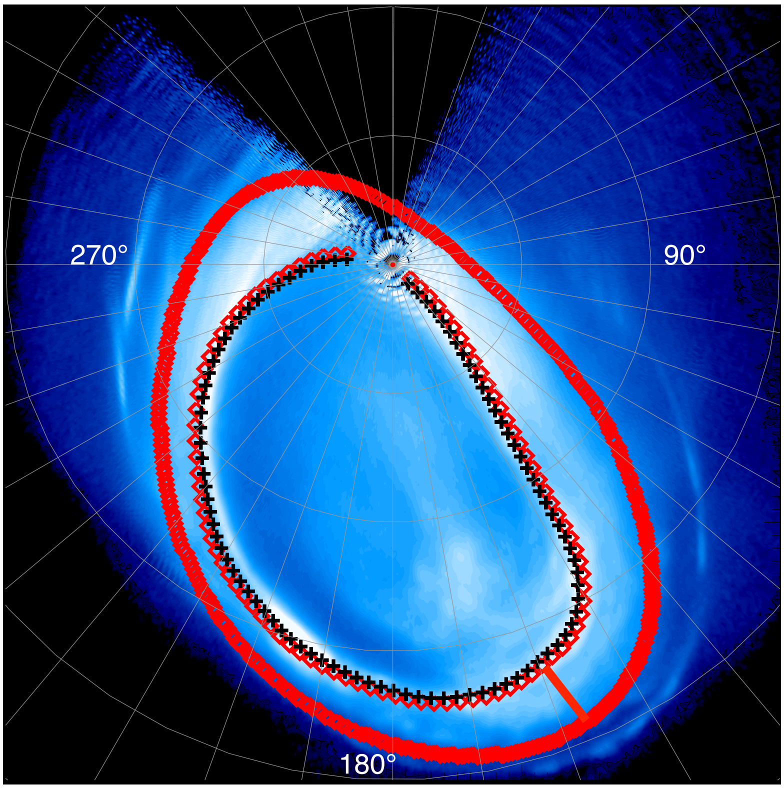

Figure 5.2: Polar projected HST UV 2014 campaign average image with inner and outer boundaries of intensity slices (red diamonds) used for second peak detection. Inner boundary is an example adjusted main emission; outer emission is the footpoint of the field line that crosses the equatorial plane at 7 R_J mapped with the VIPAL model. For peak detections, slices are taken between pairs of points. Average main emission also shown (black crosses). An example slice is shown around 160° longitude in red.

equatorial plane at 7 R_J, (just outside the orbit of Io). These boundaries are shown on Figure 5.2.

The brightness profile across the slices were examined. Examples of these profiles are shown in Fig 5.3. It was assumed that in the absence of a second oval peak, the intensity falls exponentially from the main emission, so each intensity slice had a fitted Gaussian background across the slice removed (blue, top panel Fig 5.3), with intensity values below the Gaussian set to zero. The peak of the remaining intensities (red) was selected as the second oval point. If a Gaussian with a peak greater than a threshold of 200 kR could not be fitted (i.e. the main emission is dim), then the greatest peak outside the adjusted average main emission was selected as the second oval point (bottom panel Fig 5.3). Second oval points with brightness below 40 kR and above 400 kR were rejected - these are too dim or bright to constitute a typical second oval feature. Points greater than 400 kR are typical of injection signatures or main emission brightness. The longitude, latitude and peak brightness of each point was measured for each slice per visit. This was repeated for each slice per visit.

The points were then refined based on a derived average position as follows. The peaks detected were binned into 20° longitude bins (as for the main emission point selection) and an average second emission position for the visit was found. Data points which lay more than 1° away from this derived average position or within 1° latitude of the adjusted main emission were rejected so that a dim and broad main emission point would not be mistakenly selected as a second oval point. After this refinement, the longitude, latitude and peak brightness of each point was measured again. This was repeated for each visit.

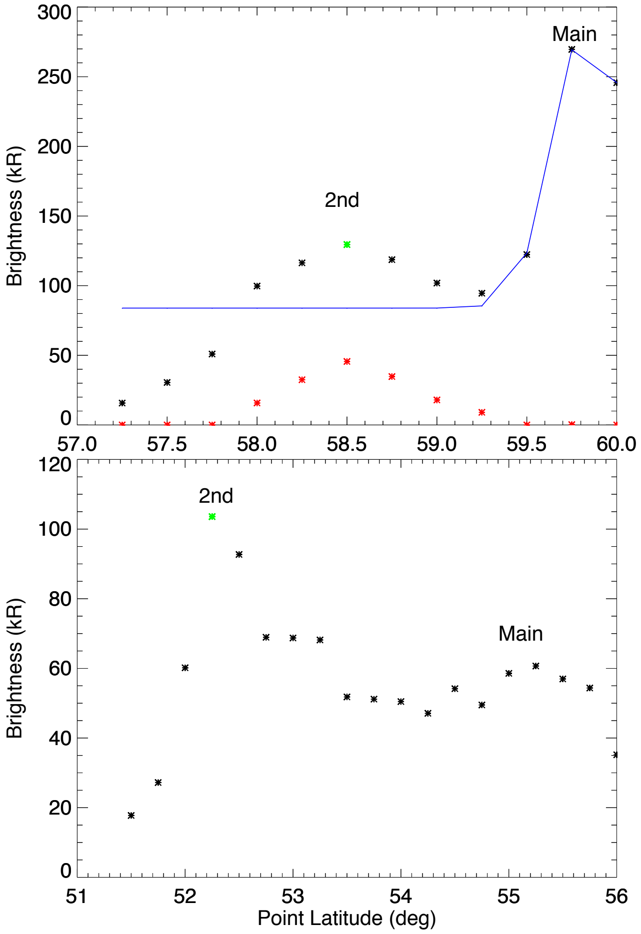

FIGURE 5.3: Two example intensity profiles from day 16 showing the second oval point selected (green). (Top) 148° longitude, clear main and second oval peaks; Gaussian profile (blue) subtracted from intensities (black) to give residual emission (red). (Bottom) 160° longitude, clear second but dim main emission; highest peak selected.

The moon footprints of Ganymede and Europa can appear in the region of interest and their effects are two-fold. Firstly, the moon footprints themselves will contribute to the brightness profiles. Secondly, it is thought that the moons may be able to cause enhanced pitch angle scattering of particles as they pass through a region (*Santolík et al.*, 2011). Points that lie either 1° ahead or 4° behind in longitude and within 1° latitude of the projected position of the Europa and Ganymede moon footprints (found by matching the moon phase to the footprint contour in *Hess et al.* (2011)) have been removed.

Only points found between longitudes 150-240° were investigated. Longitudes greater than 240° were not accessed in many visits due to the viewing geometry, or tend to be observed close the planetary limb, so may appear artificially brightened. At longitudes less than 150°, the Equatorward Diffuse Emission (EDE) region reported in *Radioti et al.* (2009) is prominent. The EDE region appears broad in latitude and has a low brightness. This is not the type of morphology that the program is designed to select, although the generation mechanism is likely related to that of the second oval. Points found on images with large injection signatures (day 4 and 11), expanded and disjointed emission (day 2), or with exceptionally poor viewing geometry (visit 2 on day 13) are rejected.

To find the average second emission location for the whole campaign, all accepted points were binned into 10° longitude bins and the average position and brightness were found.

5.4 Results

5.4.1 Second Oval Location

Figure 5.4 shows two example outputs for days 6 (a) and 16 (b) overlaid with points where second oval points are detected. The images are averaged over the visit. The third panel shows both sets of points overlaid with the campaign average main emission in gold to guide the eye. Green points are from day 6 and red points are from day 16. Day 6 shows two clear bright arcs, the 150 kR contours of which extend to 220°-242° longitude and 66°-71° latitude and 170°-182° longitude and 53°-55° latitude respectively. The automated detection has picked out these points as well as a fainter arc between the two. The three right most points from day 6 (panel a) are examples of the detection failing to select the second oval and selecting either diffuse emission or the edge of the disjointed main emission instead - the points form less of an arc and therefore do not consitute the second oval. The brighter features of the oval on day 16 have also been detected.

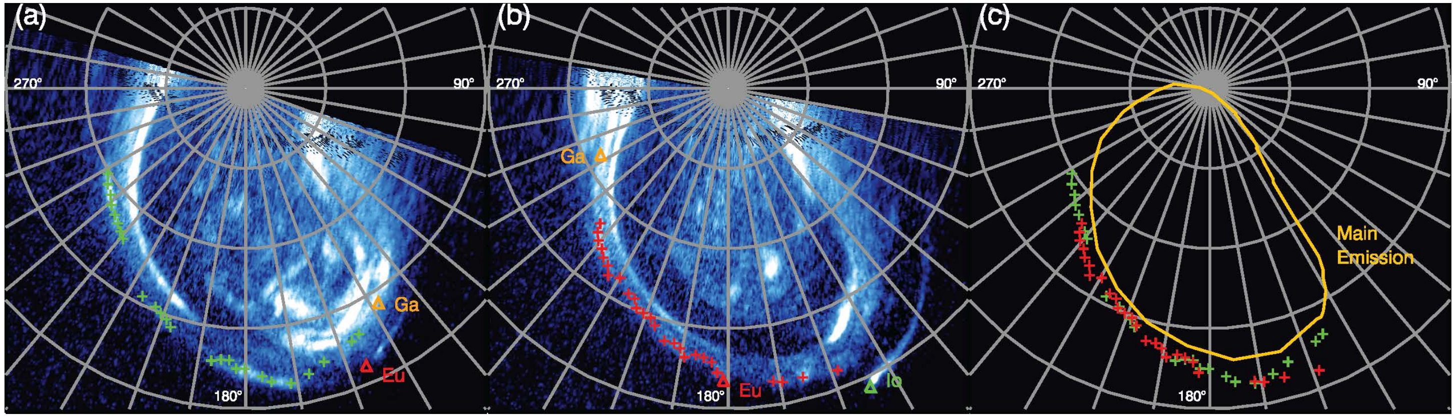

FIGURE 5.4: Two HST images from (a) day 6, and (b) day 16 with overplotted selected second oval points. (c) Second oval points from both day 6 (green) and day 16 (red), with the campaign average main emission to guide the eye. Moon footprint positions are also overplotted.

Figure 5.5a shows the mean average campaign image with the position of the second oval and the Ganymede (orange) and Europa (red) footprint contours, detected between 150-240° longitude (*Hess et al.*, 2011). The average position falls close to the Ganymede footprint and tends to be between the Ganymede and Europa footprints. The moon footprint flux tubes in the equatorial plane lie at the moon, so the statistical position of the flux tubes forming the second emission in the equatorial plane lie between the two moon orbital paths, i.e. between 9.5 (Europa) and 15 R_J (Ganymede). Yellow error bars indicate ± 1 standard deviation either side of the mean in each bin and they point towards the centre used for finding the average binned second oval location. The points are confined to an oval that is narrow in latitude and spread across all longitudes sampled by the detection algorithm. The average ionospheric longitude and latitude can be found in Table 5.1.

HST images taken on days 5, 6 and 7 (Fig. 5.1) show evolution following an injection event on day 4. There are three arcs of emission constrained in latitude centered around 230°, 200° and 180° longitude on day 6. Figure 5.4 shows the points identified by the algorithm on days 6 and 16 superimposed on the HST images. As mentioned above, the right most detected points from day 6 (green) should be ignored since they are not the second oval emission, but correspond to the edge of the broader and more diffuse main emission. The arc features (green) of day 6 lie along the same line of 'full' oval points (red) taken from day 16.

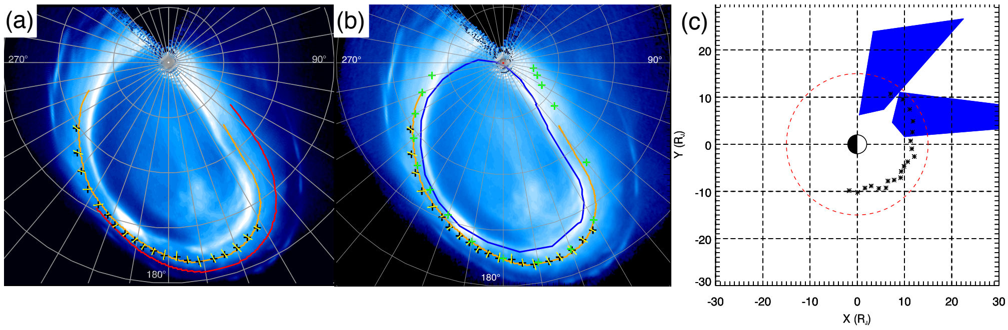

FIGURE 5.5: (a) Average campaign emission image with overplotted moon footprint contours (Europa in red, Ganymede in orange) and second oval points (black) with errors (yellow) of ±1 standard deviation either side. (b) Average campaign image with average main emission (blue), second oval position (black) with error bars (yellow), the Ganymede footprint contour (orange) and previous second oval points from (*Tomás et al.*, 2004b) (green). (c) The location in the equatorial plane of the auroral second oval (black) detected between 150-240° (in the ionosphere), and injections signatures (shaded blue) observed on 11 January 2014 (their position is consistent with e.g. (*Louarn et al.*, 2014)). The red circle shows the 15 R_J line, which is the approximate orbital path of Ganymede. The VIPAL internal field model was used to map the features (*Hess et al.*, 2011) with a CAN current sheet (*Connerney et al.*, 1981). The positive x-axis points to the Sun and the mapping is performed for 180° CML.

TABLE 5.1: System III Longitude and Latitude of Mean Second Emission

Ionospheric Longitude (°)	Ionospheric Latitude (°)	Equatorial Radial Distance (R_J)	Equatorial Longitude (°)
152.00	56.00	12.8	123.4
156.25	55.00	13.6	135.4
160.00	54.25	13.4	146.3
164.00	53.75	12.9	157.5
167.75	53.50	12.1	167.6
171.25	53.50	11.5	176.4
174.75	54.00	11.7	184.7
178.00	54.75	12.5	192.2
181.25	55.00	11.5	199.2
184.25	55.50	11.1	205.3
187.50	56.25	11.1	211.8
190.50	57.25	11.7	217.8
194.25	58.00	11.0	224.3
198.00	58.75	10.2	230.3
201.50	60.25	11.1	236.7
206.50	61.50	10.5	244.0
212.50	62.75	9.4	251.6
218.75	64.75	9.5	260.1
225.50	67.25	10.2	269.5
234.75	69.75	10.0	280.0

Previous work by *Tomás et al.* (2004a,b); *Tomás* (2005) has linked the second oval appearance to the PAD boundary in the vicinity 10-17 R_J. Wave-particle interactions (pitch angle scattering) in the region 10-17 R_J (the inner magnetosphere) are thought to scatter electrons into a field-aligned distribution, leading to auroral precipitation and to a second auroral oval. Figure 5.5b shows the position of the previously reported second oval (green) (after *Tomás* (2005)) compared to the second oval (black with yellow error bars) detected in this work from the 2014 HST campaign. Points found in this work closely follow the Ganymede footprint contour, corresponding to a source close to the Ganymede orbital path (at around 15 R_J). The previous work shows the second oval (green) lie slightly poleward of the second oval points and errors found in this current work around 200-210° longitude. This corresponds to a source that is further from the planet than that of the current work. In *Grodent et al.* (2003), it is suggested that the second oval emissions merge with the main emission around 205° longitude; we found the two emissions do not merge, but stay separated over 150-240° in the January 2014 events.

5.4.2 Magnetic mapping of features to equatorial plane

In order to investigate the potential magnetospheric source region of the auroral features, the field lines are mapped from the northern hemisphere to the equatorial magnetosphere using the VIPAL model. The VIPAL model (*Hess et al.*, 2011) is an update to the VIP4 internal magnetic field model and is based on Voyager and Pioneer magnetic field measurements, modeling of the lowest orders of the magnetic anomaly and corrects for the longitudinal position of the magnetic field lines mapping to Io's orbit. The points lie close to the Ganymede footprint contour, corresponding to a source around 15 R_J where the magnetic field begins transitioning from a more dipolar to a stretched configuration due to plasma sheet stretching. Therefore, there the CAN current sheet model is used in the mapping (*Connerney et al.*, 1981). Whilst the current sheet is known to vary in time, this approximation assumes it and its current are steady.

Figure 5.5c shows the mapped location of the average second oval position calculated from the automated detection program (black) taken between 150°-240°, the injection signatures from day 11 (blue) and the 15 R_J contour (red), roughly co-located with the orbit of the moon Ganymede. The mapped radial distance and equatorial longitudes can be found in table 5.1.

According to this mapping, the radial position of the second oval source varies between 9.4-13.6 R_J, consistent with the auroral location between the Ganymede and Europa footprint contours as shown on Fig 5.5a. It has been detected in the region 123°-279° system III longitude. The injections lie between 8.8-55.7 R_J and 6.3-34.9 R_J and around 129°-174° and 94°-130° system III longitude respectively, consistent with e.g. *Louarn et al.* (2014). The mapped location of the second oval points lie within the edges of the mapped injection feature.

5.4.3 Auroral brightness

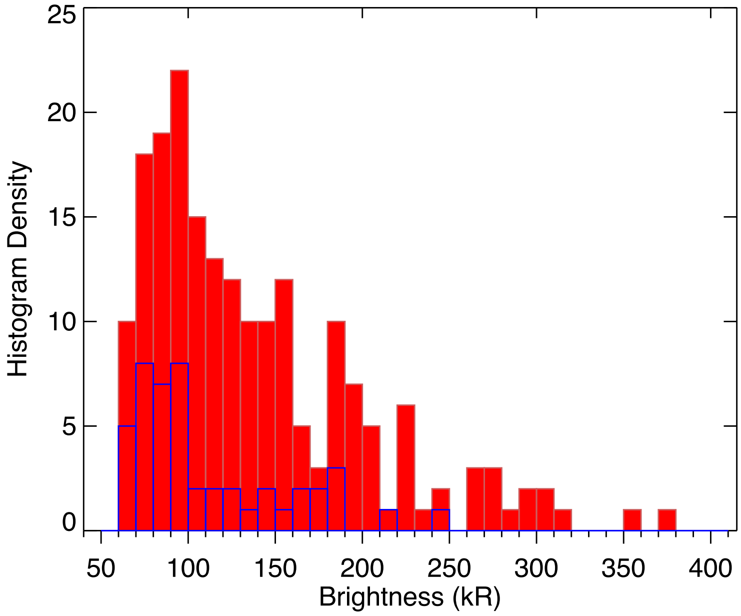

FIGURE 5.6: Histogram of brightness of second oval points for periods 3 days after an injection (red solid) and other days (blue outline).

Figure 5.6 shows a histogram of the brightness of the second oval feature through the 2014 campaign for the observations 3 days after injection events (red solid) and other observations (blue outline). A three day interval was chosen because the brightness increases for observations 3 days after injection events. The average brightness for all the second oval points is 133±62 kR. For points after injection events, the mean brightness is 139±65 kR; for other observations, the mean brightness is 112±44 kR. There are six observations before injection events and eight after. More second oval points are detected during 'post-injection' visits. There are over twice the number of points selected per bin around the modal brightness during 'post-injection' visits. There is a larger tail for the 'post-injection' visits, demonstrating that the second oval points selected are higher intensity.

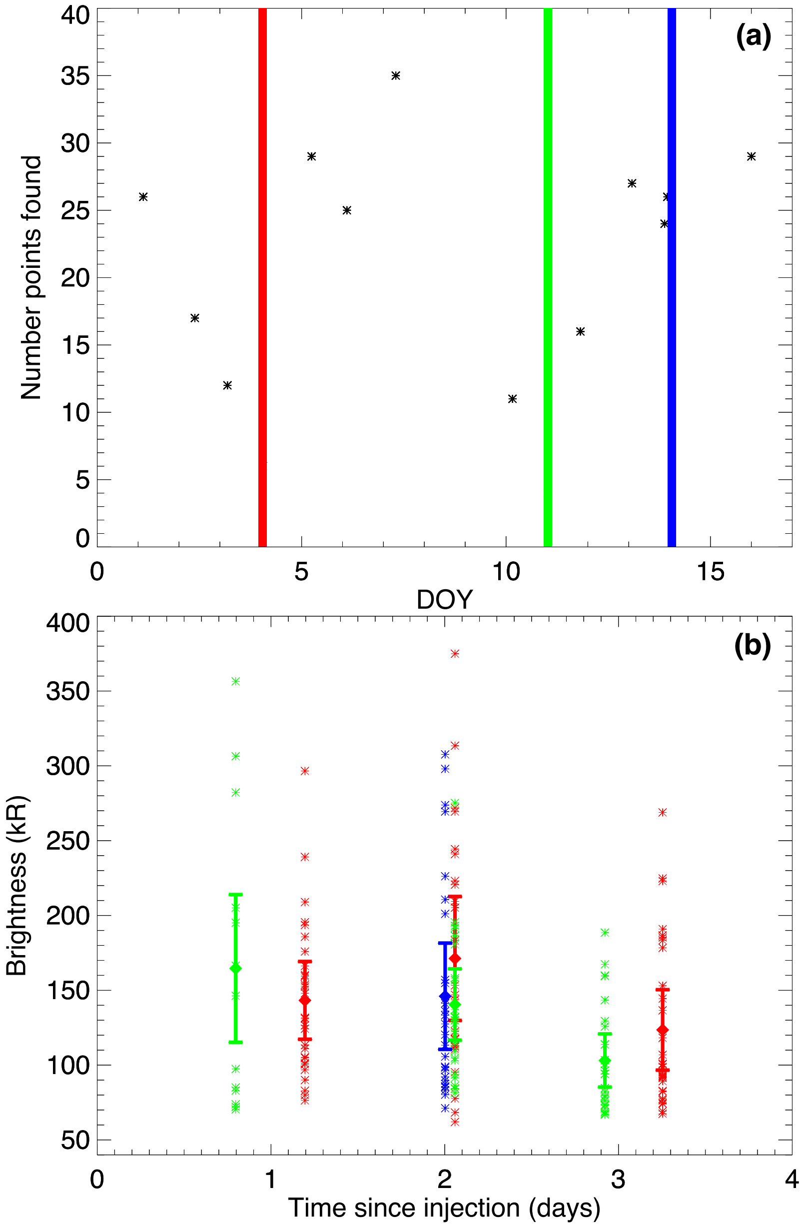

FIGURE 5.7: (a) Timeseries of the number of second oval points found in each observation normalised to the number of points that fit the detection critera. The coloured bars represent large injection events on day 4 (red), 11 (green), 14 (blue). (b) The brightness of second oval points detected after injection observations. The mean brightness and standard deviation are overplotted for each observation.

Figure 5.7a shows the number of second oval points detected normalised to correct for variable viewing geometry caused by the auroral region moving in and out of view as the planet rotates. There are more points detected after an injection event than before it, indicating that the second oval is more enhanced after an injection event. In response to the day 4 injection, the number of second oval points detected increases from 12 (out of a possible maximum across all images of 80) to 29 on day 5, a slight decrease to 25 on day 6 and up to 35 on day 7. For the case of the day 11 injection event, Figure 5.7a shows the increase in number of second oval points detected is from 11 on day 10 up to 27 on the last observation of day 13. For the day 14 injection event, the number increases further to 29. In general, then, there is an increase in the number of second oval points detected after injection events.

Superposed epoch analysis allows comparison of the responses of the second oval feature to injection events. The time of each injection event (taken as the first image where the events were detected for days 4 and 11, and with the HOM onset for day 14) is set to $t = 0$ days. Figure 5.7b shows the range of brightness of detected second oval points up to four days after the injection events.

It is noted that the mean brightness of the visits all lie within one standard deviation of each other. Following the first injection event, shown in red, the mean brightness of the detected second oval points begins at 143 kR on day 5, peaks at 171 kR on day 6 and falls to 123 kR on day 7. Despite the decrease in number of points detected on day 6 (Fig. 5.7a), the brightness of the points is higher than that of day 7. It is suggested that there are more points on day 7 because their intensity is just high enough to be detected and that in general their intensity is lower.

For the second injection event, shown in green, the mean brightness of the detected second oval points decreases through consecutive observations. The next observation is only 0.8 days after the injection event and the mean brightness of the second oval points is 164 kR. This falls to 140 kR on the first orbit of day 13 and to 103 kR at the end of day 13. The only observation after the third injection event (blue) has second oval points with a mean brightness of 146 kR.

The automated detection does not distinguish between small injections (e.g. day 11), second oval 'arcs' e.g. (days 5, 6, 7) and more complete second ovals (e.g. days 13, 16). More points are expected to be detected for a longitudinally spread signature, such as an arc, compared to a small localised injection signature. The points detected at 0.8 days (on Fig. 5.7b) correspond to the second observation of day 11 in which the HST images shows there are two small injections. This may explain why there is not such a large increase in the number of second oval points detected for this observation Fig. 5.7a, yet the peak brightness of the points is still high, at 356 kR, (Fig. 5.7b).

The two observations showing 'full' second oval morphologies on days 13 and 16 occur $\sim$ 2 days after large injections. Examination of Figure 5.7b shows that there does not appear to be a significant increase in brightness between the two observations despite the large injection event between them; day 13 shows points with a mean brightness of 140 kR (t$\sim$2 days, green) and for day 16 (t$\sim$2 days, blue) this is 146 kR. Figure 5.7a shows that a similar number of second oval points are detected on both images (days $\sim$12 and $\sim$16 respectively). This suggests that there is no cumulative effect of brightening due to two injection events occurring quickly after each other.

5.4.4 Temporal Evolution

The top panel of Fig 5.1 shows the development of second oval arcs from day 6 to day 7 in response to the injection event on day 4. The 150 kR brightness contour (pixels at greater than 150kR) of the right arc (Fig. 5.1b around 180° longitude) moves to higher longitudes (Fig. 1c around 190° longitude), which corresponds to a sub-corotating source. Both ends of the contour move 11°. The time between observations on day 6 and 7 is 28 hours. Assuming that these are the same feature and that all movement is in the subcorotation direction, this gives a drift rate of 0.4°/h (98% corotation). Sub-corotation was not explicitly seen in other sequences; however, this could be because the features were not bright enough to track.

The location of the main emission also changed through the campaign, possibly in response to the the injection events; *Badman et al.* (2016) explore the main emission and the link to radial plasma transport during this interval. In order to determine the inner boundary for second oval points detection, the average main emission is expanded sequentially to best fit the main emission points detected. This gives a measure of the main emission position per HST observation. Between day 6 and day 16, there is an expansion of $\sim$0.5°. This is in agreement with the findings of *Badman et al.* (2016), who reported the main emission expanded 1° over the full 2014 campaign (day 1 to day 16).

5.4.5 Spectral observations

The electron energy and electron flux may be different for the injection and second oval features. Spectral observations of a large injection signature are available on day 11 and of the second oval feature on day 16 of the campaign. Figure 5.8a and b show the location of the slit across the images for both days. On day 11, the slit passes through a large injection signature at low latitudes. On day 16, the slit passes through the dim main emission and second oval - the second oval appears as the lower latitude component.

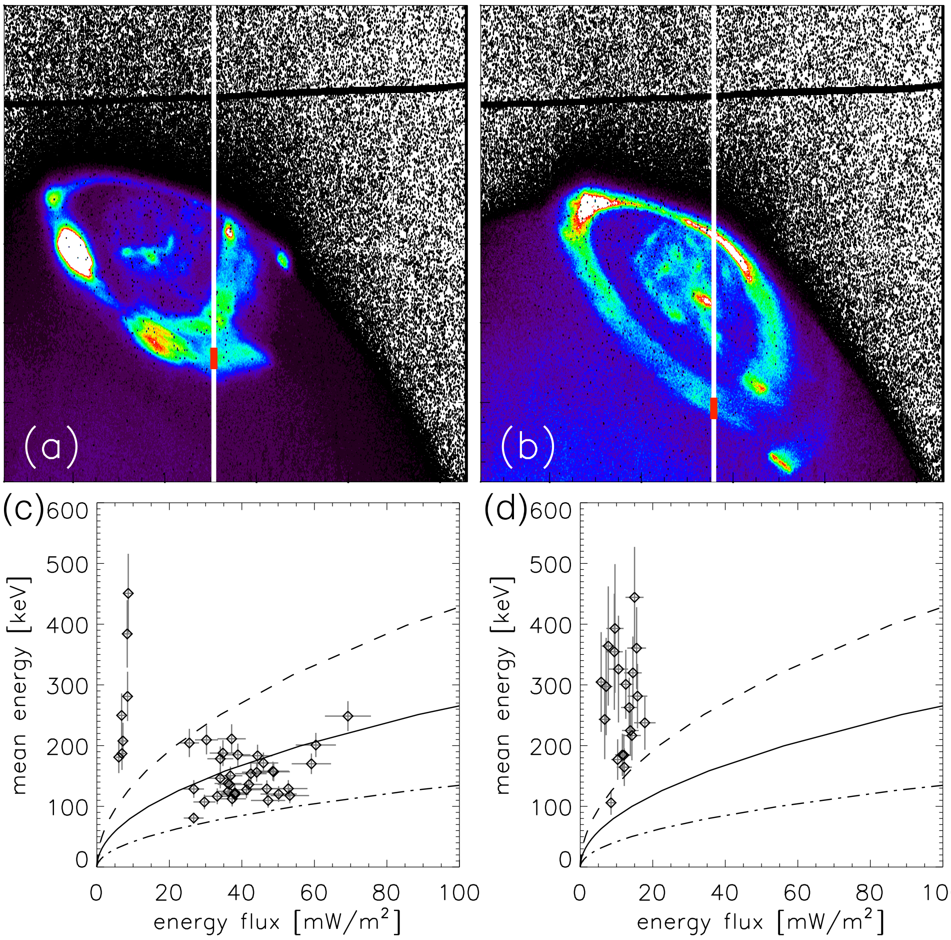

FIGURE 5.8: Top panel: HST unprojected images of (a) day 11, injection signatures, and (b) day 16, second oval, showing slit intersection (white) over the images taken before spectral observation; the red line indicates the low latitude region of interest. The low latitude region on day 11 is interpreted as a large injection signature. On day 16, the low latitude region contains the main emission and second oval feature - the lowest latitude portion could be the second oval. Bottom panel: Electron energy and energy flux for (c) day 11 and (d) day 16 for the low latitude points only. The expected relation between the mean energy and energy flux according to the Knight relation is shown for different source populations, $N_0 = 0.0026$/cc (solid), $N_0 = 0.001$/cc (dashed), $N_0 = 0.01$/cc (dot dashed). The main emission is expected to obey the relation described by these lines (*Gustin et al.*, 2016)

Figure 5.8c and d show the energy flux-precipitating energy relationship for the 'low latitude' feature spectral slit observations of days 11 and 16. The points corresponding to the large injection signature (5.8a, c) have a lower precipitating energy and higher energy flux than the low latitude points from day 16 (5.8b, d). The second oval feature may have more higher energy precipitating electrons than the large injection signature. The lines represent the energy and energy flux relation for different density electron sources being driven by field-aligned currents (i.e. the Knight relation). This may imply that the large injection signature is generated by field aligned currents at its edges due to pressure gradients (e.g. the 'bubble mode' (*Nakamura et al.*, 2001)), as well as some scattered electrons at high energy and low energy flux. The second oval signature could be formed by scattered electrons at a range of energies and low energy flux.

5.5 Possible generation mechanism: Wave-Particle Interactions

We will consider both whistler mode waves and shear Alfvén waves as candidate waves for scattering or accelerating electons into the loss cone to form the second oval feature. Generation of a longitudinally spread auroral signature requires scattered electrons from a longitudinally extended region so it is expected that precipitating electrons have drifted around the planet. Based on the enhancement of the second oval identified from Fig.5.7 following injection signatures, we now consider the possible effect of a localised injection in the region 7-20 R_J. Injected electrons are expected to drift opposite to the co-rotation direction as a result of the gradient and curvature of the magnetic field and disperse according to their energy (*Mauk et al.*, 2002). A dipole magnetic field is assumed. For electrons, the drift velocity can be approximated as (*Mauk et al.*, 1999):

$$\omega = 6.92 \times 10^{-7} \frac{q_0}{q} TLH \tag{5.1}$$

where $H = 0.7 + 0.3 \sin \alpha$, a numerically solved correction factor to the drift velocity, $T = E \frac{E+2E_{0m}}{E+E_{0m}}$, the electron temperature, ω is the drift velocity of the electrons in rad/s, q is the charge, q_0 is the proton charge, L is the l-shell number, α is the equatorial pitch angle in radians, E_{0m} is the rest mass and E is the energy in MeV. *Mauk et al.* (1997); *Mauk et al.* (1999) report typical electron energies in the range ~10-1000 keV observed in this region using EPD measurements from Galileo. Over this energy range, between L=10-20 with equatorial pitch angles between 10-90°, equation 5.1 yields the range of

4-705 days (with higher energy electrons at larger pitch angles and at further L-shells taking a shorter time) to spread 360° in longitude; this corresponds to a drift rate of 0.02-3.82°/h. This corresponds to a 89%-99% corotation rate, which encompasses the rate found from the HST images.

Plasma wave growth may occur as a result of the temperature anisotropy across the injection. *Katoh et al.* (2011) have shown that at Jupiter, whistler mode chorus enhancements may be efficiently generated by energetic electron populations. Waves have been reported in the region of interest (e.g. *Radioti et al.* (2009); *Tomás et al.* (2004a,b); *Menietti et al.* (2016)). Although studies at Earth have shown wave growth is expected to be rapid (few hours. e.g. *Thorne et al.* (2010)), waves are not typically seen in all locations at all times since the growth process may be throttled by the surrounding cold plasma conditions, such as its density (*Li et al.*, 2009a,b). The efficiency of the wave-particle scattering mechanism is affected by many parameters including the particle energy, wave frequency and the cold plasma density (e.g. *Glauert and Horne* (2005)). The range of electron energies from the injections in this region typically interact strongly with the frequency of chorus waves observed here (*Woodfield et al.*, 2014).

Should good wave growth and resonance conditions be achieved, the electron is expected to be scattered into the loss cone. There may be multiple injections, or multiple parts of the same injection with different dominant energies. The auroral feature may therefore appear patchy and in discontinous arcs. This process has been reported at Earth, e.g. *Thorne et al.* (2010); *Ni et al.* (2011); *Tao et al.* (2011), where injected plasma sheet electrons have been seen to enhance the diffuse auroral oval via pitch angle scattering due to chorus waves.

Shear Alfvén waves, which accelerate electrons through generated parallel electric fields, may also be responsible for the auroral precipitation observed. Parallel propagating Alfvén wave generation is expected where there is a change in magnetic topology, for example at reconnection events (*Shay et al.*, 2011) and the boundary of hot plasma injections. Magnetospheric shear Alfvén waves have been observed to contribute to the generation of aurora at Earth, particularly along field lines associated with the plasma sheet boundary layer (*Wygant et al.*, 2000; *Watt and Rankin*, 2010, 2012).

The auroral signatures of shear Alfvén wave driven electron precipitation tends to be latitudinally constrained since they accelerate electrons parallel to the field lines upon which they act. The field lines can map to a large region in the magnetosphere. It's feasible, therefore, that this process could be responsible for the latitudinally constrained signature reported here. Additionally, the spectra associated with the second oval may show high mean energy electrons, as expected for Alfvén waves.

5.6 Interpretation and Discussion

Arcs of emisson equatorwards of the main emission have been detected in Jupiter's aurora. Figure 5.7a shows that this feature is brighter across more longitudes after large injections. The second oval feature can appear in arcs (see HST images from day 4-7 on Fig 5.1a), which extend to higher longitudes with time, as expected for a source that is sub-corotating. The rate of sub-corotation for the second oval estimated from the HST images (0.4°/h) is in agreement with the theoretical drift rate calculated for electrons with energy around 400-800 keV at L-shells of 10-20 at equatorial pitch angle 60°.

Magnetic mapping of the injection signatures from HST images on day 11 and of the average position of the second emission show that the sources of these two features overlap in the equatorial plane. Figure 5.5c shows the mapped position of the second oval feature lies around ∼9-13 R_J, where the field lines are roughly dipolar. The second oval lies close to the Ganymede footprint contour. The location found here is close to that found in previous work (*Tomás et al.*, 2004b). The second oval location found in this work and previous work are in agreement with a source around 10-17 R_J, where the PAD boundary is thought to lie. The location of the second oval feature, its increased brightness 1-3 days following injections and apparent sub-corotation suggests that the auroral second oval feature can be enhanced as a result of an evolution of the injected plasma. Injected plasma has a latitudinally broad signature, but particles which have drifted longitudinally may be scattered by waves, so produce a longitudinally spread but latitudinally confined signature.

Spectral studies of auroral signatures allow the energies and fluxes of precipitating electrons to be determined. Figure 5.8 compares the injected plasma and second oval feature and shows that the second oval feature tends to be formed by higher energy electrons with lower fluxes than the injected plasma signature. It is suggested that the electrons may have been energized and scattered as part of wave-particle interactions for both the initial injection signatures and the second oval feature. *Tomás et al.* (2004b) predicted that for electrons in the two EPD energy channels 55-188 and 55-304 keV, the precipitating flux may be 36-115 kR to 59-276 kR respectively. This is in agreement with the range of brightnesses found for second oval points in Fig. 5.6. Figure 5.8d shows the mean electron energy for the scattered electrons forming the second oval may extend up to ∼500 keV; more energetic electrons may drive brighter aurora (up to a few hundred keV, above which UV absorption by hydrocarbons at lower altitudes throttles the auroral brightness, (*Tao et al.*, 2011)). The higher energy electrons could therefore account for the higher end tail of the brightness distribution of the feature, as shown in Fig. 5.6.

Figure 5.4 compares second oval points detected in arcs on day 6 and the more 'full' morphology seen on day 16 and shows that the arcs may be visible parts of the more complete oval feature. Wave growth and resonance processes are affected by cold plasma conditions and therefore do not necessarily occur at equal rates at all local times. Brighter arcs could be generated by wave-particle excitation processes where the cold plasma density surrounding the initial injected plasma is appropriate for wave growth and resonance. Figure 5.7b shows superposed epoch analysis of the second oval brightness. The brightness tends to increase between 1-2 days after the injection event and fades thereafter. This suggests wave growth and resonance processes that scatter electrons into the ionosphere can be a long-lived (at least 3 days) process at Jupiter.

Three large injections of hot plasma are observed in this campaign in quick succession. Figure 5.7a shows that there is a slightly higher number of second oval points detected on day 16 after the day 14 injection event, showing that the feature spreads to more longitudes. Figure 5.7b shows that the peak brightness of the feature increases by ∼100 kR after the day 14 injection event. The mean brightness remains constant. It is suggested that wave-particle interactions are sustained by the successive large injections.

Previous work has suggested that the second oval is the auroral counterpart of a stepdown in plasma angular velocity mapping to the main oval (*Hill*, 2001; *Cowley and Bunce*, 2001; *Vogt et al.*, 2011). It is noted this is not reflected in empirical models of co-rotation breakdown (*Grodent et al.*, 2003). Enhancements of the second oval as studied here would be related to a step in co-rotation breakdown closer to the planet, but not an inward shift of the main emission source (since its auroral signatures remains). However, Fig. 5.8c and d show the mean energy vs energy flux relation for the second oval is different to the main emission curves (which obey the Knight relation) shown by (*Gustin et al.*, 2016).

5.7 Summary

We have identified a UV auroral arc feature of varying longitudinal extent equatorward of the main emission. The location of the second oval feature lies between the Ganymede and Europa moon footprint contours between 150°-240° system III longitude, corresponding to a source in the inner magnetosphere between ∼9-13 R_J. This is in the same region of 10-17 R_J known as the PAD boundary, where electrons have been observed to be scattered into a field-aligned configuration and cause auroral precipitation. The feature is enhanced in both brightness and longitudinal spread 1-3 days after large injections signatures. Spectral analysis of the H_2 emissions shows the precipitating electrons have a higher energy and lower flux than the electrons generating large injection signatures.

We suggest that wave-particle interactions are responsible for the scattering of electrons in this region. We also suggest that the plasma injections can act as a temperature anisotropy and particle source to enhance wave intensity and subsequent electron scattering into the ionosphere. We suggest this process can last up to at least 3 days. Changes to the magnetic field topology around an injection may also generate shear Alfvén waves and therefore accelerate electrons parallel to the magnetic field resulting in precipitation. The second oval therefore may be and indicator of the second step in energy dissipation of injected plasma.

Chapter 6

UV High Latitude Response to Solar Wind Compressions

6.1 Introduction

This chapter examines the auroral morphology associated with co-rotating interaction regions (CIRs). The chapter introduces CIRs and the current understanding of the high latitude and main emission features in response to compressions. It then shows New Horizons, HST and mSWiM data from a CIR impact period in February and March 2007 and highlights the UV response. A short statistical survey looks at the high latitude behaviour in the UV and compares it to that of X-Rays. The observations are discussed and interpreted, particularly in terms of the periodicity of features and the main emission morphological changes.

6.2 Theory

The UV polar emission is expected to vary the most under solar wind influence since its field lines connect to the outer magnetosphere and where an open field region may exist. *Bonfond et al.* (2017a) recently reported on the recent JUNO UVS results; they found a region in a 'mussel' shape of higher colour ratio (normally attributed to higher energy precipitating electrons) in the polar region. They noted that the abrupt boundary showed UV emission around its dayside edge and resembled the shape of the open field region predicted by the flux-equivalent magnetic field mapping model of *Vogt et al.* (2011, 2015).

Emission at high latitudes has previously been reported in the northern and southern hemisphere (*Waite et al.*, 2001; *Pallier and Prangé*, 2004), sometimes with a quasi-periodic pulsation (*Bonfond et al.*, 2011; *Bonfond et al.*, 2016); these forms may be the signature of the Jovian polar cusp. The pulsating features tend to be found towards the dusk side (as viewed from HST) and sometimes take the form of spots or of very large emission extents covering the whole active region. These have been found to pulse with a 2-3 minute timescale in phase in both hemispheres, suggesting the two hemispheres are related (*Bonfond et al.*, 2016). The large spatial scale of the emission is surprising; simultaneous flashing at this scale requires extremely fast communication along multiple field lines. The authors therefore postulated that there is some level of ionospheric control of the signatures extent. Further, *Bonfond et al.* (2017a) found that the flashes bound the 'swirl' region at high latitudes, indicating that the aurora may be generated by a process related to a magnetospheric boundary.

This region of the aurora was also studied by *Nichols et al.* (2017a). They focused on the response of the UV aurora through three compression periods separated by rarefaction regions using HST during the Jun approach phase. Solar wind parameters during this interval were well constrained by Juno. They observed that the region poleward of the main emission showed multiple arcs parallel to the main emission and patches. During the compression, the emission was enhanced and sometimes bursty or periodic. They showed that a region poleward of the main emission on the 'dusk side' (as viewed by HST), which they named the 'Noon active region' (NAR), showed emission in the compression and rarefaction periods. Emission during rarefaction periods was unstructured or formed arcs poleward of the main emission. Emission in compression periods was seen as an extent of the 'dusk active region' (DAR), associated with compression-triggered tail reconnection and is discussed more below.

The model of reconnection at the cusp by *Bunce et al.* (2004) predicts a field-aligned system at the cusp into the ionosphere. A current of particles along reconnected field lines at the cusp drive a current into the ionosphere across a 'merging gap' (which is the ionospheric footprint of the reconnection site). The 'upwards' current is carried by downward electrons; the 'down' current corresponds to positive ions (producing Doppler-shifted H Lyman-alpha emission). The strongest UV emission is expected in the upward current region. The model has been applied at Saturn with some success (*Bunce et al.*, 2005). At Saturn, auroral cusp spots poleward of the main emission (the open/closed field line boundary) have been attributed to reconnection on the dayside during compressed (*Jackman et al.*, 2004; *Gérard et al.*, 2005; *Badman et al.*, 2013) and rarefied conditions (*Kinrade et al.*, 2017) either at the lobe or at low-latitude. The IMF strength and direction may modulate reconnection and open flux production at the magnetopause. It is possible to estimate the prevalent IMF direction (e.g. *Jackman et al.* (2004)) if the planetary tilt, position in solar cycle and Sun-planet position is taken into account.

Reconnection triggered by magnetotail compression may result in the so-called DAR flashes (*Nichols et al.*, 2017a), nightside and polar dawn spot signatures as part of return flows (*Grodent et al.*, 2004; *Radioti et al.*, 2008a). During compression regions, the NAR was seen to be active, though the authors interpreted this as an extension of the dusk auroral emission reconnection signature, perhaps relating it to Vasyliunas/Dungey cycle processes as opposed to a direct signature of compression. Furthermore, work by *Kita et al.* (2016) has suggested some priming of the Jovian system whereby it fills with Iogenic plasma before large auroral storms associated with solar wind dynamic pressure increases.

The main emission responds to solar wind conditions too. The work of *Nichols et al.* (2017a) also confirmed that the 'well defined main emission (that is, the main emission at SIII longitudes > 180°) brightens at compression region onset. Recent global MHD modelling efforts by *Chané et al.* (2017) show that the main emission could brighten under magnetospheric compression when the ram pressure (solar wind density and velocity) increases. The authors show that in response to the magnetic field dawn-dusk asymmetries (the magnetic field 'bend back') being enhanced as the field lines are compressed at the dayside and elongated at the nightside, the main emission could also exhibit dawn-dusk asymmetries. They showed the nightside main emission is expected to brighten, the dayside to dim for a few hours then brighten and the local noon emission may broaden.

In addition, (*Cowley and Bunce*, 2003) suggests that due to compression the middle magnetospheric plasma responsible for the main emission at Jupiter may speed up rotation. A stepwise break in co-rotation breakdown has been suggested from studies of the infrared main oval parallel branches of the main emission (e.g. *Stallard et al.* (2001)), which shows several (see, for example, Figure 4 of *Mura et al.* (2017)), with the UV normally lying on the outermost one. This is observational and not supported by smooth angular velocity profiles predicted by theory/modeling, for example, *Hill* (2001) and *Nichols and Cowley* (2003).

X-Rays at Jupiter tend to coincide with either the main emission or the polar region. The main emission 'hard' X-Rays (greater than 10 keV) are thought to be driven by Bremsstrahlung, whereas the polar region is dominated by 'soft' X-Rays (0.2-2 keV) thought to be driven by ion precipitation. The Chandra and XMM-Newton observatories have shown that the polar region has a hotspot that is often populated (e.g. (*Kimura et al.*, 2016)). This is true for the Northern and Southern Hemisphere (*Branduardi-Raymont et al.*, 2008). There is often no emission in the hotspot region followed by periodic pulsating emission, indicating the X-Ray emission in the hotspot region may be triggered solar wind conditions.

Dunn et al. (2016) showed that under solar wind compression (as part of a Coronal Mass Ejection outflow reaching Jupiter) the X-Ray 'hotspot' expands. *Kimura et al.* (2016) showed there is a positive correlation of counts with solar wind velocity but not with pressure and that the emissions map from noon down the dusk flank of the magnetosphere close to the magnetopause using *Vogt et al.* (2011, 2015) models.

Although the intensity of X-Ray population is not always periodic, the X-Ray hot spot has been seen to pulsate with multiple periods depending on the ion species. A period of 40-45 minutes has been reported from X-Ray hotspot observations (e.g. from precipitating oxygen (*Gladstone et al.*, 2002)) and it has been suggested that following analogy with the terrestrial Flux Transfer Event (FTE) this could be related to an Alfvén travel time between the magnetosphere and ionosphere (e.g. (*Bunce et al.*, 2004)). Other studies have not found a 45 minute periodicity in the X-Ray data but have found other close periodicities (e.g. (*Elsner et al.*, 2005)). The recent work by *Dunn et al.* (2016) examined the response of the X-Ray aurora to an ICME strike over two observations - at the arrival and during recovery. They found as the ICME arrived, a period in the carbon/-sulphur (these cannot be distinguished by Chandra) and oxygen emissions of 12 minutes and a strong 26 minute periodicity of carbon/sulphur in the hotspot. During their observation of the emission recovery period, they found a 42 minute periodicity, which is close to that reported by *Gladstone et al.* (2002), suggested by *Bunce et al.* (2004) and found in QP-40 radio data (e.g. (*Karanikola et al.*, 2004; *Kimura et al.*, 2011)) and in electron bursts detected by e.g. Ulysses ((*McKibben et al.*, 1993)). The previous works mentioned above all suggest a source further than 30 R_J for the precipitating particles and variability with solar wind. In particular, *Dunn et al.* (2016) suggests that there is a significant solar wind driver for the X-Ray emissions.

Although one may initially expect the common magnetospheric drivers to produce the same periodicity in both UV and X-Ray observations, the UV has notably shorter associated periodicities, in particular 2-3 minutes (*Bonfond et al.*, 2011). This was also seen in the electron bursts of *McKibben et al.* (1993), magnetopause magnetic signatures of *Walker and Russell* (1985) and radio (*Hospodarsky et al.*, 2004). The 45 minute periodicity in the X-Ray, electron bursts and radio measurements may lead one to expect to find the same periodicity in the UV observations. Given the HST orbits in previous campaigns have only been 40 minutes long, it is not possible to test for this periodicity currently. It is hoped with the long term ($\sim$ few hours) orbits of Juno that this periodicity may be tested for.

6.3 Auroral response to solar wind CIRs in February and March 2007

In February 2007 the New Horizons spacecraft flew past Jupiter en route to Pluto, and measured the plasma conditions upstream and in the magnetotail. Unfortunately, New Horizons did not carry a magnetometer, however, the plasma data suggest that HST UV and Chandra X-Ray observations taken in March and February in 2007 coincide with the arrival of two Co-rotating Interaction Regions (CIR). Structured arrival of compression and rarefaction regions are expected to reoccur at the Jovian magnetosphere as the CIR rotates around the Sun.

In this interval, the effect of two CIRs are seen roughly 10 days apart. Figure 6.1 shows the solar wind velocity, number density and IMF strength. Two rotations of the CIRs are shown and the observation interval is shown with blue labels. These are found by shifting a solar wind propagation model (mSWiM, (*Zieger and Hansen*, 2008)) 2.1 days to match New Horizons data after *Nichols et al.* (2009a); *Clarke et al.* (2009). They grey window represents a 40 hour window of uncertainty of the mSWiM model. Despite the propagation to match New Horizons data, it is still sensible to include this uncertainty window. HST observations are taken around days of year 53-57 and 63-69. The auroral response to compression has been previously studied (e.g. *Clarke et al.* (2009); *Nichols et al.* (2007, 2009a); *Nichols et al.* (2017a); a brightening of the main emission at longitudes $> 180°$ and patchy or bursty main emission at longitudes less than this. Anticipating this response, in this study we match the solar wind velocity and number density peaks to the beginning of this auroral response. We use the auroral UV from the Hubble Space Telescope (HST) emissions as a way of investigating planetary

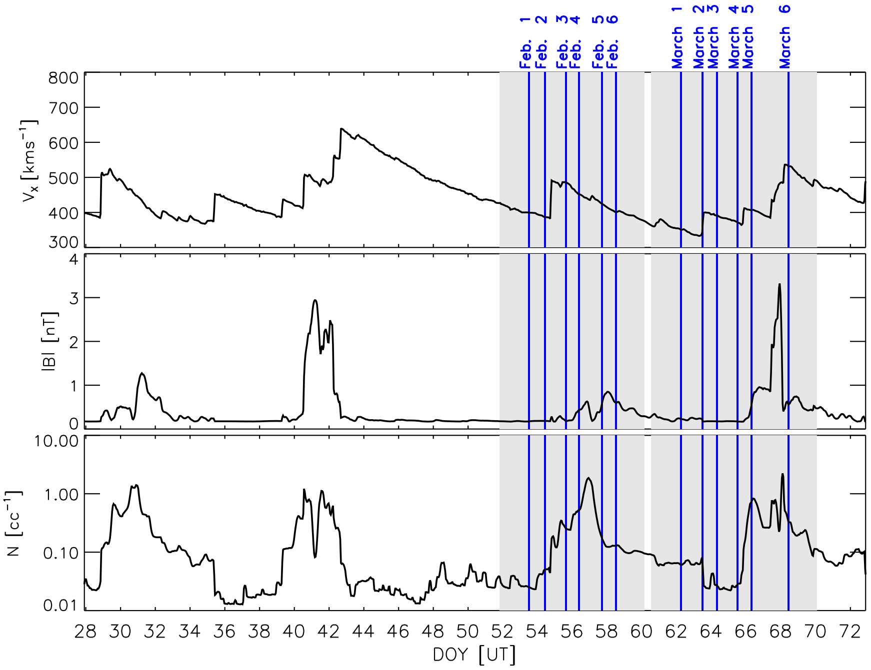

FIGURE 6.1: Solar wind velocity(top), IMF strength (middle) and solar wind density (bottom) over the period of interest in 2007 measured using a propagated mSWiM model to match New Horizons data. These are found by shifting a solar wind propagation model (mSWiM) by 2.1 days to match New Horizons data after *Nichols et al.* (2009a); *Clarke et al.* (2009). Labels in blue show the times of the HST observations in Feburary and March, with uncertainty window of ± 40 h.

response to the CIR impact interval in February, days 54-57, because it is the best-constrained shock arrival time. We also focus on day 63 of the March interval that shows an interesting pulsating spot feature.

Figure 6.2 shows the auroral response over 6 HST visits for both the February and March events.

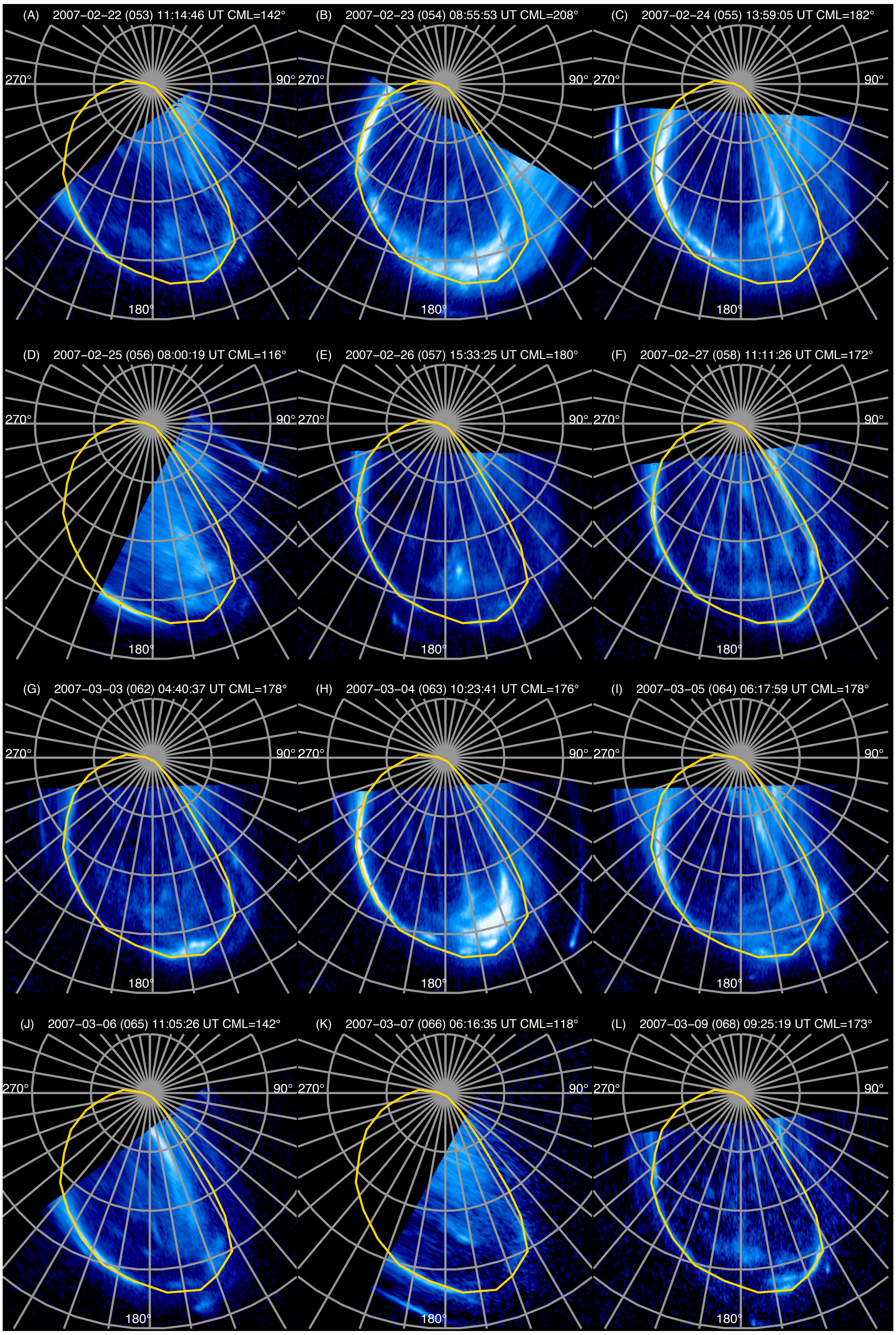

FIGURE 6.2: Twelve panels showing polar-projected HST image of Jupiter's northern FUV aurora over the CIR impact during February (panels A-F) and March (panels G-L). For each image the exposure time was between 30 and 100 s. The Central Meridian Longitude (CML) is shown. The image is displayed with a log intensity scale saturated at 1000 kR. The grey lines indicate a 10° 10°jovicentric latitude-system III longitude grid. The image is oriented such that 180° λ_{III} is directed toward the bottom and $lambda_{III}$ labels are displayed in white.

The following discussion compares the two events to identify the common features seen in each part of the response. It is split in the high latitude and the main emission responses.

Before each compression interval fully impacts, both sets of images show typical rarefaction responses (panels A and G) i.e. the main emission is relatively dim globally, especially around noon, with the exception of brightness post-noon; this is a typical state of the main emission (e.g.*Nichols et al.* (2017a); *Radioti et al.* (2008a)). In the February event there is some polar cusp spot activity, but this is absent in the March event.

In response to the compression (likely within a day but this is uncertain due to the uncertainty in the solar wind data Fig.6.1), as shown in panels B and H, the main emission has intensified especially around dawn in both images, as described for the 'well defined main emission' in *Nichols et al.* (2017a). The main emission has also shifted poleward about a degree in both images. There are localised effects too: the emission has become particularly bright and expanded poleward locally around 160-180°, with both sets of images showing arc structure developing. There is polar activity in both visits; the February event shows bright and localised emission at 175° longitude and 64° latitude; this emission is larger that most cusp spot emissions and lies along the main emission arcs. The March event also shows bright and localised emission around 180° longitude and 64° latitude away from the arcs; this emission is very typical of cusp spot emission(e.g. *Prangé et al.* (2004)). The February event also shows polar dawn spots previously discussed in (e.g. *Radioti et al.* (2008a)).

As the compression continues in panels C and I the arcs in the main emission continues post-noon. In the February event there is a discontinuity in the main emission at noon, around 170-180° longitude. In the March event there are polar dawn spots visible. Both of these are potential signatures of return flows from tail reconnection. Both images also show flashes in this region with a 2-3 minute periodicity (see Fig 6.5). There is also increased low-latitude emission.

As the compression passes in panels D and J, the main emission dims around noon and the arcs consolidate to thick emission on the dusk and dawn sides. The flashing continues in both events at high latitudes. In the March event a poleward dusk arc flashes, which may be the signature of tail reconnection.

In panels E and K the main emission has begun expanding to its original position, has returned just past noon (with missing emission pre-noon and dusk), is well defined and is still dimmer than its nominal brightness. There is now only low level activity in the polar region. In the February event a strong second oval appears from the edge of the image to around 165°.

In the final panels of the events, F and J, the typical rarefaction morphology is visible. The main emission continues to increase in brightness and is well defined. As the visit proceeds, a section of the emission in the dusk sector retreats about a degree to fit along the 'oval' of the rest of the emission. In the first visit of the March event, there is strong partial second arc at about 165°; in the second visit 60 minutes later the main emission is bright but a single arc in this region.

The responses of the aurora to the CIR are summaried in table 6.1.

TABLE 6.1: A table summary of the Mid-Low latitude and high latitude of the Jovian UV aurora to a CIR event, with indicated time markers for Onset, Magnetospheric Expansion and Solar Wind Rarefaction. Many of these responses have been noted previously by (*Clarke et al.*, 2009; *Nichols et al.*, 2007, 2009a; *Nichols et al.*, 2017a). There is some overlap so some panels are referenced twice.

Phase of CIR	Mid-Low latitude features	High latitude features
1: Event Onset (A and G, H)	Well defined main emission at dawn Enhanced, thicker emission at dusk Contraction polewards	High latitude spots; some cusp spots
2: (B and H, I)	Branching of main emission into parallel arcs at dusk Enhanced with bursty emission	Bursty dusk emission High latitude dusk arc emission as tail reconnection signature
3: (C and I)	Continued: Branching of main emission into parallel arcs at dusk Enhanced with bursty emission Patchy low latitude emission	Continued: Bursty dusk emission High latitude dusk arc emission as tail reconnection signature
4: (D and J)	Dimming and consolidation of emission at dusk at dawn	Continued: Bursty dusk emission
5: Magnetosphere Expands (E and K)	Gradual brightening, thinning and expansion of main emission from poleward arcs to fit with main oval structure - occurs last at dusk Well defined low latitude emission	Normal polar activity
6: Solar Wind Rarefaction (F and L)	Well defined main emission	Normal polar activity

It is suggested that the compression impacted either just before or at the start of the image sequence on February 21^{st} (day 52); however, it is impossible to tell outside of uncertainty from either the New Horizons or shifted m-SWiM data that this is the case.

6.4 Analysis

Figure 6.3 shows significant enhancements in the dusk side main emission and poleward region on days 54 and 55. There are two flashes on day 54, four on day 55 and one on 56. The day 56 sequence is taken at an extreme CML, so it is hard to be certain about the extent or periodicity of flashing for this reason, this day is not analysed in detail but a continued response is noted.

By subtracting the previous image from the image showing enhancement, the region of enhancement was isolated. Only enhancement greater than 100 kR is shown to avoid variations in noise being shown. The enhancement is overlaid in pink on the enhanced image on panels (C) and (F) of Fig 6.3. This shows the majority of enhancement comes down the main emission arcs/bifurcation structures, for example in panel (F), though there is also emission between these structures. There is also patchy enhancement at other points along the main emission through the dawn side.

Between the first and last exposures of the images taken on each day, the main emission generally brightens, aside from the local noon emission, which does not brighten. Both days show a widened main emission on the dawn side (as viewed by HST). On other images in this interval, tail reconnection signatures such as the DAR signature suggested by *Nichols et al.* (2017a) and polar dawn spots (*Radioti et al.*, 2008a) are seen.

6.4.1 High latitude response

Figure 6.4 shows an example of pulsating spot behaviour on day 63 (during the March CIR arrival interval) at around 173° longitude and 63° latitude. In Fig 6.4a, the spot is visible, 6.4b it is not as bright and in 6.4c shows stretching into a poleward form. These are distinct from previously reported polar auroral filaments (*Nichols et al.*, 2009b).

Using the differencing technique shown in Fig. 6.3, the power in the flashing region on day 64 can be isolated. Similarly, the pulsating spot on day 63 can also be isolated. A box capturing the 100kR contour of the most common flashing region shows the region where the enhancement occurs. Figure 6.5 shows the power time series in the pulsating

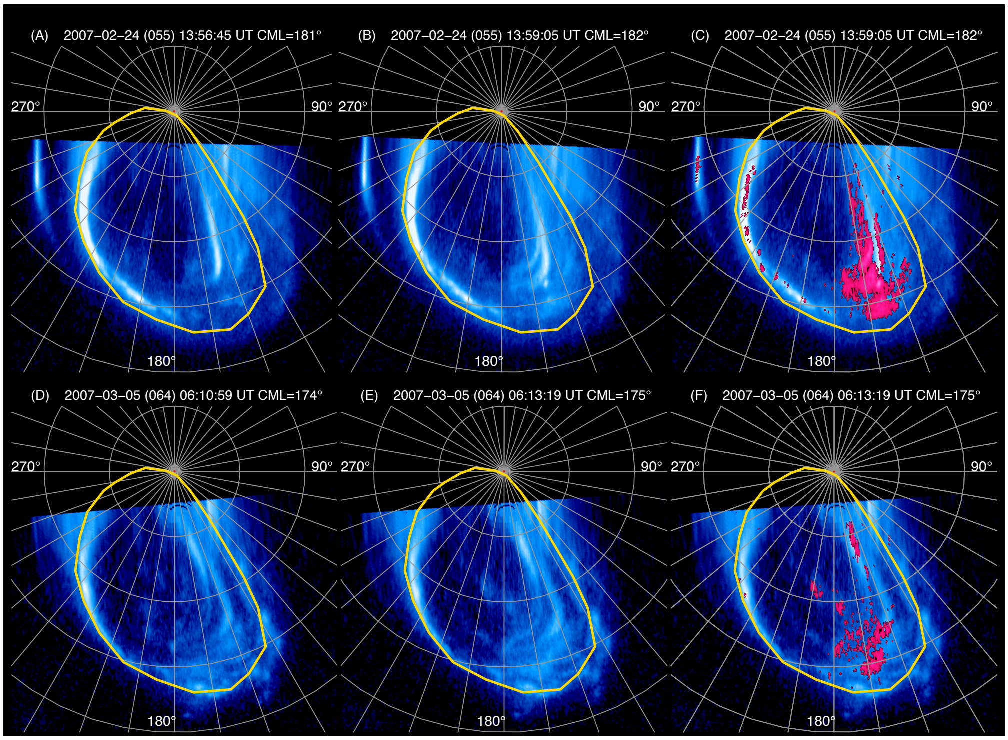

FIGURE 6.3: Six polar projected images taken with the HST, with log intensity scale saturated at 1000 kR. The gray lines indicate a 10° 10° jovicentric latitude system III longitude grid. The image is oriented such that 180° system III longitude is directed toward the bottom and labels are displayed in gray. (Top panel) Day 55 images (A) before and (B) during enhancement and (C) showing the difference between the files (pink) superimposed on the enhanced image (Bottom panel) Day 64 images (D) before and (E) during enhancement and (F) showing the difference between the files (pink) superimposed on the enhanced image.

spot region on day 63 (red) and the large flashing region on day 64 (black). These have a similar 2-3 minute periodicity.

6.4.2 Local time dependence of pulsating features

Individual and statistical studies of the high latitude aurora in the X-Ray (emission due to ions) have shown that there is a hotspot for polar emissions (e.g. (*Dunn et al.*, 2016; *Kimura et al.*, 2016)). Magnetic mapping of these emissions into the equatorial plane suggest that there is preference to a duskward source or driver (see Fig. 6 of *Kimura et al.* (2016)).

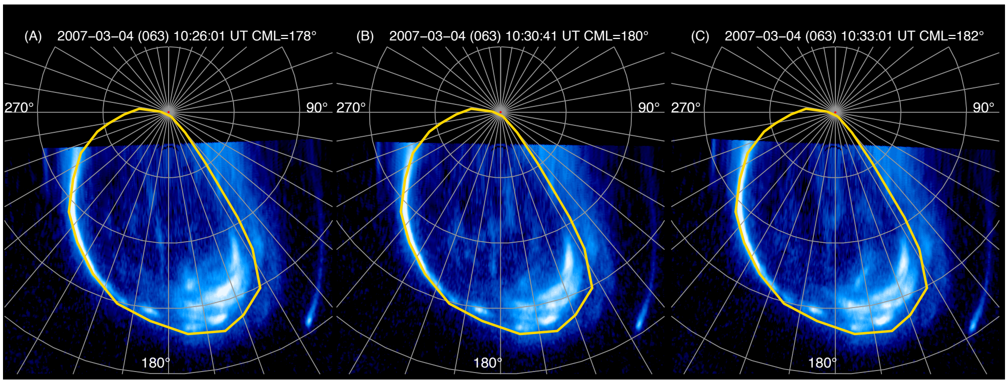

FIGURE 6.4: Three polar projected images taken with the HST on day 63 showing the pulsating spot, with log intensity scale saturated at 1000 kR. The gray lines indicate a 10° 10° jovicentric latitude system III longitude grid. The image is oriented such that 180° system III longitude is directed toward the bottom and labels are displayed in gray. The spot is in (a) enhanced (10:26 UT) at around 172° longitude and 64° latitude, (b) faded (10:31 UT) and (c elongated polewards (10:33 UT)

The following seeks to ascertain whether the same local time preference exists in the UV in order to examine a link between polar UV and X-Ray processes. The footpoints of aurora identified in the high latitude region (as identified below and in Fig.6) were mapped into the equatorial plane to find their source/driver region. The internal field model VIPAL was used in conjunction with the flux equivalence method of *Vogt et al.* (2011, 2015).

Hubble Space Telescope images from the 2014 campaign were polar projected and the same areas outlined by *Kimura et al.* (2016) were outlined on these images to identify a 'halo' and 'core' region. During this period, there was no large compression - the images were taken in a relatively quiet solar wind period (see figure 2e of (*Badman et al.*, 2016)). Despite this, the campaign includes images showing flare activity dominating the high latitude region in large coherent structures (in 2014 on days 7 and 10, see grey background of figure 6 and figures 1g and 1h of *Badman et al.* (2016) for further examples).

Figure 6.6 shows a projected image of an event in 2014 with the regions of interest coloured. The core and halo regions were picked out as circles in accordance with *Kimura et al.* (2016); they are similar but not identical to the traditionally isolated 'active' and 'swirl' regions. The main emission was then excluded from these regions by removing the region one-degree poleward of the average position of the main emission from 2014. A region at high latitudes on the dusk side where the image is often distorted was

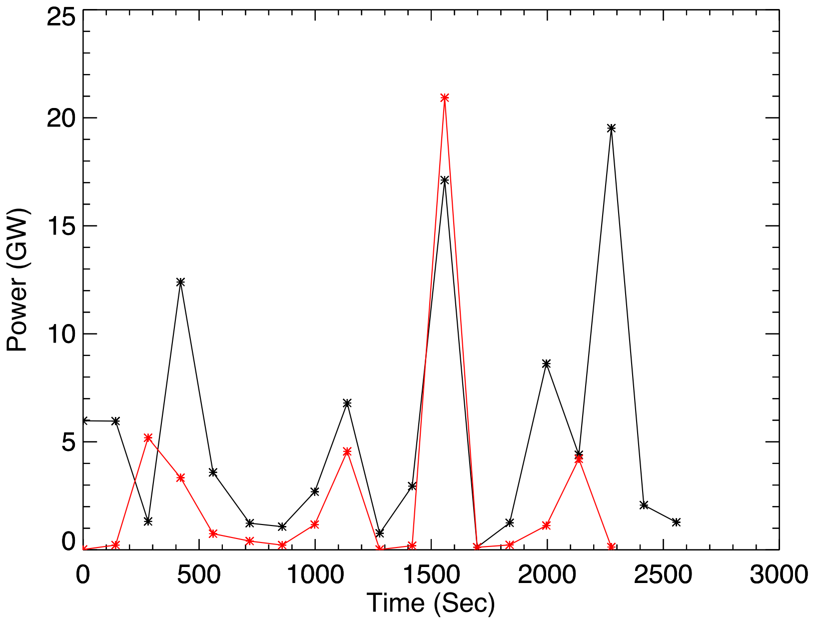

Figure 6.5: A timeseries of auroral brightness (kR) estimated from the projected image from day 63 of the pulsating spot (red) and day 64 of the large flashing region (black). Local peaks (red) and troughs (blue) have been highlighted. There is a 2-3 minute periodicity.

also excluded. This is to focus on the comparison of the UV polar region with the X-ray hotspot caused by ion precipitation, rather than the hard X-rays from electron brehmsstralung along the main oval.

To avoid any bias where images could only be partially viewed, a model of the fractional area of interest on view vs CML was generated. For the 2014 dataset, only the images with the lowest CMLs were affected. Areas of auroral emission in the region of interest over 350 kR were selected. The threshold of 350 kR ensures that only aurora about background emission are selected; the threshold can be reduced to about 100 kR without producing different results.

Figure 6.7 shows the number of points (each point is 0.25° by 0.25° region) vs CML. A dashed line showing the fractional view (in the whole high latitude region) according to CML is scaled against the y axis (i.e. 80% of region on view is 80% the height of the y axis) and is also plotted. The number of points detected above threshold is greater at lower CML, where it might be expected that for the number of points may peak with

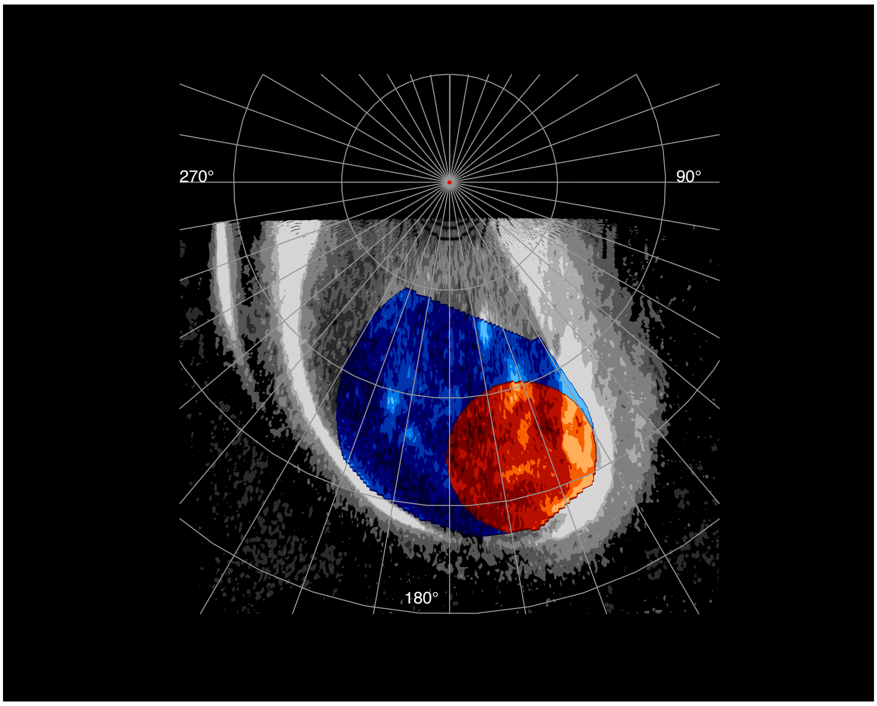

Figure 6.6: Polar projection of DOY 7 (07:26 UT) from the 2014 HST campaign. The image is in grey, with the 'halo' region in blue, the 'core' region in orange.

maximal viewing angle. This behaviour is reflected in the active flare emissions too. At lower CML, lower longitudes are more visible, corresponding to the kinked region of the MO and the area mapping to the duskside of the magnetosphere indicating that more emission tends to come from dusk, as *Kimura et al.* (2016) also found.

Figure 6.8 shows this behaviour for the core and halo regions for days 7 and 10 that both show large flare structures, albeit in a restricted 120-175 ° CML range. The same behaviour as found for the whole high latitude region is reflected in the halo region, indicating there is some preference to emission at lower longitudes within this region. In the core region, there is no relationship between the two indicating that this region tends to be uniformly populated. The core region, however, is already situated slightly duskward within the high latitude region.

The points can be mapped into the equatorial plane using an internal magnetic field model (VIPAL) and a flux-equivalence mapping method (after *Vogt et al.* (2011, 2015)). Figure 6.9 shows that the flare points map to the duskward side in the equatorial plane. This is similar to what *Kimura et al.* (2016) found in terms of local time dependence for

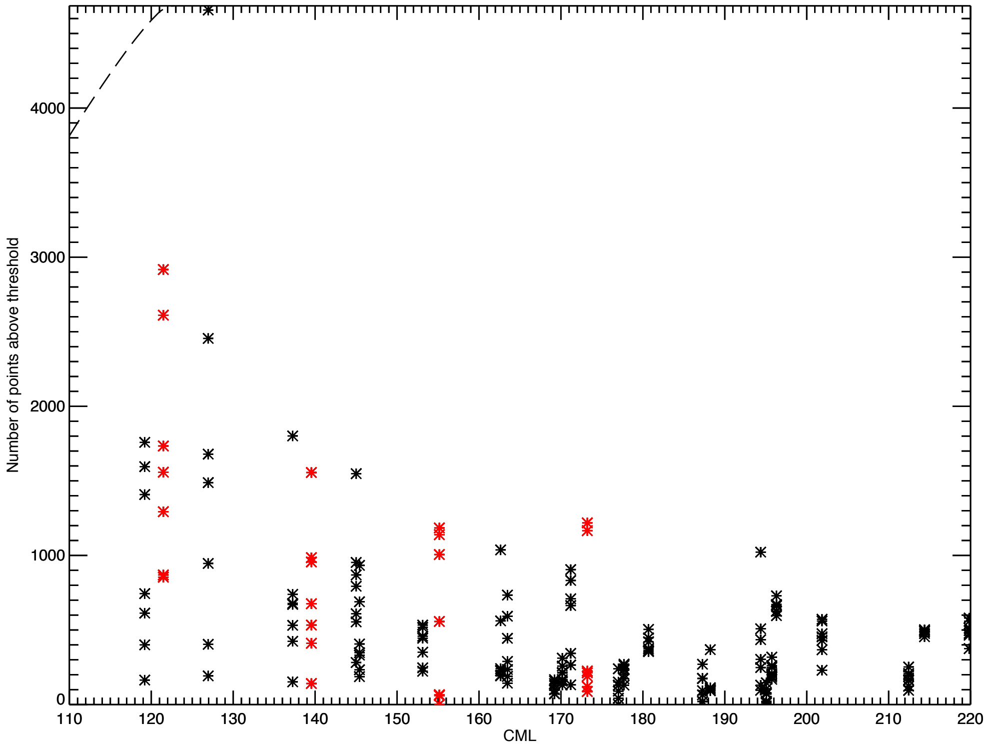

Figure 6.7: The number of points above a 350 kR threshold v CML of images in the 2014 campaign. The red points show large flare activity. The dashed line is scaled against the y axis and shows the fraction of the total region of interest on view at each CML; after about 125° the whole of the region of interest (in this case, the high latitude region) can be seen.

the core region. The radial distance of the mapped points in the UV are close to the magnetopause, as was found the core region in the X-Ray emissions.

6.5 Discussion

The main emission shows several branches as part of its response to the CIR impact. These are all discussed in the main emission subsection, despite having high latitude components. As *Nichols et al.* (2009a) note, it is possible to consider these high latitude branches as being co-rotation driven or controlled directly by the solar wind. First the main emission changes are discussed, then the high latitude features are discussed.

The main emission is brighter at the time of compression. Comparing the first and last image of each day's observations suggest that the brightness in the dayside main emission increases, with different parts become gradually brighter aside from the local noon emission, which is not brighter, as suggested by *Chané et al.* (2017). The authors

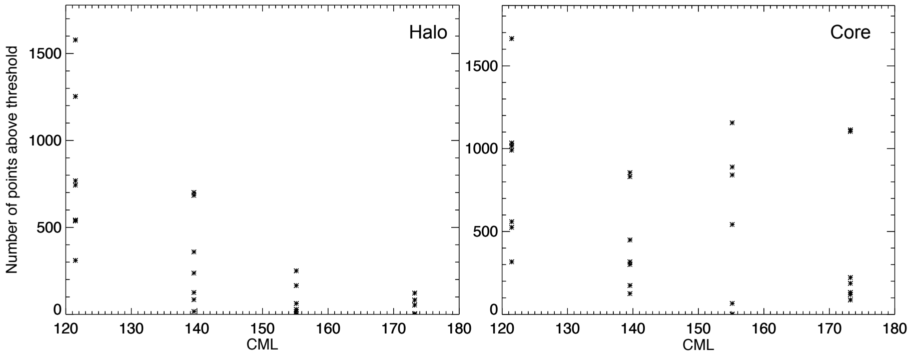

FIGURE 6.8: The number of points above a 350 kR threshold v CML of images from days showing large scale flare activity (days 7 and 10). The left panel shows the number of points from the halo region and the right panel shows the core region.

suggest changes are due to the compression of the magnetosphere, leading to increased field bend-back, field elongation on the nightside and compression on the dayside. The radial component of the magnetic field has changed, so the field aligned currents that flow along these field lines have also changed, causing the a slight intensity of the main emission on the dayside to increase (see *Chané et al.* (2017) for further details). *Nichols et al.* (2017a) also showed this response in the so-called well-defined main emission.

Nichols et al. (2009a) studied this interval in the UV. The study associated the branching of the main emission with the compression region in the solar wind. They noted the importance of considering that the poleward branches were either a separate polar structure, or possibly a movement or expansion of the main emission itself.

The emissions along these poleward arcs in this interval are seen to brighten at the same longitudes as the brightened main emission (seen in Fig 6.3c and 6.3f), just as Bonfond found (*Bonfond et al.*, 2016). There is also emission in the region around the strongest parts of the enhancement (seen in particular in Fig 6.3c) this could be due to a large power input affecting the ionosphere around the main currents, or due to increased wave-particle scattering as a result of energisation.

Given the arc response around the main emission appears with both CIR impacts, there may be a link between the main emission field lines and the CIR impact; it is unlikely that this is direct since the field lines are so far into the magnetosphere that they are likely to be unaffected by compression. However, enhanced plasma flows as a result of the compression may cause changes to the main emission. Two scenarios for this are discussed below, though both may be occurring simultaneously: firstly enhanced

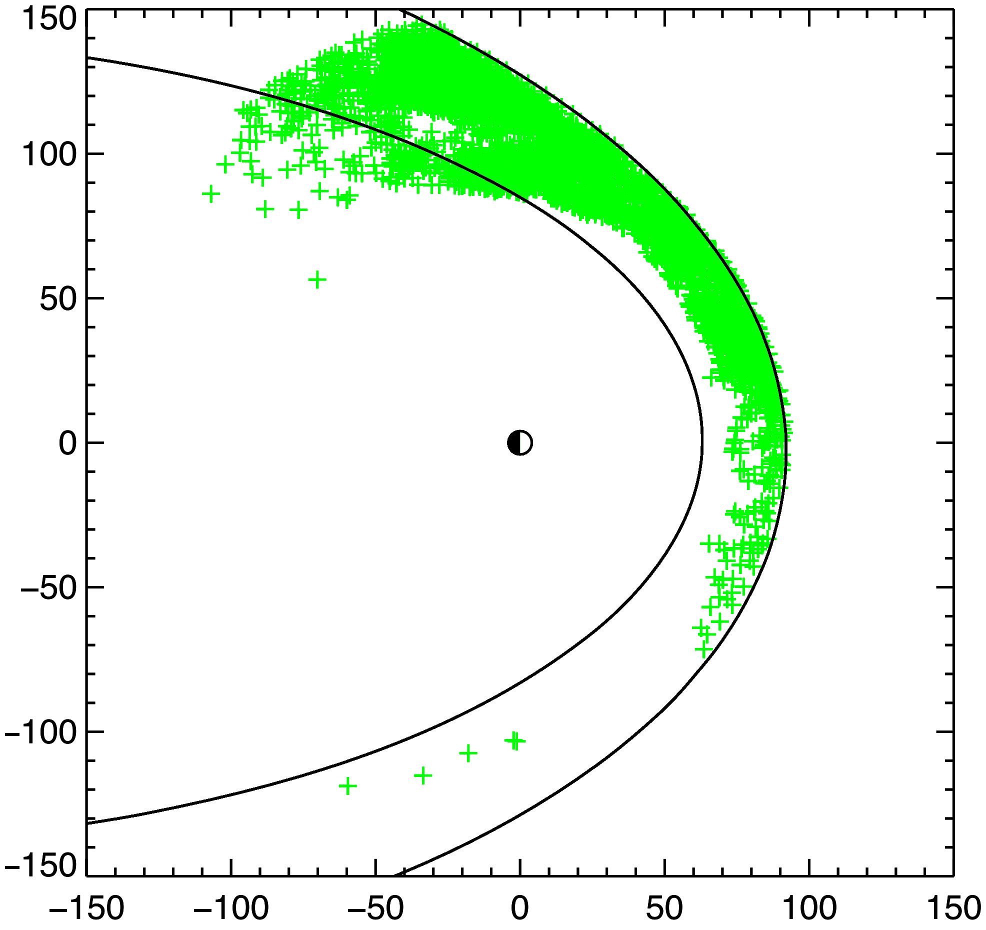

Figure 6.9: Equatorial mapping of points in the X-Y plane of points over the campaign on closed field lines from the high latitude region. The mapping used the VIPAL internal field model and the flux-equivalence mapping method of *Vogt et al.* (2011, 2015). The magnetopause is the *Joy et al.* (2002) compressed and expanded magnetopauses. There is a clear duskward preference for the mapping.

velocity shears due to enhanced flow structures causes current divergence into the ionosphere causing emission or alternatively that compression causes a progressive stepwise breakdown in co-rotation where layers of plasma is sped up to co-rotation.

It is thought that as a result of compression, tail reconnection can be triggered and less dense return flows from tail reconnection travel around the dawn flank. It is also thought that as the field lines contract towards the planet, the plasma should begin to increase in azimuthal flow velocity as a result of conservation of angular momentum (e.g. *Cowley and Bunce* (2003)). Plasma rotating more rapidly may cause more Vasyliunas cycle reconnection to proceed. There are notable levels of night and dawn side polar spot emission and low latitude emission that are both indicative of increased Vasyliunas reconnection, return flows and radial interchange. These two changes in the plasma flows may cause preferential flow channels to form, causing velocity shears in the plasma and currents to couple these into the ionosphere and therefore arcs of emission. If these plasma velocity shears formed radially outside of the plasma responsible for the nominal main emission on the dusk side, the emission arcs should form poleward of prior main emission as in Fig.6.2.

It is also suggested that compression of the magnetosphere may enhance a step-wise breakdown plasma velocity increases as angular momentum is conserved. The infrared main emission has previously been reported to show parallel arc structure that could be the result of stepwise co-rotation breakdown (see for example Fig 4 of *Mura et al.* (2017)), where the UV main emission would lie along the outermost branch. If the main emission UV 'upwards current' is caused by electron precipitation, in accordance with *Cowley and Bunce* (2001), this current is the innermost region of sub-corotation; the rest of the sub co-rotating plasma lies radially outside this, so a stepwise co-rotation breakdown current system would form radially further from the planet. Aurora relating to this current, such as the branches seen in the infrared should form poleward of the main emission. The successive polar branches may trace out plasma flow lines at different velocities in the equatorial plane up to the open-closed field line boundary. It is then notable that the most poleward UV emission branch shows a roughly similar shape to the open closed boundary described in magnetic field modelling by *Vogt et al.* (2011, 2015) and also fits the region of 'mussel shaped' higher colour ratio discussed in *Bonfond et al.* (2017a). It has already been suggested that the highest latitude features may link directly to the solar wind. *Nichols et al.* (2007) suggest, after *Cowley et al.* (2007), that the poleward arc of the main emission could be the result of flow shears across the open/closed field boundary.

In the observations following those showing multiple arcs, the main emission is dim, particularly around noon and forms a singlebranch poleward of its previous location. In the final observations, the main emission has returned to its nominal emission position and remains dim. The dimming and equatorial shift has previously been reported as a result of magnetospheric expansion (*Badman et al.*, 2016). This corresponds to the exit of the shock in the solar wind data.

The appearance of tail reconnection signatures in the so-called DAR (*Nichols et al.*, 2017a) and polar dawn spots (*Radioti et al.*, 2008a) may suggest that tail reconnection has been triggered in this interval because of compression of the magnetotail and/or increased radial transport (or both). It is hard to suggest a timescale of response due to the uncertainty in CIR arrival, but the response happens within a few planetary rotations. These two signatures are expected as soon as 10h after enhanced mass loading (*Nichols et al.*, 2017a), so a response time of a few rotations is not unreasonable.

One interesting result is the appearance of the pulsating spot shown in Fig 6.4 and its brightness timeseries in Fig 6.5, which shows a periodicity of 2-3 minutes. The spot shows at least one (with a possible other the first image of the sequence) intriguing change in morphology where it spreads to poleward longitudes. The 2-3 minute timescale (as discussed in the chapter introduction) is associated with flux transfer events, indicating that a reconnection driver for the emissions should be considered.

The observations on the day after the pulsating spot emission are seen (i.e. on day 55) show changes in the main emission enhancements too; some branches are being enhanced, some left dimmer image to image. Figure 6.3 shows that a large poleward region can be enhanced by precipitation. Figure 6.5 shows that the periodicity of 2-3 minutes stands for the large region and also the cusp emission, indicating they may have a common source or driver.

These observations could relate to the up-down current system suggested in *Bunce et al.* (2004) as a result of, perhaps, pulsed reconnection. The spot could correspond to the cusp spot and the upward current. The branches that are not lit could correspond to the down current field - this new suggestion should be explored with simultaneous X-Ray observations to indicate the 'down' current region.

Kimura et al. (2016) found that the X-Ray emission peaks at lower CML, indicating that for the X-Ray there was still a duskward preference for the emission. In the UV, however, the hotspot is more uniformly populated. If the UV and X-Ray ion-driven emission are linked, the link is likely to occur in the hotspot region. These results are for a limited CML range; a study over a wider range of CML and longer time periods of flare activity may find this behaviour changes at high CML although physically this is unexpected since both in the UV and X-Ray the high latitude region at lower-longitudes seems to exhibit more emission. The UV pulsating spot and large flashing emission and the X-Ray hotspot emission both map the magnetopause on the duskside (see Fig 6.9), indicating again that there may be some common driver in the region for the UV hotspot emission and the ion-driven emission which dominates emission from the X-Ray hotspot.

It may be that the pulsating spot emission and the large emissions are temporally linked - i.e. cusp reconnection is responsible for both emissions and opening of an active region at high latitudes is what causes the larger emission. The amount of flux opened in a reconnection event can be estimated by comparing the size of the active regions in the spot and the large region. Using $F = BA$ and the VIPAL magnetic field model, the flux of the spot area (the enhanced region at around 172° longitude and 64° latitude in Fig. 6.4a) is 14 GWb. For the expanded enhanced area (defined as the common pink enhanced region in Fig. 6.3c and 6.3f) is 172 GWb. This indicates that 158 GWb can be opened in this type of event as a result of dayside reconnection. *Vogt et al.* (2015) estimated that the open cap contained between 520-570 GWb depending on the field model used. *Nichols et al.* (2006) found that over one solar rotation, 500 GWb should be opened. Opening 158 GWb would be a significant, though not impossible, proportion.

If comparison to X-Ray data was possible, we may not expect to see structure of up/down currents specifically/distinctly because of exposure times and not exact simultaneity - the imposed cusp current system may be expected to be dynamic due to the bursty nature of the reconnection driving it. *Bonfond et al.* (2011) had found that emissions pulsing with a 2-3 minute periodicity could occur on closed field lines due to a common phase in north/south pulsations. Alternate triggers that can occur on closed field lines (such as, for example, the Kelvin-Helmholtz instability) should be considered.

6.6 Conclusion

This chapter has examined the UV from the high latitudes during compression intervals and solar wind quiet times. The morphologies of the UV after a compression displayed two key elements: the parallel arcs in the region where the main emission would be expected and the large scale flashes both poleward of and over these arcs. The high latitudes also displayed large scale flashes in the solar wind quiet time interval. There may have been a small solar wind compression around day 8 but the images from the 2007 campaign, where the CIR response was examined, shows the distinct arc formation described above and shown in Fig. 6.2b, 6.2c, 6.2e and 6.2f. This does not appear in the solar wind quiet interval, indicating perhaps that the arc response is reserved for stronger compression events. This supports the interpretation that the arcs in the main emission are a result of strong compressions either due to enhanced flow structures at the dusk side or a stepwise co-rotation breakdown in response to increase of azimuthal plasma velocity.

It is interesting that the large-scale flashing behaviour appears in both the solar wind compression response but also for either no or weak solar wind compressions too, indicating that the solar wind driver is relatively weak. It was found from comparing the

UV and X-Ray response that the two emissions may be spatially linked and both show a lower longitude preference for emission and duskward side mapping in the equatorial plane. This is in agreement with the *Bunce et al.* (2004) model of an up (UV) and down (X-Ray) current formed from pulsed cusp reconnection. The 2-3 minute timescale found in small spots and the larger scale flashes has previously been linked to flux transfer events. On the other hand, the model doesn't predict such large auroral flashes and requires open field reconnection, whereas *Bonfond et al.* (2011) found in conjugate studies of each hemisphere's high latitude regions that there is a common period (of 2-3 minutes), implying the driver lies on closed field lines. Magnetic mapping places the emission driver at the magnetopause, which would agree with both mechanisms. It remains an open question as to what causes the large scale flashes at high latitudes and an alternate explanation, for example, the triggering of the Kelvin-Helmholtz instability is required.

Chapter 7

Summary and Future Work

This chapter summarises the work of this thesis and then suggests extensions based on open questions it has identified.

7.1 Summary

The first two data chapters of this thesis discuss the radial transport of hot plasma injections from reconnection return flow. The first chapter looked at the auroral evidence for the global magnetospheric disturbance. The aurora showed a significantly superrotating polar spot poleward of the main emission on the dawnside. The spot transitioned from the polar to main emission region in the presence of a locally broad, bright dawnside main emission feature and two large equatorward emission features. Radio observations were also examined and both HOM and non-Io DAM were detected. It was inferred from these two sets of observations that hot plasma inflows from tail reconnection flow planetward and may generate the superrotating spot. The main emission feature could be the result of flow shears from prior hot inflows, indicating that this region in the magnetophere may be a 'transition region'. Equatorward emissions are evidence of hot plasma injections in the inner magnetosphere. The images are thought to be part of a prolonged period of reconnection and injection taking place over several hours.

The second data chapter examined the effect of hot plasma injection in the middle to inner magnetosphere. The UV auroral plasma injection signatures were examined and the second oval feature was characterised. The location of the second oval feature lies between the Ganymede and Europa moon footprint contours between 150 and 240°

system III longitude, corresponding to a source in the inner magnetosphere between 9 R_J and 13 R_J. At the examined longitudes, this is in the same region of 11 R_J to 16 R_J known as the pitch angle distribution boundary, beyond which electrons are thought to be scattered into a field-aligned configuration and cause auroral precipitation. The feature is enhanced in both brightness and longitudinal spread 1-3 days after large hot plasma injections. The precipitating electrons have a higher-energy and lower flux than the electrons generating large injection signatures. It was suggested that wave-particle interactions are responsible for the scattering of electrons in this region. We also suggest that the plasma injections can act as a temperature anisotropy and particle source to enhance electron scattering into the aurora and the brightness of the second oval feature. An alternate suggestion was also made: changes to the magnetic field topology around an injection may also generate shear Alfvén waves and therefore accelerate electrons parallel to the magnetic field resulting in precipitation.

The auroral evidence for these two chapters can be summarised in a set of three HST images. Figure 7.1 shows in each row from left to right shows an example of this complete process in the aurora from the 2014 HST campaign. The top row starts with 7.1a - a large injection signature indicated that prior to this, some large interchange motions have been triggered to bring hot plasma into the inner magnetosphere so that it might cause aurora. In panel 7.1b, arcs have developed, confined in latitude and elongated longitudinally. In 7.1c, one arc has faded and either another has appeared or one has moved clockwise, perhaps suggesting that the plasma has drifted around the planet. In the bottom panel more of the sequence of events over the first two data chapters can be seen. In 7.1d, the superrotating spot is captured at the top of the left hand main emission feature and large injections can also be seen. This show the link between features that map to between around 90 R_J to 10 R_J demonstrating that this is a truly global phenomenon. The evolution in 7.1e shows the second oval developing next to small injection signatures. This demonstrates that the reconnection and injection interval can last over a period of several days. Another large injection event is thought to have occurred on day 14 of the campaign (not imaged, but detected in radio data as large HOM emission) after which the image in figure 7.1f is taken, showing a ‘full’ second oval.

In the third data chapter, the auroral response to co-rotating interaction regions and solar wind compression was investigated. It was shown that in there are both high latitude and mid latitude features that arise - large scale flashes appear at high latitudes, sometimes along side significant branching of the main emission region.

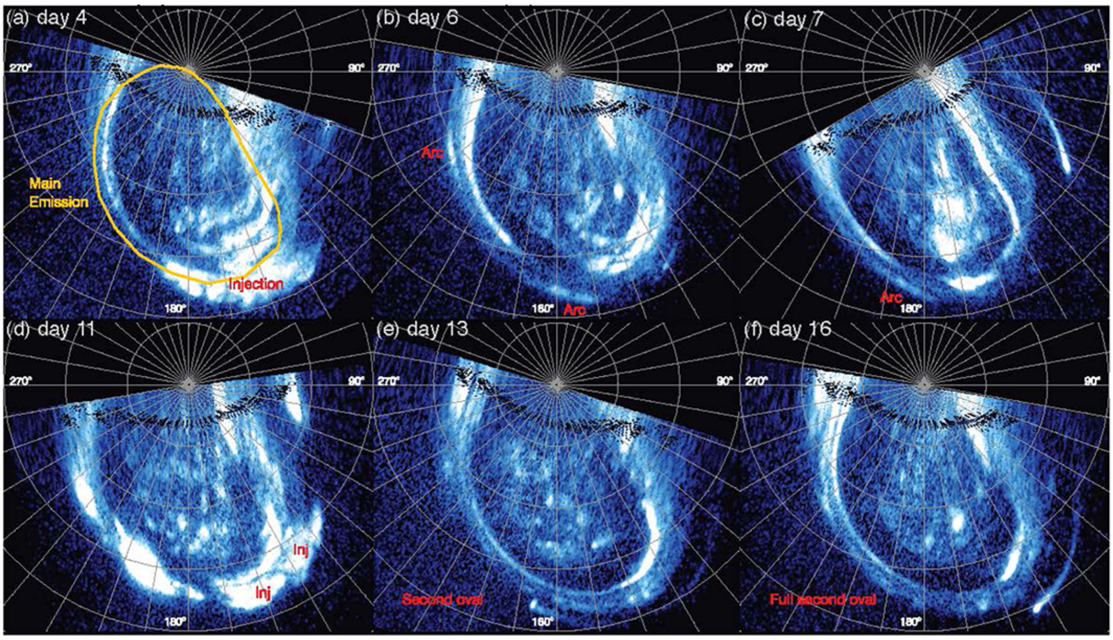

Figure 7.1: Six polar projected images taken with the HST, with log intensity scale saturated at 400 kR. For each image the exposure time was 100 s. The grey lines indicate a 10° × 10° jovicentric latitude-system III longitude grid. The image is oriented such that 180° system III longitude is directed toward the bottom and labels are displayed in grey. Top row, left to right, a) Injection event, day 4 01:10 UT, average main emission position for campaign in gold, b) day 6 02:35 UT, c) day 7 07:16 UT. Bottom row, left to right, d) Injection event, day 11 00:31 UT, e) day 13 22:39 UT, f) After HOM emission, indicator of in injection event, on day 14, day 16 00:03 UT.

The sequential response of the UV aurora to a strong compression was shown in two set of responses in February and March 2007. Figure 7.2 shows the response for the February event, as summarised in table 6.1. The predominant features were main emission contraction and expansion, main emission branching and periodic large and small high latitude flares at low longitudes. A statistical study examining the occurrence of high latitude flares with varied CML using 2014 data showed that emissions were likely to form at lower longitudes and fall into a similar region to the reported X-Ray hot spot. This suggested that perhaps the emissions could be driven by the same mechanism. *Bunce et al.* (2004) suggest a model of an up and down current formed from pulsed cusp reconnection. The 2-3 minute timescale found in small spots and the larger scale flashes has previously been linked to flux transfer events. On the other hand, the model doesn't predict such large auroral flashes and requires open field reconnection, whereas *Bonfond et al.* (2011) found in conjugate studies of each polar cap that there is a common period (of 2-3 minutes), implying the driver lies on closed field lines. Another possibility that has not been discussed here is whether the Kelvin Helmholtz instability is triggered around the dusk flank magnetopause as part of the solar wind impact.

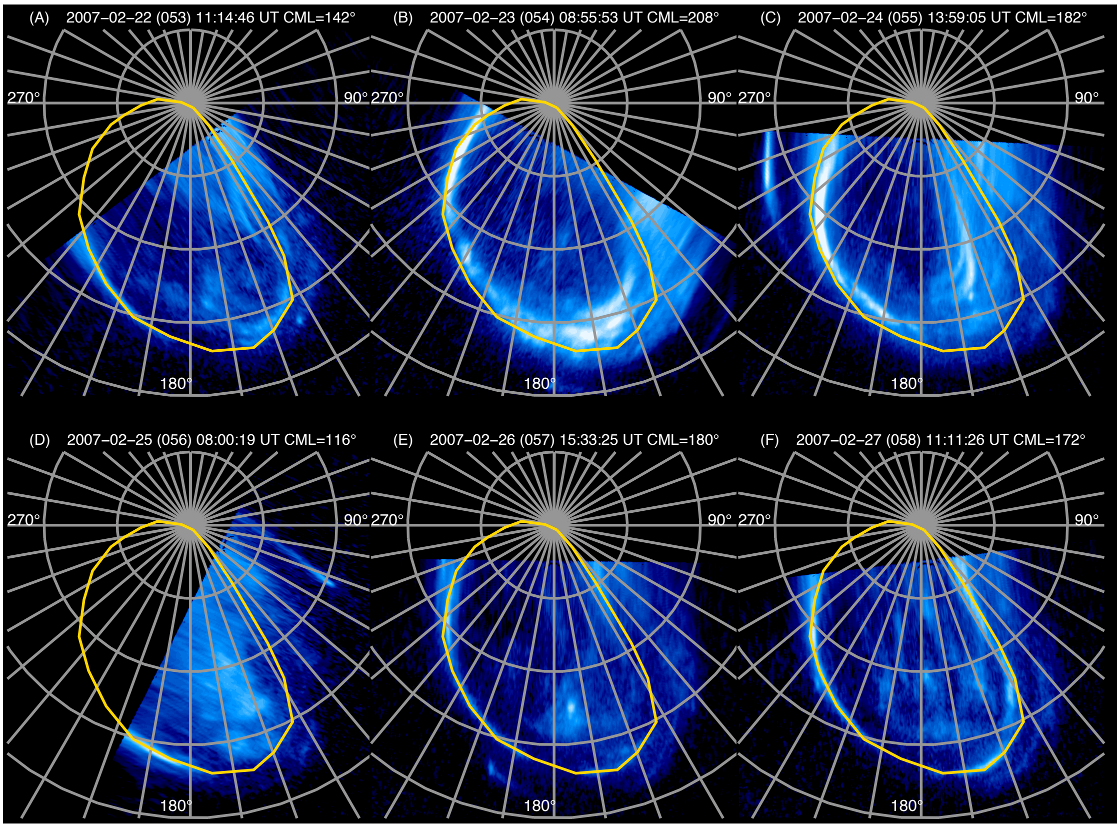

FIGURE 7.2: Six panels showing polar-projected HST image of Jupiter's northern FUV aurora over the CIR impact during February. For each image the exposure time was between 30 and 100 s. The Central Meridian Longitude (CML) is shown. The image is displayed with a log intensity scale saturated at 1000 kR. The grey lines indicate a 10° 10°jovicentric latitude-system III longitude grid. The image is oriented such that 180° $_{III}$ is directed toward the bottom and $_{III}$ labels are displayed in white.

During smaller compression or quiet solar wind intervals only the high latitude flashing response was seen, indicating that perhaps the main emission branching response is reserved for stronger compression events. This supports the interpretation that the arcs in the main emission are a result of strong compression either due to enhanced flow structures at the dusk side or a stepwise co-rotation breakdown in response to increase of azimuthal plasma velocity.

7.2 Future Work

The first two data chapters investigate the radial transport of plasma in the magnetosphere with particular interest to the hot return flows from reconnection. Chapter 4 showed that the hot plasma inflows may come into a 'transition region' as they move radially towards the planet. *Thomsen et al.* (2015) suggests that at Saturn, there is a plasmapause - a region of interface between hot sparse plasma and cold dense plasma that forms in the inner magnetosphere as a result of hot plasma injections coming into contact with the denser magnetospheric plasma. This region is thought to have prime conditions for interchange process. A full investigation to assess whether this sort of boundary should occur in the Jovian middle magnetosphere, with a view to determining the nature of this 'transition region' should be conducted. From the size of the low latitude auroral injection signatures presented in the first two data chapters, it is suggested that the scale of the interchange process is much larger that the kronian counterpart. Orbits from Juno could help characterise the plasma along the field lines that map to the transition region, particularly in terms of the plasma thermal energy, to eluidate the processes in the 'transition region'. Imaging from other wavelength ranges, for example X-Ray and Infra-Red could be used to probe processes at other energies. Longer-sequence and higher resolution auroral data from UVS (than HST) could help capture more examples of this process occurring for further analysis - for example, how long does the main emission feature associated with the 'transition region' last for? How long is the region maintained in the magnetosphere for? How does the region come onset and decline? What is the nature of the flow shears potentially occurring in that region? How does that compare to other rotationally driven planets? How does a very large reconnection and injection interval effect the transition region? To what extent can the process of return flow enhance interchange motions, pushing more cold dense plasma outward and driving the Vasyliunas cycle?

Chapter 5 suggested that hot plasma injections could provide energy to enhance wave-particle interactions and thus cause the auroral signature of the second oval. The properties of these wave-particle interactions could be understood further - At what rates do the plasma injections drift? How does the second oval feature relate to the large injection signatures - under what conditions can the plasma generate the second oval auroral signature? What happens to the plasma after it disperses around the planet?

Finally, if the processes examined in the first and second data chapter are part of the same process, more longer-sequence auroral data can be used to probe the timescales of these global magnetospherics.

The final data chapter of the thesis investigated the UV response to solar wind co-rotating interaction regions and compressions. Pulsed high latitude reconnection was examined as a possible cause of the large period flares. To investigate whether it is a system of up and down currents formed at the cusp, as described by *Bunce et al.* (2004), simultaneous

X-Ray (down current) and UV (up current) data can be used to see whether this up-down current structure does exist at the cusp. Similarly, conjugate studies of both polar caps can be used to see where the emissions come from. By comparing the timing of the emissions in the aurorae, it is possible to tell whether emissions are coming from closed field lines or open ones, and where on the field line the particle source is.

The Kelvin-Helmholtz instability has also not been properly investigated as a source of perturbation to cause emission - this is due to time constraints. Instability down the dusk flank may be expected to produce aurora on the dusk side of the planet. Future work, perhaps in collaboration with modelers, should seek to compare the observations presented in chapter 6 with the expectation from magnetospheric models.

The statistical study made with 2014 data should be repeated with the 2007 images so that a statistical picture of the 2007 campaign high latitude region which can be compared to individual morphologies during the CIR interval. This may make it clear whether the CIR interval causes a particular morphology compared to other solar wind compressions and also lend statistical weight (i.e. not case studies) to the high latitude morphologies seen. In chapter 6 in order to quantify the amount of image on view with CML, the number of pixels in a region above a detection threshold was compared to the CML. This allowed detections of any type of flare, compared to trying to identify the brightest or most powerful of flares. An extension to this work using the 2007 campaign (which had months of data, compared to the fortnight of data from 2014) is to examine both whether flares have occurred and how bright/powerful they are compared to, for example, solar wind conditions. This combination of morphology and power may allow determination of the driver (or drivers) for the morphologies. This is especially pertinent for morphologies that sometimes appear to overlap (e.g. high latitude flares and main emission branching) which may or may not have related drivers.

Further work also needs to be done investigating the main emission branching to explain both how the branching in the main emission arises but also how each branch's brightness is driven. It has been proposed here that the branching of the main emission is either due to enhanced flow structures at the dusk side or a stepwise co-rotation breakdown in response to increase of azimuthal plasma velocity. Further examination of the auroral morphologies and mapping of the main emission to the equatorial plane may show the location of flow shears. This in turn can give a handle on how compressed the magnetosphere is. The brightness of the branches could indicate the magnitude of the flow shear, allowing preferential flow channels to be identified. This could indicate whether the stepwise co-rotation breakdown or dusk flow channels are the dominant factor in plasma flow dynamics.

Bibliography

Acuña, M. H., K. W. Behannon, and J. E. P. Connerney (1983), Jupiter's magnetic field and magnetosphere, in *Physics of the Jovian Magnetosphere*, edited by A. J. Dessler, pp. 1–50.

Allegrini, F., F. Bagenal, S. Bolton, J. Connerney, G. Clark, R. W. Ebert, T. K. Kim, W. S. Kurth, S. Levin, P. Louarn, B. Mauk, D. J. McComas, C. Pollock, D. Ranquist, M. Reno, J. R. Szalay, M. F. Thomsen, P. Valek, S. Weidner, R. J. Wilson, and J. L. Zink (2017), Electron beams and loss cones in the auroral regions of jupiter, *Geophysical Research Letters*, *44*(14), 7131–7139, doi:10.1002/2017GL073180, 2017GL073180.

Badman, S. V., and S. W. H. Cowley (2007), Significance of Dungey-cycle flows in Jupiter's and Saturn's magnetospheres, and their identification on closed equatorial field lines, *Ann. Geophys.*, *25*, 941–951, doi:10.5194/angeo-25-941-2007.

Badman, S. V., A. Masters, H. Hasegawa, M. Fujimoto, A. Radioti, D. Grodent, N. Sergis, M. K. Dougherty, and A. J. Coates (2013), Bursty magnetic reconnection at Saturn's magnetopause, *Geophys. Res. Lett.*, *40*, 1027–1031, doi:10.1002/grl.50199.

Badman, S. V., B. Bonfond, M. Fujimoto, R. L. Gray, Y. Kasaba, S. Kasahara, T. Kimura, H. Melin, J. D. Nichols, A. J. Steffl, C. Tao, F. Tsuchiya, A. Yamazaki, M. Yoneda, I. Yoshikawa, and K. Yoshioka (2016), Weakening of jupiter's main auroral emission during january 2014, *Geophysical Research Letters*, doi:10.1002/2015GL067366, 2015GL067366.

Bagenal, F., T. E. Dowling, and W. B. McKinnon (2007), *Jupiter: the planet, satellites and magnetosphere*, vol. 1, Cambridge University Press.

Baumjohann, W., and R. A. Treumann (2012), *Basic space plasma physics*, World Scientific Publishing Company.

Bhattacharya, B., R. M. Thorne, and D. J. Williams (2001), On the energy source for diffuse jovian auroral emissivity, *Geophysical Research Letters*, *28*(14), 2751–2754, doi:10.1029/2000GL012616.

Biermann, L., B. Brosowski, and H. Schmidt (1967), The interaction of the solar wind with a comet, *Solar Physics*, *1*(2), 254–284.

Bonfond, B. (2010), The 3-D extent of the Io UV footprint on Jupiter, *J. Geophys. Res.*, *115*, doi:10.1029/2010JA015475.

Bonfond, B. (2012), When Moons Create Aurora: The Satellite Footprints on Giant Planets, *Washington DC American Geophysical Union Geophysical Monograph Series*, *197*, 133–140, doi:10.1029/2011GM001169.

Bonfond, B., D. Grodent, J.-C. Gérard, A. Radioti, J. Saur, and S. Jacobsen (2008), UV Io footprint leading spot: A key feature for understanding the UV Io footprint multiplicity?, *Geophys. Res. Lett.*, *35*(5), doi:10.1029/2007GL032418.

Bonfond, B., D. Grodent, J.-C. Gérard, A. Radioti, V. Dols, P. A. Delamere, and J. T. Clarke (2009), The Io UV footprint: Location, inter-spot distances and tail vertical extent, *J. Geophys. Res.*, *114*, doi:10.1029/2009JA014312.

Bonfond, B., M. F. Vogt, J.-C. Gérard, D. Grodent, A. Radioti, and V. Coumans (2011), Quasi-periodic polar flares at Jupiter: A signature of pulsed dayside reconnections?, *Geophys. Res. Lett.*, *38*, L02104, doi:10.1029/2010GL045981.

Bonfond, B., D. Grodent, J.-C. Gérard, T. Stallard, J. T. Clarke, M. Yoneda, A. Radioti, and J. Gustin (2012), Auroral evidence of Io's control over the magnetosphere of Jupiter, *Geophys. Res. Lett.*, *39*, doi:doi:10.1029/2011GL050253.

Bonfond, B., S. Hess, F. Bagenal, J.-C. Gérard, D. Grodent, A. Radioti, J. Gustin, and J. T. Clarke (2013), The multiple spots of the Ganymede auroral footprint, *Geophys. Res. Lett.*, *40*, 4977–4981, doi:10.1002/grl.50989.

Bonfond, B., D. Grodent, S. V. Badman, J.-C. Gérard, and A. Radioti (2016), Dynamics of the flares in the active polar region of jupiter, *Geophysical Research Letters*, *43*(23), 11,963–11,970, doi:10.1002/2016GL071757, grl55293.

Bonfond, B., G. R. Gladstone, D. Grodent, T. K. Greathouse, M. H. Versteeg, V. Hue, M. W. Davis, M. F. Vogt, J.-C. Gérard, A. Radioti, S. Bolton, S. M. Levin, J. E. P. Connerney, B. H. Mauk, P. Valek, A. Adriani, and W. S. Kurth (2017a), Morphology of the uv aurorae jupiter during juno's first perijove observations, *Geophysical Research Letters*, *44*(10), 4463–4471, doi:10.1002/2017GL073114, 2017GL073114.

Bonfond, B., J. Saur, D. Grodent, S. Badman, D. Bisikalo, V. Shematovich, J.-C. Gérard, and A. Radioti (2017b), The tails of the satellite auroral footprints at jupiter, *Journal of Geophysical Research: Space Physics*, *122*(8), 7985–7996.

Boudjada, M., P. Galopeau, and H. Rucker (2001), Jovian hectometric beam observed by pws and waves experiments on board galileo and wind spacecraft, *Planetary and Space Science*, *49*(10), 1151–1158.

Bougeret, J.-L., M. Kaiser, P. Kellogg, R. Manning, K. Goetz, S. Monson, N. Monge, L. Friel, C. Meetre, C. Perche, et al. (1995), Waves: The radio and plasma wave investigation on the wind spacecraft, *Space Science Reviews*, *71*(1-4), 231–263.

Branduardi-Raymont, G., R. F. Elsner, M. Galand, D. Grodent, T. E. Cravens, P. Ford, G. R. Gladstone, and J. H. Waite (2008), Spectral morphology of the X-ray emission from Jupiter's aurorae, *J. Geophys. Res.*, *113*, A02202, doi:10.1029/2007JA012600.

Bunce, E. J., S. W. H. Cowley, and T. K. Yeoman (2004), Jovian cusp processes: Implications for the polar aurora, *J. Geophys. Res.*, *109*, A09S13, doi:10.1029/2003JA010280.

Bunce, E. J., S. W. H. Cowley, and S. E. Milan (2005), Interplanetary magnetic field control of Saturn's polar cusp aurora, *Ann. Geophys.*, *23*, 1405–1431, doi:10.5194/angeo-23-1405-2005.

Chané, E., J. Saur, R. Keppens, and S. Poedts (2017), How is the jovian main auroral emission affected by the solar wind?, *Journal of Geophysical Research: Space Physics*, *122*(2), 1960–1978.

Clarke, J. T., H. W. Moos, S. K. Atreya, and A. L. Lane (1980), Observations from earth orbit and variability of the polar aurora on Jupiter, *Astrophys. J. Lett.*, *241*, L179–L182, doi:10.1086/183386.

Clarke, J. T., D. Grodent, S. W. H. Cowley, E. J. Bunce, P. Zarka, J. E. P. Connerney, and T. Satoh (2004), Jupiter's aurora, in *Jupiter. The Planet, Satellites and Magnetosphere*, edited by F. Bagenal, T. E. Dowling, and W. B. McKinnon, pp. 639–670.

Clarke, J. T., J. Nichols, J. C. Gerard, D. Grodent, K. C. Hansen, W. Kurth, G. R. Gladstone, J. Duval, S. Wannawichian, E. Bunce, S. W. H. Cowley, F. Crary, M. Dougherty, L. Lamy, D. Mitchell, W. Pryor, K. Retherford, T. Stallard, B. Zieger, P. Zarka, and

B. Cecconi (2009), Response of Jupiter's and Saturn's auroral activity to the solar wind, *J. Geophys. Res.*, *114*, A05210, doi:10.1029/2008JA013694.

Cole, G. (2002), *Planetary science : the science of planets around stars*, Institute of Physics Pub., Bristol.

Connerney, J. E. P., M. H. Acuña, and N. F. Ness (1981), Modeling the jovian current sheet and inner magnetosphere, *Journal of Geophysical Research: Space Physics*, *86*(A10), 8370–8384, doi:10.1029/JA086iA10p08370.

Connerney, J. E. P., M. H. Acuña, N. F. Ness, and T. Satoh (1998), New models of Jupiter's magnetic field constrained by the Io flux tube footprint, *J. Geophys. Res.*, *103*, 11,929–11,940, doi:10.1029/97JA03726.

Cowley, S., and E. Bunce (2003), Modulation of jupiter's main auroral oval emissions by solar wind induced expansions and compressions of the magnetosphere, *Planetary and Space Science*, *51*(1), 57 – 79, doi:https://doi.org/10.1016/S0032-0633(02)00118-6.

Cowley, S. W. H., and E. J. Bunce (2001), Origin of the main auroral oval in Jupiter's coupled magnetosphere-ionosphere system, *Planet. Space. Sci.*, *49*, 1067–1088, doi:10.1016/S0032-0633(00)00167-7.

Cowley, S. W. H., and E. J. Bunce (2003), Corotation-driven magnetosphere-ionosphere coupling currents in Saturn's magnetosphere and their relation to the auroras, *Ann. Geophys.*, *21*(8), 1691–1707.

Cowley, S. W. H., E. J. Bunce, T. S. Stallard, and S. Miller (2003), Jupiter's polar ionospheric flows: Theoretical interpretation, *Geophys. Res. Lett.*, *30*, 1220, doi:10.1029/2002GL016030.

Cowley, S. W. H., J. D. Nichols, and D. J. Andrews (2007), Modulation of Jupiter's plasma flow, polar currents, and auroral precipitation by solar wind-induced compressions and expansions of the magnetosphere: a simple theoretical model, *Ann. Geophys.*, *25*, 1433–1463, doi:10.5194/angeo-25-1433-2007.

Cowley, S. W. H., J. D. Nichols, and C. M. Jackman (2015), Down-tail mass loss by plasmoids in jupiter's and saturn's magnetospheres, *Journal of Geophysical Research: Space Physics*, *120*(8), 6347–6356, doi:10.1002/2015JA021500, 2015JA021500.

Cowley, S. W. H., G. Provan, E. Bunce, and J. Nichols (2017), Magnetosphere-ionosphere coupling at jupiter: Expectations for juno perijove 1 from a steady state axisymmetric physical model, *Geophysical Research Letters*, *44*(10), 4497–4505.

Davies, A. G. (2007), *Volcanism on Io : a comparison with Earth*, Cambridge planetary science, Cambridge University Press, Cambridge.

Delamere, P., F. Bagenal, C. Paranicas, A. Masters, A. Radioti, B. Bonfond, L. Ray, X. Jia, J. Nichols, and C. Arridge (2015), Solar wind and internally driven dynamics: Influences on magnetodiscs and auroral responses, *Space Science Reviews*, *187*(1-4), 51–97.

Delamere, P. A., and F. Bagenal (2010), Solar wind interaction with Jupiter's magnetosphere, *J. Geophys. Res.*, *115*, A10201, doi:10.1029/2010JA015347.

Desroche, M., F. Bagenal, P. Delamere, and N. Erkaev (2012), Conditions at the expanded jovian magnetopause and implications for the solar wind interaction, *Journal of Geophysical Research: Space Physics*, *117*(A7).

Dessler, A. J. (1983), *Physics of the Jovian Magnetosphere*, Cambridge Univ. Press, Cambridge, UK.

Dumont, M., D. Grodent, A. Radioti, and J.-C. Gérard (2014), Jupiter's equatorward auroral features: Possible signatures of magnetospheric injections, *J. Geophys. Res.*, *119*(12), 10,068–10,077, doi:10.1002/2014JA020527.

Dumont, M., D. Grodent, A. Radioti, B. Bonfond, E. Roussos, and C. Paranicas (2015), Simulations of the auroral signatures of jupiter's magnetospheric injections, *EPSC Abstracts*, *10*(EPSC2015-642).

Dungey, J. W. (1961), Interplanetary Magnetic Field and the Auroral Zones, *Phys. Res. Lett.*, *6*, 47–48, doi:10.1103/PhysRevLett.6.47.

Dungey, J. W. (1963), The structure of the exosphere or adventures in velocity space, in *Geophysics, The Earth's Environment*, edited by C. De Witt, J. Hieblot, and L. Le Beau, p. 503.

Dunn, W. R., G. Branduardi-Raymont, R. F. Elsner, M. F. Vogt, L. Lamy, P. G. Ford, A. J. Coates, G. R. Gladstone, C. M. Jackman, J. D. Nichols, et al. (2016), The impact of an icme on the jovian x-ray aurora, *Journal of Geophysical Research: Space Physics*, *121*(3), 2274–2307.

Elsner, R. F., N. Lugaz, J. H. Waite, T. E. Cravens, G. R. Gladstone, P. Ford, D. Grodent, A. Bhardwaj, R. J. MacDowall, M. D. Desch, and T. Majeed (2005), Simultaneous Chandra X ray, Hubble Space Telescope ultraviolet, and Ulysses radio observations of Jupiter's aurora, *J. Geophys. Res.*, *110*, A01207, doi:10.1029/2004JA010717.

Fujimoto, M., and A. Nishida (1990), Monte carlo simulation of energization of jovian trapped electrons by recirculation, *Journal of Geophysical Research: Space Physics*, *95*(A4), 3841–3853, doi:10.1029/JA095iA04p03841.

Galopeau, P. H. M., and M. Y. Boudjada (2005), Solar wind control of jovian auroral emissions, *Journal of Geophysical Research: Space Physics*, *110*(A9), doi:10.1029/2004JA010843, a09221.

Ge, Y., C. Russell, and K. Khurana (2010), Reconnection sites in jupiter's magnetotail and relation to jovian auroras, *Planetary and Space Science*, *58*(11), 1455–1469.

Gérard, J.-C., E. J. Bunce, D. Grodent, S. W. H. Cowley, J. T. Clarke, and S. V. Badman (2005), Signature of Saturn's auroral cusp: Simultaneous Hubble Space Telescope FUV observations and upstream solar wind monitoring, *J. Geophys. Res.*, *110*, A11201, doi:10.1029/2005JA011094.

Gérard, J.-C., B. Bonfond, D. Grodent, A. Radioti, J. T. Clarke, G. R. Gladstone, J. H. Waite, D. Bisikalo, and V. I. Shematovich (2014), Mapping the electron energy in Jupiter's aurora: Hubble spectral observations, *J. Geophys. Res.*, *119*, 9072–9088, doi:10.1002/2014JA020514.

Gladstone, G. R., J. H. Waite, D. Grodent, W. S. Lewis, F. J. Crary, R. F. Elsner, M. C. Weisskopf, T. Majeed, J.-M. Jahn, A. Bhardwaj, J. T. Clarke, D. T. Young, M. K. Dougherty, S. A. Espinosa, and T. E. Cravens (2002), A pulsating auroral X-ray hot spot on Jupiter, *Nature*, *415*, 1000–1003.

Glauert, S. A., and R. B. Horne (2005), Calculation of pitch angle and energy diffusion coefficients with the padie code, *Journal of Geophysical Research: Space Physics*, *110*(A4), n/a–n/a, doi:10.1029/2004JA010851, a04206.

Gold, T. (1959), Motions in the magnetosphere of the earth, *Journal of Geophysical Research*, *64*(9), 1219–1224.

Gosling, J., and V. Pizzo (1999), Formation and evolution of corotating interaction regions and their three dimensional structure, in *Corotating Interaction Regions*, pp. 21–52, Springer.

Grodent, D. (2015), A brief review of ultraviolet auroral emissions on giant planets, *Space Science Reviews*, *187*(1-4), 23–50.

Grodent, D., J. H. Waite Jr., and J.-C. Gérard (2001), A self-consistent model of the Jovian auroral thermal structure, *J. Geophys. Res.*, *106*, 12,933–12,952, doi:10.1029/2000JA900129.

Grodent, D., J. T. Clarke, J. Kim, J. H. Waite, and S. W. H. Cowley (2003), Jupiter's main auroral oval observed with HST-STIS, *J. Geophys. Res.*, *108*, A11, doi:10.1029/2003JA009921.

Grodent, D., J.-C. Gérard, J. T. Clarke, G. R. Gladstone, and J. H. Waite (2004), A possible auroral signature of a magnetotail reconnection process on Jupiter, *J. Geophys. Res.*, *109*, A05201, doi:10.1029/2003JA010341.

Grodent, D., B. Bonfond, J.-C. Gérard, A. Radioti, J. Gustin, J. T. Clarke, J. Nichols, and J. E. P. Connerney (2008a), Auroral evidence of a localized magnetic anomaly in Jupiter's northern hemisphere, *J. Geophys. Res.*, *113*, A09201, doi:10.1029/2008JA013185.

Grodent, D., J.-C. Gérard, A. Radioti, B. Bonfond, and A. Saglam (2008b), Jupiter's changing auroral location, *J. Geophys. Res.*, *113*(A1), doi:10.1029/2007JA012601.

Gurnett, D. A., W. S. Kurth, G. B. Hospodarsky, A. M. Persoon, P. Zarka, A. Lecacheux, S. J. Bolton, M. D. Desch, W. M. Farrell, M. L. Kaiser, H.-P. Ladreiter, H. O. Rucker, P. Galopeau, P. Louarn, D. T. Young, W. R. Pryor, and M. K. Dougherty (2002), Control of Jupiter's radio emission and aurorae by the solar wind, *Nature*, *415*, 985–987.

Gustin, J., J.-C. Gérard, D. Grodent, S. W. H. Cowley, J. T. Clarke, and A. Grard (2004), Energy-flux relationship in the FUV Jovian aurora deduced from HST-STIS spectral observations, *J. Geophys. Res.*, *109*, A10205, doi:10.1029/2003JA010365.

Gustin, J., J.-C. Gérard, G. R. Gladstone, D. Grodent, and J. T. Clarke (2006), Characteristics of Jovian morning bright FUV aurora from Hubble Space Telescope/Space Telescope Imaging Spectrograph imaging and spectral observations, *J. Geophys. Res.*, *111*, A09220, doi:10.1029/2006JA011730.

Gustin, J., B. Bonfond, D. Grodent, and J.-C. Gérard (2012), Conversion from HST ACS and STIS auroral counts into brightness, precipitated power, and radiated power for H_2 giant planets, *J. Geophys. Res.*, *117*, A07316, doi:10.1029/2012JA017607.

Gustin, J., D. Grodent, L. Ray, B. Bonfond, E. Bunce, J. Nichols, and N. Ozak (2016), Characteristics of north jovian aurora from {STIS} {FUV} spectral images, *Icarus*, *268*, 215 – 241, doi:http://dx.doi.org/10.1016/j.icarus.2015.12.048.

Hasegawa, H., M. Fujimoto, T.-D. Phan, H. Reme, A. Balogh, M. Dunlop, C. Hashimoto, and R. TanDokoro (2004), Transport of solar wind into earth's magnetosphere through rolled-up kelvin–helmholtz vortices, *Nature*, *430*(7001), 755–758.

Hasegawa, H., A. Retinò, A. Vaivads, Y. Khotyaintsev, M. André, T. Nakamura, W.-L. Teh, B. Sonnerup, S. Schwartz, Y. Seki, et al. (2009), Kelvin-helmholtz waves at the earth's magnetopause: Multiscale development and associated reconnection, *Journal of Geophysical Research: Space Physics*, *114*(A12).

Henderson, M. G., G. D. Reeves, and J. S. Murphree (1998), Are north-south aligned auroral structures an ionospheric manifestation of bursty bulk flows?, *Geophysical Research Letters*, *25*(19), 3737–3740, doi:10.1029/98GL02692.

Hess, S. L. G., B. Bonfond, P. Zarka, and D. Grodent (2011), Model of the Jovian magnetic field topology constrained by the Io auroral emissions, *J. Geophys. Res.*, *116*, A05217, doi:10.1029/2010JA016262.

Hess, S. L. G., E. Echer, and P. Zarka (2012), Solar wind pressure effects on Jupiter decametric radio emissions independent of Io, *Planet. Space. Sci.*, *70*, 114–125, doi: 10.1016/j.pss.2012.05.011.

Hess, S. L. G., E. Echer, P. Zarka, L. Lamy, and P. Delamere (2014), Multi-instrument study of the Jovian radio emissions triggered by solar wind shocks and inferred magnetospheric subcorotation rates, *Planet. Space. Sci.*

Hill, T. W. (2001), The Jovian auroral oval, *J. Geophys. Res.*, *106*, 8101–8108, doi: 10.1029/2000JA000302.

Hospodarsky, G., W. Kurth, B. Cecconi, D. Gurnett, M. Kaiser, M. Desch, and P. Zarka (2004), Simultaneous observations of jovian quasi-periodic radio emissions by the galileo and cassini spacecraft, *Journal of Geophysical Research: Space Physics*, *109*(A9).

Huddleston, D. E., C. T. Russell, G. Le, and A. Szabo (1997), Magnetopause structure and the role of reconnection at the outer planets, *J. Geophys. Res.*, *102*(A11), 24,289–24,302.

Hundhausen, A. (1995), The solar wind, *Introduction to space physics*, pp. 91–128.

Imai, M., A. Lecacheux, M. Moncuquet, F. Bagenal, C. A. Higgins, K. Imai, and J. R. Thieman (2015), Modeling jovian hectometric attenuation lanes during the cassini flyby of jupiter, *Journal of Geophysical Research: Space Physics*, *120*(3), 1888–1907, doi:10.1002/2014JA020815, 2014JA020815.

Jackman, C. M., N. Achilleos, E. J. Bunce, S. W. H. Cowley, M. K. Dougherty, G. H. Jones, S. E. Milan, and E. J. Smith (2004), Interplanetary magnetic field at ∼9 AU during the declining phase of the solar cycle and its implications for Saturn's magnetospheric dynamics, *J. Geophys. Res.*, *109*(A11), A11203, doi:10.1029/2004JA010614.

Jackman, C. M., J. A. Slavin, and S. W. H. Cowley (2011), Cassini observations of plasmoid structure and dynamics: Implications for the role of magnetic reconnection in magnetospheric circulation at Saturn, *J. Geophys. Res.*, *116*, A10212, doi:10.1029/2011JA016682.

Johnson, R., and F. Leblanc (2001), The physics and chemistry of sputtering by energetic plasma ions, in *Physics of Space: Growth Points and Problems*, pp. 259–269, Springer.

Joy, S. P., M. G. Kivelson, R. J. Walker, K. K. Khurana, C. T. Russell, and T. Ogino (2002), Probabilistic models of the Jovian magnetopause and bow shock locations, *J. Geophys. Res.*, *107*, 1309, doi:10.1029/2001JA009146.

Karanikola, I., M. Athanasiou, G. Anagnostopoulos, G. Pavlos, and P. Preka-Papadema (2004), Quasi-periodic emissions (15–80 min) from the poles of jupiter as a principal source of the large-scale high-latitude magnetopause boundary layer of energetic particle, *Planetary and Space Science*, *52*(5-6), 543–559.

Kasahara, S., E. A. Kronberg, N. Krupp, T. Kimura, C. Tao, S. V. Badman, A. Retinò, and M. Fujimoto (2011), Magnetic reconnection in the Jovian tail: X-line evolution and consequent plasma sheet structures, *J. Geophys. Res.*, *116*, A11219, doi:10.1029/2011JA016892.

Kasahara, S., E. A. Kronberg, T. Kimura, C. Tao, S. V. Badman, A. Masters, A. Retinò, N. Krupp, and M. Fujimoto (2013), Asymmetric distribution of reconnection jet fronts in the jovian nightside magnetosphere, *Journal of Geophysical Research: Space Physics*, *118*(1), 375–384.

Katoh, Y., F. Tsuchiya, Y. Miyoshi, A. Morioka, H. Misawa, R. Ujiie, W. S. Kurth, A. T. Tomás, and N. Krupp (2011), Whistler mode chorus enhancements in association with energetic electron signatures in the jovian magnetosphere, *Journal of Geophysical Research: Space Physics*, *116*(A2), doi:10.1029/2010JA016183, a02215.

Keiling, A., V. Angelopoulos, A. Runov, J. Weygand, S. Apatenkov, S. Mende, J. McFadden, D. Larson, O. Amm, K.-H. Glassmeier, et al. (2009), Substorm current wedge driven by plasma flow vortices: Themis observations, *Journal of Geophysical Research: Space Physics*, *114*(A1).

Khurana, K. K., M. G. Kivelson, V. M. Vasyliunas, N. Krupp, J. Woch, A. Lagg, B. H. Mauk, and W. S. Kurth (2004), The configuration of jupiter's magnetosphere, *Jupiter: The planet, satellites and magnetosphere*, *1*, 593–616.

Kimura, T., F. Tsuchiya, H. Misawa, A. Morioka, H. Nozawa, and M. Fujimoto (2011), Periodicity analysis of Jovian quasi-periodic radio bursts based on Lomb-Scargle periodograms, *J. Geophys. Res.*, *116*, A03204, doi:10.1029/2010JA016076.

Kimura, T., S. V. Badman, C. Tao, K. Yoshioka, G. Murakami, A. Yamazaki, F. Tsuchiya, B. Bonfond, A. J. Steffl, A. Masters, S. Kasahara, H. Hasegawa, I. Yoshikawa, M. Fujimoto, and J. T. Clarke (2015), Transient internally-driven aurora at Jupiter discovered by Hisaki and the Hubble Space Telescope, *Geophys. Res. Lett.*, *in press*, doi:10.1002/2015GL063272.

Kimura, T., R. Kraft, R. Elsner, G. Branduardi-Raymont, G. Gladstone, C. Tao, K. Yoshioka, G. Murakami, A. Yamazaki, F. Tsuchiya, et al. (2016), Jupiter's x-ray and euv auroras monitored by chandra, xmm-newton, and hisaki satellite, *Journal of Geophysical Research: Space Physics*, *121*(3), 2308–2320.

Kinrade, J., S. V. Badman, E. Bunce, C. Tao, G. Provan, S. Cowley, A. Grocott, R. Gray, D. Grodent, T. Kimura, et al. (2017), An isolated, bright cusp aurora at saturn, *Journal of Geophysical Research: Space Physics.*

Kita, H., T. Kimura, C. Tao, F. Tsuchiya, H. Misawa, T. Sakanoi, Y. Kasaba, G. Murakami, K. Yoshioka, A. Yamazaki, et al. (2016), Characteristics of solar wind control on jovian uv auroral activity deciphered by long-term hisaki exceed observations: Evidence of preconditioning of the magnetosphere?, *Geophysical Research Letters*, *43*(13), 6790–6798.

Kivelson, M. G., and K. K. Khurana (2002), Properties of the magnetic field in the jovian magnetotail, *Journal of Geophysical Research: Space Physics*, *107*(A8), SMP 23–1–SMP 23–9, doi:10.1029/2001JA000249.

Kivelson, M. G., and C. T. Russell (1995), *Introduction to space physics*, Cambridge university press.

Kivelson, M. G., K. K. Khurana, C. T. Russell, and R. J. Walker (1997), Intermittent short-duration magnetic field anomalies in the Io torus: Evidence for plasma interchange?, *Geophys. Res. Lett.*, *24*, 2127, doi:10.1029/97GL02202.

Knight, S. (1973), Parallel electric fields, *Planet. Space. Sci.*, *21*, 741–750, doi:10.1016/0032-0633(73)90093-7.

Kronberg, E. A., J. Woch, N. Krupp, A. Lagg, K. K. Khurana, and K.-H. Glassmeier (2005), Mass release at Jupiter: Substorm-like processes in the Jovian magnetotail, *J. Geophys. Res.*, *110*, A03211, doi:10.1029/2004JA010777.

Krupp, N., V. M. Vasyliũnas, J. Woch, A. Lagg, K. K. Khurana, M. G. Kivelson, B. H. Mauk, E. C. Roelof, D. J. Williams, S. M. Krimigis, W. S. Kurth, L. A. Frank, and J. D. Patterson (2004), Dynamics of the Jovian Magnetosphere, in *Jupiter: the planet, satellites and magnetosphere*, edited by Bagenal, F., Dowling, T. E., & McKinnon, W. B., pp. 617–638, Cambridge University Press.

Kurth, W., M. Imai, G. Hospodarsky, D. Gurnett, P. Louarn, P. Valek, F. Allegrini, J. Connerney, B. Mauk, S. Bolton, et al. (2017), A new view of jupiter's auroral radio spectrum, *Geophysical Research Letters*, *44*(14), 7114–7121.

Ladreiter, H. P., P. Zarka, and A. Lacacheux (1994), Direction finding study of Jovian hectometric and broadband kilometric radio emissions: Evidence for their auroral origin, *Planet. Space. Sci.*, *42*, 919–931, doi:10.1016/0032-0633(94)90052-3.

Lamy, L., R. Prangé, W. Pryor, J. Gustin, S. V. Badman, H. Melin, T. Stallard, D. G. Mitchell, and P. C. Brandt (2013), Multi-spectral simultaneous diagnosis of Saturn's aurorae throughout a planetary rotation, *J. Geophys. Res.*, *118*, 1–27, doi:10.1002/jgra.50404.

Li, W., R. M. Thorne, V. Angelopoulos, J. W. Bonnell, J. P. McFadden, C. W. Carlson, O. LeContel, A. Roux, K. H. Glassmeier, and H. U. Auster (2009a), Evaluation of whistler-mode chorus intensification on the nightside during an injection event observed on the themis spacecraft, *Journal of Geophysical Research: Space Physics*, *114*(A1), n/a–n/a, doi:10.1029/2008JA013554, a00C14.

Li, W., R. M. Thorne, V. Angelopoulos, J. Bortnik, C. M. Cully, B. Ni, O. LeContel, A. Roux, U. Auster, and W. Magnes (2009b), Global distribution of whistler-mode chorus waves observed on the themis spacecraft, *Geophysical Research Letters*, *36*(9), n/a–n/a, doi:10.1029/2009GL037595, l09104.

Li, W., R. M. Thorne, Q. Ma, X.-J. Zhang, G. R. Gladstone, V. Hue, P. W. Valek, F. Allegrini, B. H. Mauk, G. Clark, W. S. Kurth, G. B. Hospodarsky, J. E. P. Connerney, and S. J. Bolton (2017), Understanding the origin of jupiter's diffuse aurora using juno's first perijove observations, *Geophysical Research Letters*, pp. n/a–n/a, doi:10.1002/2017GL075545, 2017GL075545.

Louarn, P., A. Roux, S. Perraut, W. S. Kurth, and D. A. Gurnett (2000), A study of the Jovian "energetic magnetospheric events" observed by Galileo: role in the radial plasma transport, *J. Geophys. Res.*, *105*, 13,073–13,088, doi:10.1029/1999JA900478.

Louarn, P., B. H. Mauk, M. G. Kivelson, W. S. Kurth, A. Roux, C. Zimmer, D. A. Gurnett, and D. J. Williams (2001), A multi-instrument study of a Jovian magnetospheric disturbance, *J. Geophys. Res.*, *106*, 29,883–29,898, doi:10.1029/2001JA900067.

Louarn, P., C. P. Paranicas, and W. S. Kurth (2014), Global magnetodisk disturbances and energetic particle injections at Jupiter, *J. Geophys. Res.*, *119*, 4495–4511, doi: 10.1002/2014JA019846.

Louarn, P., M. G. Kivelson, and W. S. Kurth (2016), On the links between the radio flux and magnetodisk distortions at jupiter, *Journal of Geophysical Research: Space Physics*, *121*(10), 9651–9670, doi:10.1002/2016JA023106, 2016JA023106.

Louarn, P., F. Allegrini, D. McComas, P. Valek, W. Kurth, N. André, F. Bagenal, S. Bolton, J. Connerney, R. Ebert, et al. (2017), Generation of the jovian hectometric radiation: First lessons from juno, *Geophysical Research Letters*.

Mauk, B. H., D. J. Williams, and R. W. McEntire (1997), Energy-time dispersed charged particle signatures of dynamic injections in jupiter's inner magnetosphere, *Geophysical Research Letters*, *24*(23), 2949–2952, doi:10.1029/97GL03026.

Mauk, B. H., D. J. Williams, R. W. McEntire, K. K. Khurana, and J. G. Roederer (1999), Storm-like dynamics of Jupiter's inner and middle magnetosphere, *J. Geophys. Res.*, *104*, 22,759–22,778, doi:10.1029/1999JA900097.

Mauk, B. H., J. T. Clarke, D. Grodent, J. H. Waite, C. P. Paranicas, and D. J. Williams (2002), Transient aurora on Jupiter from injections of magnetospheric electrons, *Nature*, *415*, 1003–1005.

Mauk, B. H., D. K. Haggerty, C. Paranicas, G. Clark, P. Kollmann, A. M. Rymer, S. J. Bolton, S. M. Levin, A. Adriani, F. Allegrini, F. Bagenal, B. Bonfond, J. E. P. Connerney, G. R. Gladstone, W. S. Kurth, D. J. McComas, and P. Valek (2017a), Discrete and broadband electron acceleration in jupiter's powerful aurora, *Nature*, *549*(7670), 66–69.

Mauk, B. H., D. K. Haggerty, C. Paranicas, G. Clark, P. Kollmann, A. M. Rymer, D. G. Mitchell, S. J. Bolton, S. M. Levin, A. Adriani, F. Allegrini, F. Bagenal, J. E. P. Connerney, G. R. Gladstone, W. S. Kurth, D. J. McComas, D. Ranquist, J. R. Szalay, and P. Valek (2017b), Juno observations of energetic charged particles over jupiter's polar regions: Analysis of monodirectional and bidirectional electron beams, *Geophysical Research Letters*, *44*(10), 4410–4418, doi:10.1002/2016GL072286, 2016GL072286.

McComas, D. J., and F. Bagenal (2007), Jupiter: A fundamentally different magnetospheric interaction with the solar wind, *Geophys. Res. Lett.*, *34*, L20106, doi:10.1029/2007GL031078.

McKibben, R., J. Simpson, and M. Zhang (1993), Impulsive bursts of relativistic electrons discovered during ulysses' traversal of jupiter's dusk-side magnetosphere, *Planetary and space science*, *41*(11-12), 1041–1058.

Menietti, J. D., J. B. Groene, T. F. Averkamp, R. B. Horne, E. E. Woodfield, Y. Y. Shprits, M. de Soria-Santacruz Pich, and D. A. Gurnett (2016), Survey of whistler mode chorus intensity at jupiter, *Journal of Geophysical Research: Space Physics*, *121*(10), 9758–9770, doi:10.1002/2016JA022969, 2016JA022969.

Mitchell, D. G., S. M. Krimigis, C. Paranicas, P. C. Brandt, J. F. Carbary, E. C. Roelof, W. S. Kurth, D. A. Gurnett, J. T. Clarke, J. D. Nichols, J.-C. Gérard, D. C. Grodent, M. K. Dougherty, and W. R. Pryor (2009), Recurrent energization of plasma in the midnight-to-dawn quadrant of Saturn's magnetosphere, and its relationship to auroral UV and radio emissions, *Planet. Space. Sci.*, *57*, 1732–1742, doi:10.1016/j.pss.2009.04.002.

Mitchell, D. G., P. C. Brandt, J. F. Carbary, W. S. Kurth, S. M. Krimigis, C. Paranicas, N. Krupp, B. H. Mauk, G. B. Hospodarsky, M. K. Dougherty, and W. R. Pryor (2015), *Injection, Interchange, and Reconnection*, pp. 327–343, John Wiley and Sons, Inc, doi:10.1002/9781118842324.ch19.

Mura, A., A. Adriani, F. Altieri, J. E. P. Connerney, S. J. Bolton, M. L. Moriconi, J.-C. Gérard, W. S. Kurth, B. M. Dinelli, F. Fabiano, F. Tosi, S. K. Atreya, F. Bagenal, G. R. Gladstone, C. Hansen, S. M. Levin, B. H. Mauk, D. J. McComas, G. Sindoni, G. Filacchione, A. Migliorini, D. Grassi, G. Piccioni, R. Noschese, A. Cicchetti, D. Turrini, S. Stefani, M. Amoroso, and A. Olivieri (2017), Infrared observations of jovian aurora from juno's first orbits: Main oval and satellite footprints, *Geophysical Research Letters*, *44*(11), 5308–5316, doi:10.1002/2017GL072954, 2017GL072954.

Murakami, G., K. Yoshioka, A. Yamazaki, F. Tsuchiya, T. Kimura, C. Tao, H. Kita, M. Kagitani, T. Sakanoi, K. Uemizu, Y. Kasaba, I. Yoshikawa, and M. Fujimoto (2016), Response of jupiter's inner magnetosphere to the solar wind derived from extreme ultraviolet monitoring of the io plasma torus, *Geophysical Research Letters*, *43*(24), 12,308–12,316, doi:10.1002/2016GL071675, 2016GL071675.

Nakamura, R., W. Baumjohann, R. Schödel, M. Brittnacher, V. A. Sergeev, M. Kubyshkina, T. Mukai, and K. Liou (2001), Earthward flow bursts, auroral streamers, and small expansions, *Journal of Geophysical Research: Space Physics*, *106*(A6), 10,791–10,802, doi:10.1029/2000JA000306.

Nakamura, T. K. M., M. Fujimoto, and A. Otto (2006), Magnetic reconnection induced by weak kelvin-helmholtz instability and the formation of the low-latitude boundary layer, *Geophysical Research Letters*, *33*(14), n/a–n/a, doi:10.1029/2006GL026318, l14106.

Ni, B., R. M. Thorne, N. P. Meredith, R. B. Horne, and Y. Y. Shprits (2011), Resonant scattering of plasma sheet electrons leading to diffuse auroral precipitation: 2. evaluation for whistler mode chorus waves, *Journal of Geophysical Research: Space Physics*, *116*(A4), n/a–n/a, doi:10.1029/2010JA016233, a04219.

Nichols, J., and S. Cowley (2004), Magnetosphere-ionosphere coupling currents in Jupiter's middle magnetosphere: effect of precipitation-induced enhancement of the ionospheric Pedersen conductivity, *Ann. Geophys.*, *22*, 1799–1827, doi:10.5194/angeo-22-1799-2004.

Nichols, J. D. (2011), Magnetosphere-ionosphere coupling in Jupiter's middle magnetosphere: Computations including a self-consistent current sheet magnetic field model, *J. Geophys. Res.*, *116*, A10232, doi:10.1029/2011JA016922.

Nichols, J. D., and S. W. H. Cowley (2003), Magnetosphere-ionosphere coupling currents in Jupiter's middle magnetosphere: dependence on the effective ionospheric Pedersen conductivity and iogenic plasma mass outflow rate, *Ann. Geophys.*, *21*, 1419–1441, doi:10.5194/angeo-21-1419-2003.

Nichols, J. D., S. W. H. Cowley, and D. J. McComas (2006), Magnetopause reconnection rate estimates for jupiter's magnetosphere based on interplanetary measurements at 5au, *Annales Geophysicae*, *24*(1), 393–406, doi:10.5194/angeo-24-393-2006.

Nichols, J. D., E. J. Bunce, J. T. Clarke, S. W. H. Cowley, J.-C. Gérard, D. Grodent, and W. R. Pryor (2007), Response of Jupiter's UV auroras to interplanetary conditions as observed by the Hubble Space Telescope during the Cassini flyby campaign, *J. Geophys. Res.*, *112*, A02203, doi:10.1029/2006JA012005.

Nichols, J. D., J. T. Clarke, J. C. Gérard, D. Grodent, and K. C. Hansen (2009a), Variation of different components of Jupiter's auroral emission, *J. Geophys. Res.*, *114*, A06210, doi:10.1029/2009JA014051.

Nichols, J. D., J. T. Clarke, J. C. Gérard, and D. Grodent (2009b), Observations of Jovian polar auroral filaments, *Geophys. Res. Lett.*, *36*, L08101, doi:10.1029/2009GL037578.

Nichols, J. D., S. V. Badman, K. H. Baines, R. H. Brown, E. J. Bunce, J. T. Clarke, S. W. H. Cowley, F. J. Crary, J.-C. Gérard, A. Grocott, D. Grodent, W. S. Kurth, H. Melin, D. G. Mitchell, W. R. Pryor, and T. S. Stallard (2014), Dynamic auroral storms on Saturn as observed by the Hubble Space Telescope, *Geophys. Res. Lett.*, *41*, 3323–3330, doi:10.1002/2014GL060186.

Nichols, J. D., S. V. Badman, F. Bagenal, S. J. Bolton, B. Bonfond, E. J. Bunce, J. T. Clarke, J. E. P. Connerney, S. W. H. Cowley, R. W. Ebert, M. Fujimoto, J.-C. Gérard, G. R. Gladstone, D. Grodent, T. Kimura, W. S. Kurth, B. H. Mauk, G. Murakami, D. J. McComas, G. S. Orton, A. Radioti, T. S. Stallard, C. Tao, P. W. Valek, R. J. Wilson, A. Yamazaki, and I. Yoshikawa (2017a), Response of jupiter's auroras to conditions in the interplanetary medium as measured by the hubble space telescope and juno, *Geophysical Research Letters*, *44*(15), 7643–7652, doi:10.1002/2017GL073029, 2017GL073029.

Nichols, J. D., T. K. Yeoman, E. J. Bunce, M. N. Chowdhury, S. W. H. Cowley, and T. R. Robinson (2017b), Periodic emission within jupiter's main auroral oval, *Geophysical Research Letters*, *44*(18), 9192–9198, doi:10.1002/2017GL074824, 2017GL074824.

Nishida, A. (1976), Outward diffusion of energetic particles from the jovian radiation belt, *Journal of Geophysical Research*, *81*(10), 1771–1773, doi:10.1029/JA081i010p01771.

Nishimura, Y., L. R. Lyons, V. Angelopoulos, T. Kikuchi, S. Zou, and S. B. Mende (2011), Relations between multiple auroral streamers, pre-onset thin arc formation, and substorm auroral onset, *Journal of Geophysical Research: Space Physics*, *116*(A9), n/a–n/a, doi:10.1029/2011JA016768, a09214.

Pallier, L., and R. Prangé (2001), More about the structure of the high latitude Jovian aurorae, *Planet. Space. Sci.*, *49*, 1159–1173, doi:10.1016/S0032-0633(01)00023-X.

Pallier, L., and R. Prangé (2004), Detection of the southern counterpart of the Jovian northern polar cusp: Shared properties, *Geophys. Res. Lett.*, *31*, L06701, doi:10.1029/2003GL018041.

Palmaerts, B., A. Radioti, D. Grodent, E. Chané, and B. Bonfond (2014), Transient small-scale structure in the main auroral emission at jupiter, *Journal of Geophysical Research: Space Physics*, *119*(12), 9931–9938, doi:10.1002/2014JA020688, 2014JA020688.

Parker, E. N. (1958), Dynamics of the interplanetary gas and magnetic fields., *The Astrophysical Journal*, *128*, 664.

Phan, T. D., J. T. Gosling, G. Paschmann, C. Pasma, J. F. Drake, M. Øieroset, D. Larson, R. P. Lin, and M. S. Davis (2010), The dependence of magnetic reconnection on plasma β and magnetic shear: evidence from solar wind observations, *Astrophys. J.*, *719*, L199–L203, doi:10.1088/2041-8205/719/2/L199.

Phan, T. D., G. Paschmann, J. T. Gosling, M. Oieroset, M. Fujimoto, J. F. Drake, and V. Angelopoulos (2013), The dependence of magnetic reconnection on plasma beta and magnetic shear: Evidence from magnetopause observations, *Geophys. Res. Lett.*, *in press*, doi:10.1029/2012GL054528.

Prangé, R., L. Pallier, K. C. Hansen, R. Howard, A. Vourlidas, R. Courtin, and C. Parkinson (2004), An interplanetary shock traced by planetary auroral storms from the Sun to Saturn, *Nature*, *432*, 78–81, doi:10.1038/nature02986.

Radioti, A., D. Grodent, J.-C. Gérard, B. Bonfond, and J. T. Clarke (2008a), Auroral polar dawn spots: Signatures of internally driven reconnection processes at Jupiter's magnetotail, *Geophys. Res. Lett.*, *35*, L03104, doi:10.1029/2007GL032460.

Radioti, A., J.-C. Gérard, D. Grodent, B. Bonfond, N. Krupp, and J. Woch (2008b), Discontinuity in Jupiter's main auroral oval, *J. Geophys. Res.*, *113*, A01215, doi:10.1029/2007JA012610.

Radioti, A., A. T. Tomás, D. Grodent, J.-C. Gérard, J. Gustin, B. Bonford, N. Krupp, J. Woch, and J. D. Menietti (2009), Equatorward diffuse auroral emissions at Jupiter: Simultaneous HST and Galileo observations, *Geophys. Res. Lett.*, *36*, L07101, doi:10.1029/2009GL037857.

Radioti, A., D. Grodent, J.-C. Gérard, and B. Bonfond (2010), Auroral signatures of flow bursts released during magnetotail reconnection at jupiter, *Journal of Geophysical Research: Space Physics*, *115*(A7), doi:10.1029/2009JA014844, a07214.

Radioti, A., D. Grodent, J.-C. Gérard, M. F. Vogt, M. Lystrup, and B. Bonfond (2011), Nightside reconnection at Jupiter: Auroral and magnetic field observations from 26 July 1998, *J. Geophys. Res.*, *116*, A03221, doi:10.1029/2010JA016200.

Radioti, A., E. Roussos, D. Grodent, J.-C. Gérard, N. Krupp, D. G. Mitchell, J. Gustin, B. Bonfond, and W. Pryor (2013), Signatures of magnetospheric injections in Saturn's aurora, *J. Geophys. Res.*, *118*, 1922–1933, doi:10.1002/jgra.50161.

Ray, L. C., R. E. Ergun, P. A. Delamere, and F. Bagenal (2010), Magnetosphere-ionosphere coupling at Jupiter: Effect of field-aligned potentials on angular momentum transport, *J. Geophys. Res.*, *115*, A09211, doi:10.1029/2010JA015423.

Ray, L. C., R. E. Ergun, P. A. Delamere, and F. Bagenal (2012), Magnetosphere-ionosphere coupling at Jupiter: A parameter space study, *Journal of Geophysical Research (Space Physics)*, *117*, A01205, doi:10.1029/2011JA016899.

Roederer, J. G. (2012), *Dynamics of geomagnetically trapped radiation*, vol. 2, Springer Science & Business Media.

Russell, C., and M. Dougherty (2010), Magnetic fields of the outer planets, *Space science reviews*, *152*(1), 251–269.

Russell, C., Z. Yu, and M. Kivelson (2001), The rotation period of jupiter, *Geophysical research letters*, *28*(10), 1911–1912.

Santolík, O., D. A. Gurnett, G. H. Jones, P. Schippers, F. J. Crary, J. S. Leisner, G. B. Hospodarsky, W. S. Kurth, C. T. Russell, and M. K. Dougherty (2011), Intense plasma wave emissions associated with saturn's moon rhea, *Geophysical Research Letters*, *38*(19), n/a–n/a, doi:10.1029/2011GL049219, l19204.

Shay, M. A., J. F. Drake, J. P. Eastwood, and T. D. Phan (2011), Super-alfvénic propagation of substorm reconnection signatures and poynting flux, *Phys. Rev. Lett.*, *107*, 065,001, doi:10.1103/PhysRevLett.107.065001.

Stallard, T., S. Miller, G. Millward, and R. D. Joseph (2001), On the Dynamics of the Jovian Ionosphere and Thermosphere. I. The Measurement of Ion Winds, *Icarus*, *154*, 475–491, doi:10.1006/icar.2001.6681.

Swisdak, M., B. N. Rogers, J. F. Drake, and M. A. Shay (2003), Diamagnetic suppression of component magnetic reconnection at the magnetopause, *J. Geophys. Res.*, *108*, 1218, doi:10.1029/2002JA009726.

Tao, C., S. V. Badman, and M. Fujimoto (2011), UV and IR auroral emission model for the outer planets: Jupiter and Saturn comparison, *Icarus*, *213*, 581–592, doi: 10.1016/j.icarus.2011.04.001.

Tao, C., T. Kimura, S. V. Badman, G. Murakami, K. Yoshioka, F. Tsuchiya, N. André, I. Yoshikawa, A. Yamazaki, D. Shiota, H. Tadokoro, and M. Fujimoto (2016a), Variation of jupiter's aurora observed by hisaki/exceed: 1. observed characteristics of the auroral electron energies compared with observations performed using hst/stis, *Journal of Geophysical Research: Space Physics*, *121*(5), 4041–4054, doi:10.1002/2015JA021271, 2015JA021271.

Tao, C., T. Kimura, S. V. Badman, N. André, F. Tsuchiya, G. Murakami, K. Yoshioka, I. Yoshikawa, A. Yamazaki, and M. Fujimoto (2016b), Variation of jupiter's aurora observed by hisaki/exceed: 2. estimations of auroral parameters and magnetospheric dynamics, *Journal of Geophysical Research: Space Physics*, pp. n/a–n/a, doi:10.1002/2015JA021272, 2015JA021272.

Tao, X., R. M. Thorne, W. Li, B. Ni, N. P. Meredith, and R. B. Horne (2011), Evolution of electron pitch angle distributions following injection from the plasma sheet, *Journal of Geophysical Research: Space Physics*, *116*(A4), n/a–n/a, doi: 10.1029/2010JA016245, a04229.

Thomsen, M. F., D. G. Mitchell, X. Jia, C. M. Jackman, G. Hospodarsky, and A. J. Coates (2015), Plasmapause formation at saturn, *Journal of Geophysical Research: Space Physics*, *120*(4), 2571–2583, doi:10.1002/2015JA021008, 2015JA021008.

Thorne, R. M., T. P. Armstrong, S. Stone, D. J. Williams, R. W. McEntire, S. J. Bolton, D. A. Gurnett, and M. G. Kivelson (1997), Galileo evidence for rapid interchange transport in the Io torus, *Geophys. Res. Lett.*, *24*, 2131, doi:10.1029/97GL01788.

Thorne, R. M., B. Ni, X. Tao, R. B. Horne, and N. P. Meredith (2010), Scattering by chorus waves as the dominant cause of diffuse auroral precipitation, *Nature*, *467*(7318), 943–946.

Tomás, A., J. Woch, N. Krupp, A. Lagg, K.-H. Glassmeier, M. K. Dougherty, and P. G. Hanlon (2004a), Changes of the energetic particles characteristics in the inner part of the Jovian magnetosphere: a topological study, *Planet. Space. Sci.*, *52*, 491–498, doi:10.1016/j.pss.2003.06.011.

Tomás, A. T., J. Woch, N. Krupp, A. Lagg, K.-H. Glassmeier, and W. S. Kurth (2004b), Energetic electrons in the inner part of the Jovian magnetosphere and their relation to auroral emissions, *J. Geophys. Res.*, *109*, A06203, doi:10.1029/2004JA010405.

Tomás, A. T. M. (2005), Energetic particles in the jovian magnetosphere and their relation to auroral emissions, Ph.D. thesis, Braunschweig University of Technology.

Tsuchiya, F., M. Kagitani, K. Yoshioka, T. Kimura, G. Murakami, A. Yamazaki, H. Nozawa, Y. Kasaba, T. Sakanoi, K. Uemizu, and I. Yoshikawa (2015), Local electron heating in Io plasma torus associated with Io from HISAKI satellite observation, *J. Geophys. Res.*, *in press*, doi:10.1002/2015JA021420.

Vasavada, A. R., A. H. Bouchez, A. P. Ingersoll, B. Little, C. D. Anger, and Galileo SSI Team (1999), Jupiter's visible aurora and Io footprint, *J. Geophys. Res.*, *104*, 27,133–27,142, doi:10.1029/1999JE001055.

Vasyliunas, V. M. (1983), Plasma distribution and flow, in *Physics of the Jovian Magnetosphere*, edited by A. J. Dessler, pp. 395–453, Cambridge Univ. Press.

Vogt, M. F., M. G. Kivelson, K. K. Khurana, S. P. Joy, and R. J. Walker (2010), Reconnection and flows in the Jovian magnetotail as inferred from magnetometer observations, *J. Geophys. Res.*, *115*, A06219, doi:10.1029/2009JA015098.

Vogt, M. F., M. G. Kivelson, K. K. Khurana, R. J. Walker, B. Bonfond, D. Grodent, and A. Radioti (2011), Improved mapping of Jupiter's auroral features to magnetospheric sources, *J. Geophys. Res.*, *116*, A03220, doi:10.1029/2010JA016148.

Vogt, M. F., C. M. Jackman, J. A. Slavin, E. J. Bunce, S. W. H. Cowley, M. G. Kivelson, and K. K. Khurana (2014), Structure and statistical properties of plasmoids in jupiter's magnetotail, *Journal of Geophysical Research: Space Physics*, *119*(2), 821–843, doi: 10.1002/2013JA019393, 2013JA019393.

Vogt, M. F., E. J. Bunce, M. G. Kivelson, K. K. Khurana, R. J. Walker, A. Radioti, B. Bonfond, and D. Grodent (2015), Magnetosphere-ionosphere mapping at jupiter: Quantifying the effects of using different internal field models, *Journal of Geophysical Research: Space Physics*, *120*(4), 2584–2599, doi:10.1002/2014JA020729, 2014JA020729.

Waite, J. H., G. R. Gladstone, W. S. Lewis, R. Goldstein, D. J. McComas, P. Riley, R. J. Walker, P. Robertson, S. Desai, J. T. Clarke, and D. T. Young (2001), An auroral flare at Jupiter, *Nature*, *410*, 787–789.

Walker, R. J., and C. T. Russell (1985), Flux transfer events at the Jovian magnetopause, *J. Geophys. Res.*, *90*, 7397–7404, doi:10.1029/JA090iA08p07397.

Watt, C., and R. Rankin (2012), Alfvén wave acceleration of auroral electrons in warm magnetospheric plasma, *Auroral Phenomenology and Magnetospheric Processes: Earth and Other Planets*, pp. 251–260.

Watt, C. E. J., and R. Rankin (2010), Do magnetospheric shear alfvén waves generate sufficient electron energy flux to power the aurora?, *Journal of Geophysical Research: Space Physics*, *115*(A7), n/a–n/a, doi:10.1029/2009JA015185, a07224.

Woodfield, E., R. Horne, S. Glauert, J. Menietti, and Y. Shprits (2014), The origin of jupiter's outer radiation belt, *Journal of Geophysical Research: Space Physics*, *119*(5), 3490–3502, doi:10.1002/2014JA019891.

Woodfield, E. E., R. B. Horne, S. A. Glauert, J. D. Menietti, and Y. Y. Shprits (2013), Electron acceleration at jupiter: input from cyclotron-resonant interaction with whistler-mode chorus waves, *Annales Geophysicae*, *31*(10), 1619–1630, doi:10.5194/angeo-31-1619-2013.

Woodgate, B., R. Kimble, C. Bowers, S. Kraemer, M. Kaiser, A. Danks, J. Grady, J. Loiacono, M. Brumfield, L. Feinberg, et al. (1998), The space telescope imaging spectrograph design, *Publications of the Astronomical Society of the Pacific*, *110*(752), 1183.

Wygant, J., A. Keiling, C. Cattell, M. Johnson, R. Lysak, M. Temerin, F. Mozer, C. Kletzing, J. Scudder, W. Peterson, et al. (2000), Polar spacecraft based comparisons of intense electric fields and poynting flux near and within the plasma sheet-tail lobe boundary to uvi images: An energy source for the aurora, *Journal of Geophysical Research: Space Physics*, *105*(A8), 18,675–18,692.

Xiao, F., R. M. Thorne, D. A. Gurnett, and D. J. Williams (2003), Whistler-mode excitation and electron scattering during an interchange event near io, *Geophysical Research Letters*, *30*(14), n/a–n/a, doi:10.1029/2003GL017123, 1749.

Yoneda, M., M. Kagitani, and S. Okano (2009), Short-term variability of Jupiter's extended sodium nebula, *Icarus*, *204*(2), 589–596, doi:10.1016/j.icarus.2009.07.023.

Yoneda, M., H. Nozawa, H. Misawa, M. Kagitani, and S. Okano (2010), Jupiter's magnetospheric change by Io's volcanoes, *Geophys. Res. Lett.*, *37*, doi:10.1029/2010GL043656.

Yoneda, M., F. Tsuchiya, H. Misawa, B. Bonfond, C. Tao, M. Kagitani, and S. Okano (2013), Io's volcanism controls Jupiter's radio emissions, *Geophys. Res. Lett.*, *40*(4), 671–675.

Yoneda, M., M. Kagitani, F. Tsuchiya, T. Sakanoi, and S. Okano (2015), Brightening event seen in observations of Jupiter's extended sodium nebula, *Icarus*, *261*, 31–33, doi:10.1016/j.icarus.2015.07.037.

Yoshikawa, I., K. Yoshioka, G. Murakami, F. Suzuki, R. Hikida, A. Yamazaki, T. Kimura, F. Tsuchiya, M. Kagitani, T. Sakanoi, K. Uemizu, C. Tao, H. Nozawa, Y. Kasaba, and M. Fujimoto (2016), Properties of hot electrons in the jovian inner magnetosphere deduced from extended observations of the io plasma torus, *Geophysical Research Letters*, *43*(22), 11,552–11,557, doi:10.1002/2016GL070706, 2016GL070706.

Yoshioka, K., F. Tsuchiya, T. Kimura, M. Kagitani, G. Murakami, A. Yamazaki, M. Kuwabara, F. Suzuki, R. Hikida, I. Yoshikawa, F. Bagenal, and M. Fujimoto (2017), Radial variation of sulfur and oxygen ions in the io plasma torus as deduced from remote observations by hisaki, *Journal of Geophysical Research: Space Physics*, *122*(3), 2999–3012, doi:10.1002/2016JA023691, 2016JA023691.

Yung, Y. L., G. R. Gladstone, K. M. Chang, J. M. Ajello, and S. Srivastava (1982), H2 fluorescence spectrum from 1200 to 1700 a by electron impact-laboratory study and application to jovian aurora, *The Astrophysical Journal*, *254*, L65–L69.

Zarka, P. (1998), Auroral radio emissions at the outer planets: Observations and theories, *J. Geophys. Res.*, *103*, 20,159–20,194, doi:10.1029/98JE01323.

Zarka, P., J. Queinnec, and F. J. Crary (2001), Low-frequency limit of jovian radio emissions and implications on source locations and io plasma wake, *Planetary and Space Science*, *49*(10–11), 1137 – 1149, doi:http://dx.doi.org/10.1016/S0032-0633(01)00021-6, magnetosphere of the Outer Planets Part {II}.

Zieger, B., and K. C. Hansen (2008), Statistical validation of a solar wind propagation model from 1 to 10 au, *Journal of Geophysical Research-Space Physics*, *113*(A8), doi:DOI10.1029/2008JA013046.